

*Ollscoil na hÉireann, Gaillimh*  
National University of Ireland, Galway



National University of Ireland, Galway  
*Ollscoil na hÉireann, Gaillimh*

*Roinn na Fisice Trialalaí, an Grúpa Optaice Feidhmí*  
Department of Experimental Physics, Applied Optics Group

# Profiling Atmospheric Turbulence with Single Star SCIDAR

by

**Denis Garnier**

*Supervised by Professor J. C. Dainty*

PhD Thesis  
submitted in fulfilment of the requirements  
for the degree of  
Doctor of Philosophy

Septembre 2007



*A mieu maigran*



# Acknowledgements

I would like to thank my supervisor Prof. Chris Dainty for his help and direction provided during my Ph.D. I want to thank Derek Coburn who has been of immense help for the development of the instrument design and for all the discussions and feedback.

I want to thank Rachel Johnston, of Applied Research Associates New Zealand, for the code for generating Kolmogorov phase screens and for the help she and Richard Lane, also of Applied Research Associates New Zealand, provided me.

I also want to thank ESO for time at the 1-m telescope (La Silla Observatory, Chile) using the generalised double star SCIDAR technique and IAC for the time on the JKT (Roque de Los Muchachos Observatory, La Palma, Spain) during the measurement campaign of October 2005.

Finally I want to thank Prof. Harry Barrett of the College of Optical Science, the University of Arizona for his helpful discussions.



# Abstract

A generalised SCIDAR (SCIntillation Detection And Ranging) system for characterising atmospheric parameters using single star scintillation is presented. Astronomical scintillation is the variation in apparent luminosity of a distant object, such as a star, viewed through the atmosphere. Scintillation is caused almost exclusively by small temperature variations (on the order of 0.1-1K) in the atmosphere, resulting in index-of-refraction fluctuations. The system uses the scintillation to characterise the three-dimensional structure of the atmosphere by estimation of the refractive index structure constant as a function of altitude,  $C_n^2(h)$ . Once the refractive index fluctuation profile is obtained, other atmospheric parameters of interest for astronomy can be derived. The instrument, based on a commercially available 250 mm diameter telescope with an imaging system at its back, was built with the aim portability and the potential for characterising atmospheric parameters for wide areas of the sky.

The principle of SCIDAR is discussed in this thesis. Scintillation patterns are recorded and reduced to autocorrelation functions that are functions of  $C_n^2(h)$ . The problem to retrieve the  $C_n^2(h)$  profile is an ill-posed problem, meaning that a direct inversion technique cannot be used directly due to poor conditioning of the problem. Inverse problem resolution and especially the Tikhonov regularisation technique is discussed. Simulations of scintillation pattern using Fresnel diffraction are made to test the algorithm.

From the simulations, profiles have been obtained and also from real data as well. The results retrieved for a range of different magnitudes of star, up to magnitude 3, are encouraging.





# Contents

<b>List of Figures</b> . . . . .	vi
<b>1. Introduction</b> . . . . .	1
1.1 Introduction . . . . .	1
1.2 Thesis organisation . . . . .	2
<b>Notations and Symbols</b> . . . . .	1
<b>2. Mathematical background</b> . . . . .	6
2.1 Fourier optics . . . . .	6
2.1.1 Fourier transform . . . . .	6
2.1.1.1 Some properties of the Fourier transform . . . . .	7
2.1.1.2 Circular symmetric functions . . . . .	8
2.1.2 Fourier transform of some functions . . . . .	9
2.1.2.1 Circle function . . . . .	9
2.1.2.2 Gaussian function . . . . .	9
2.1.3 Convolution and correlation . . . . .	9
2.1.3.1 Convolution theorem . . . . .	10
2.1.3.2 Autocorrelation theorem . . . . .	10
2.1.4 Energy and power spectra . . . . .	11
2.1.5 Sampling theorem . . . . .	11
2.2 Linear system theory . . . . .	11
2.2.1 Point spread function . . . . .	12
2.2.1.1 Shift-invariant systems . . . . .	12
2.2.2 Transfer functions . . . . .	13
2.3 Random variables . . . . .	13

---

2.3.1	Probability functions . . . . .	14
2.3.2	Moments . . . . .	15
2.3.2.1	Central moments . . . . .	15
2.3.3	Joint probability . . . . .	15
2.3.4	Joint moments . . . . .	16
2.3.5	Conditional probability and Bayes' rule . . . . .	16
2.4	Random processes . . . . .	17
2.4.1	Multiple-point expectations . . . . .	17
2.4.2	Covariance and correlation . . . . .	18
2.4.2.1	Stationarity, isotropy and ergodicity . . . . .	18
2.4.2.2	Stationarity . . . . .	19
2.4.2.3	Isotropy . . . . .	19
2.4.2.4	Ergodicity . . . . .	19
2.4.3	Some distributions . . . . .	20
2.4.3.1	Normal distribution . . . . .	20
2.4.3.2	Poisson distribution . . . . .	20
2.4.3.3	Log-normal distribution . . . . .	20
<b>3.</b>	<b>Atmospheric optics . . . . .</b>	<b>22</b>
3.1	Atmospheric turbulence . . . . .	22
3.1.1	Structure of the atmosphere . . . . .	22
3.1.2	Turbulent zones . . . . .	24
3.1.3	Statistics of refractive index fluctuations . . . . .	25
3.1.3.1	Kolmogorov law . . . . .	25
3.1.3.2	Atmospheric temporal statistics . . . . .	29
3.1.4	Propagation of light through atmospheric turbulence . . . . .	30
3.1.4.1	One thin layer . . . . .	31
3.1.4.2	Free space propagation . . . . .	31
3.1.4.3	Statistical properties of the field . . . . .	32
3.2	Stellar scintillation . . . . .	32
3.2.1	Phase and amplitude statistics . . . . .	32
3.2.1.1	Effect of a thin layer . . . . .	32
3.2.1.2	Effect of multiple layers . . . . .	34

3.2.2	Scintillation statistics . . . . .	34
3.2.3	Wavelength dependence . . . . .	36
3.2.4	Aperture filtering . . . . .	36
3.2.5	Neglecting scintillation effects in high angular resolution techniques . . . . .	36
3.3	SCIDAR . . . . .	37
3.4	Single star SCIDAR . . . . .	39
3.4.1	Wind profile . . . . .	41
3.4.2	Multi-generalised single star SCIDAR . . . . .	42
3.4.3	Other Single star profilers . . . . .	43
3.4.3.1	Spatio-temporal single star SCIDAR . . . . .	43
3.4.3.2	MASS . . . . .	43
3.4.4	Other atmospheric profilers . . . . .	45
3.4.4.1	In situ $C_n^2(h)$ . . . . .	45
3.4.4.2	SLODAR . . . . .	45
3.4.4.3	3D mapping of atmospheric turbulence . . . . .	46
<b>4.</b>	<b>Inverse problems . . . . .</b>	<b>47</b>
4.1	Mathematical basis . . . . .	47
4.1.1	Linearity and boundedness . . . . .	48
4.1.2	Range and domain . . . . .	48
4.1.3	Continuity and compactness . . . . .	48
4.1.4	Matrix operators . . . . .	49
4.1.5	Adjoint operator . . . . .	49
4.1.6	Null space of an operator . . . . .	49
4.1.7	Inverse operator . . . . .	50
4.1.8	Singular value decomposition . . . . .	50
4.1.8.1	Eigenanalysis . . . . .	50
4.1.8.2	Singular value decomposition of a matrix . . . . .	50
4.1.8.3	Hermitian operators . . . . .	51
4.1.8.4	Pseudo-inverse of a matrix . . . . .	52
4.1.8.5	Pseudo-inverse and SVD . . . . .	52
4.2	Well-posed and ill-posed problems . . . . .	53

---

4.2.1	Linear integral equation . . . . .	53
4.2.2	Functional . . . . .	54
4.2.3	Resolution . . . . .	54
4.3	Regularisation methods . . . . .	54
4.3.1	Tikhonov regularisation . . . . .	55
4.3.2	Regularisation parameter selection . . . . .	55
4.3.2.1	Generalised Cross-validation . . . . .	56
4.3.2.2	L-curve . . . . .	56
4.3.2.3	Unbiased Predicted Risk Estimator . . . . .	57
4.4	Statistical methods . . . . .	57
4.4.1	Maximum likelihood estimation . . . . .	57
4.4.1.1	Gaussian Noise . . . . .	58
4.4.1.2	Poisson Noise . . . . .	58
4.4.2	Bayesian estimation . . . . .	58
4.4.3	Maximum entropy . . . . .	59
4.5	Optimization . . . . .	59
4.5.1	Functional minimisation . . . . .	60
4.5.1.1	Steepest descent . . . . .	61
4.5.1.2	Conjugate gradient descent . . . . .	62
4.6	Non-negativity . . . . .	63
4.6.1	Reparametrisation . . . . .	63
4.6.2	Feasibility set and active set . . . . .	64
4.6.3	Projector on the feasibility set . . . . .	65
4.7	Single star SCIDAR problem . . . . .	65
<b>5.</b>	<b>Single star SCIDAR equipment and data collection . . . . .</b>	<b>67</b>
5.1	Instrument considerations . . . . .	67
5.2	Instrument design . . . . .	69
5.3	Calibration . . . . .	74
5.4	Data reduction . . . . .	74
<b>6.</b>	<b>Single star simulations . . . . .</b>	<b>80</b>
6.1	Phase screens . . . . .	80
6.2	Propagation through turbulence . . . . .	81

---

6.2.1	Sampling . . . . .	83
6.2.1.1	Phase . . . . .	84
6.2.1.2	Fresnel propagation . . . . .	85
6.2.1.3	Scintillation . . . . .	85
6.2.2	Edge effect . . . . .	85
6.2.3	Modelling diffraction effect . . . . .	86
<b>7.</b>	<b>Results . . . . .</b>	<b>91</b>
7.1	Results from simulation . . . . .	91
7.2	Results from the campaign at La Palma . . . . .	94
7.2.1	Reduced autocovariances . . . . .	96
7.2.2	$C_n^2(h)$ profile estimates . . . . .	96
7.2.3	Estimation of the error . . . . .	97
<b>8.</b>	<b>Conclusion and future work . . . . .</b>	<b>103</b>
8.1	Summary . . . . .	103
8.2	Future work . . . . .	104
<b>A.</b>	<b>Hilbert Spaces . . . . .</b>	<b>106</b>
A.1	Vectors . . . . .	106
A.2	Hilbert Space . . . . .	106
A.2.1	Distance And Norm . . . . .	107
A.2.2	Completeness . . . . .	107
A.2.3	Scalar Products . . . . .	108
A.2.4	$\mathbb{L}_2$ spaces . . . . .	109

# List of Figures

3.1	Structure of the atmosphere. . . . .	23
3.2	Turbulent zones in the atmosphere. . . . .	24
3.3	Outer and inner scale. . . . .	26
3.4	Classic and Generalised Double Star SCIDAR. . . . .	39
3.5	Single star covariance several layers. . . . .	40
3.6	Single star SCIDAR. . . . .	41
3.7	Kernel of the single star SCIDAR. . . . .	44
3.8	Sequenced generalised single star SCIDAR. . . . .	45
4.1	Steepest descent method. . . . .	62
5.1	Scintillation images of Capella. . . . .	69
5.2	Correspondance between telescope pupil and detected image. . . . .	70
5.3	Details of the single star SCIDAR system. . . . .	70
5.4	System in the dome in Galway. . . . .	71
5.5	Layout of the single star SCIDAR system. . . . .	72
5.6	Sequenced generalised single star SCIDAR. . . . .	73
5.7	Scintillation pattern for no pupil defocus. . . . .	74
5.8	Average scintillation pattern at the pupil plane obtained over 2000 frames. . . . .	75
5.9	Mean autocorrelation. . . . .	76
5.10	Autocorrelation of the pupil function. . . . .	77
5.11	Corrected normalised autocorrelation. . . . .	78
5.12	One dimensional radial cuts autocorrelation. . . . .	78
5.13	One dimensional averaged autocorrelation. . . . .	79
5.14	Concatenated autocorrelations. . . . .	79

6.1	Phase screen with $\frac{D}{r_0} = 13$ . . . . .	81
6.2	Phase screen with $\frac{D}{r_0} = 50$ . . . . .	82
6.3	Structure function. . . . .	83
6.4	Propagation through one turbulent layer. . . . .	84
6.5	Simulated scintillation patterns for different measurement planes. . . . .	88
6.6	Simulated 2 dimensional normalised autocorrelation for 5 five different conjugation planes. . . . .	89
6.7	Simulated average autocorrelation cuts for 5 five different conjugation planes. . . . .	90
7.1	SCIDAR data frames of Capella. . . . .	92
7.2	Scintillation Capella at 5.8km. . . . .	92
7.3	Estimated $C_n^2(h)$ profiles for 4 different noise level. . . . .	93
7.4	Simulated autocorrelations single star SCIDAR data. . . . .	94
7.5	Simulated autocorrelations single star SCIDAR data with added noise. . . . .	95
7.6	Average autocorrelation for the bright star Capella ( $m_v \simeq 0.08$ ). . . . .	96
7.7	Average autocorrelation for $\delta$ Andromeda (magnitude 3.27). . . . .	97
7.8	Estimated $C_n^2(h)$ profile using Capella for a binning $\times 2$ . . . . .	98
7.9	Estimated $C_n^2(h)$ profile using Capella for a binning $\times 4$ . . . . .	99
7.10	Estimated $C_n^2(h)$ profile using $\delta$ Andromeda for a binning $\times 4$ . . . . .	100
7.11	Error estimation for Capella data binning $\times 2$ . . . . .	101
7.12	Error estimation for Capella data binning $\times 4$ . . . . .	101
7.13	Error estimation for $\delta$ Andromeda data binning $\times 4$ . . . . .	102

---

# Chapter 1

## Introduction

---

### 1.1 Introduction

The Earth's atmosphere is a turbulent medium organised in layers. The sun's heat warms the Earth's surface, then heated air masses are in motion. At night, regions of approximately the same refractive index are formed, organised in strata of turbulent eddies. Those different eddies are changing intrinsically in time and are carried by the wind. Astronomical scintillation is the variation in apparent luminosity of a distant object, such as a star, viewed through the atmosphere. Scintillation is caused almost exclusively by small temperature variations (on the order of 0.1-1 Kelvin) in the atmosphere, resulting in index-of-refraction fluctuations. The undulation in the atmosphere acts as a lens focussing and defocussing of the light.

The effect of the atmosphere on an observed image is to blur the image. Adaptive optics is a technique to compensate the distortion of the wavefront introduced by the atmosphere using deformable elements.

SCIDAR (SCIntillation Detection And Ranging) is a remote sensing technique that uses an analysis of the scintillation to characterise the three-dimensional structure of the atmosphere by estimation of the refractive index structure constant as a function of altitude,  $C_n^2(h)$ .

For imaging systems using adaptive optics, a knowledge of the turbulence from the ground layer up to  $\simeq 20$  km is of great importance. The effect of the whole atmosphere can be quantified by the seeing (measure of the  $C_n^2(h)$  integrated over all layers of the atmosphere), which is the angular resolution of long-exposure images, but such a quantity is not enough. The seeing is related to the coherence length of the wavefront, the Fried parameter  $r_0$ . Other parameters, such as the isoplanatic



angle  $\theta_0$ , the angular distance on the sky over which wavefront distortions are correlated, can be found as a weighted integration over  $C_n^2(h)$ . The wind speed of the layers can be retrieved from SCIDAR instrument as well giving the coherence time of the turbulence useful for interferometric system. Atmospheric profilers such as SCIDAR are very useful for the characterisation of astronomical sites[63, 31], interferometry and (multi-conjugate) adaptive optics systems performance[26, 30].

The SCIDAR technique records scintillation patterns that are reduced to auto-correlation functions that are functions of  $C_n^2(h)$ . The solution, or inverse problem, is not well-posed, meaning that a direct inversion is really sensitive to noise. A solution can be approximated by a regularisation technique. The reconstruction of the profile depends on the assumed noise statistics and the available object prior information.

In this thesis we describe the principle of single star SCIDAR, a technique derived from the double star SCIDAR using a single star as a source. Arguments for the feasibility of the technique can be found in an unpublished paper of Klückers [48], and in the Ph.D thesis of R. A. Johnston[44]. The aim of the project is to build and demonstrate the feasibility of generalised single star SCIDAR. The instrument is a 25 cm telescope with an imaging system at its back conjugating sequentially to 5 pupil heights. The conjugation to the required pupil heights the camera is moved by means of a stepper motor controlled stage laterally along the optical axis of the system. The single star SCIDAR instrument was designed and constructed by Derek Coburn[18, 19, 17], a researcher in Applied Optics Group, in consultation with myself and Prof. Dainty. In order to retrieve the  $C_n^2(h)$  profile from the autocovariance functions an inverse problem has to be solved. Simulations of scintillation pattern (forward problem) using Fresnel diffraction are made. An inversion program is written for the reduced autocovariance functions using Tikhonov regularisation. Finally the program has been tested on real data.

## 1.2 Thesis organisation

**Chapter 2** gives an introduction to Fourier optics and randomness. That is motivated by the fact that atmosphere is a changing medium thus expressions are

treated statistically. The notion of convolution is an important concept in atmospheric optics and correlation is the key concept for SCIDAR instrument and turbulent profilers in general.

**Chapter 3** treats atmospheric turbulence properties for astronomy that were studied by Fried and Kolmogorov providing quantities of interest. The concept of double star SCIDAR [73] will be laid out then the principle of the single star SCIDAR will be introduced.

**Chapter 4** introduces the tools for retrieving the  $C_n^2(h)$  profile. The inverse problem will be treated and more especially the Tikhonov regularisation technique.

**Chapter 5** describes the single star SCIDAR system, and the data processing used to reduce the scintillation images to autocorrelations.

**Chapter 6** describes the simulations using Fresnel diffraction of wave propagation through atmospheric turbulence to obtain scintillation patterns for the single star SCIDAR technique.

**Chapter 7** presents results of  $C_n^2(h)$  profiles obtained from the simulated data and from real data gathered during a campaign at the Observatorio del Roque de los Muchachos, on La Palma island.

**Chapter 8** gives the conclusions of the work of this thesis.

**Appendix A** gives properties of Hilbert spaces and  $\mathbb{L}_2$  spaces used for the inverse problem.

## Presentations and publications

D. Coburn, D. Garnier, and J. C. Dainty. Development of a Single Star SCIDAR system for profiling atmospheric turbulence. *Atmosphere knowledge and Adaptive Optics for 8 to 100 m telescopes, ESO Mini Workshop, Garching, October 2003.*

---

D. Garnier, D. Coburn, and J. C. Dainty. Single star SCIDAR for  $C_n^2(h)$  profiling. In *Atmospheric Optical Modeling, Measurement, and Simulation. Proc. SPIE, Vol. 5891:20-26*, 2005.

D. Coburn, D. Garnier, and C. Dainty. Development and modelling of a single star SCIDAR system for profiling atmospheric turbulence. In *Laser and Optical Systems for Astronomy and Space-Based Instrumentation II, Proc. FiO and Laser Science.*, 2005.

D. Coburn, D. Garnier, and J. C. Dainty. A single star SCIDAR system for profiling atmospheric turbulence. In *Optics in Atmospheric Propagation and Adaptive Systems VIII. Proc. SPIE, Vol. 5981:105-114*, 2005.

## Statement of originality

The material in this thesis has not previously been submitted for a degree or diploma in any university. To the best of my knowledge and belief, the thesis contains no material previously published or written by another person, except when due reference is made in the text.

---

# Chapter 2

## Mathematical background

---

This chapter presents some mathematical background in Fourier optics, linear systems and the theory of random processes.

### 2.1 Fourier optics

Real-world objects can be represented by functions. We will consider only scalar-valued functions. We shall use the symbol  $f(\mathbf{r})$  to represent an object, where  $\mathbf{r}$  is one or more spatial coordinates and possibly time. The functions represent different quantities such as temperature, index of refraction, phase, amplitude complex of a field or the irradiance.

#### 2.1.1 Fourier transform

The one dimensional Fourier transform of a function  $f(x)$  of the real variable  $x$ , denoted  $F(u)$ ,  $\tilde{f}(u)$ , or  $\mathcal{F}\{f(x)\}$ , is defined by

$$\tilde{f}(u) = \int_{-\infty}^{+\infty} f(x)e^{-2i\pi ux} dx \quad (2.1)$$

where  $u$  is frequency. The inverse Fourier transform of  $\tilde{f}(u)$ , is defined as

$$f(x) = \mathcal{F}^{-1}\{\tilde{f}(u)\} = \int_{-\infty}^{+\infty} \tilde{f}(u)e^{+2i\pi ux} dx \quad (2.2)$$

The definitions Eq.(2.1) and Eq.(2.2) are meaningful if the function  $f(x)$  is absolutely integrable ie,  $\int_{-\infty}^{+\infty} |f(x)|dx < \infty$  and any discontinuities of  $f(x)$  are not infinite. The presence of the integral in the two definitions, raises the existence conditions of such transform. There is a set of sufficient conditions[34], with the

different sets of conditions where  $f$  must be integrable and  $f$  must have no infinite discontinuities. Consider a function  $f(x)$  that is square integrable, meaning its  $\mathbb{L}_2$  norm exists (i.e.  $f$  lies in a Hilbert  $\mathbb{L}_2$  space (section 4.1 for more details on Hilbert space)  $\| \mathbf{f} \|_2 = \left[ \int_{-\infty}^{+\infty} |f(x)|^2 dx \right]^{\frac{1}{2}} < \infty$ . This condition is sufficient.

However physical realizability is a valid sufficient condition for the existence of a Fourier transform[13].

### 2.1.1.1 Some properties of the Fourier transform

Consider two functions  $f(x)$  and  $h(x)$ , and their respective Fourier transforms  $\tilde{f}(u)$  and  $\tilde{h}(u)$ .

#### Symmetries

$$\mathcal{F}\{f(-x)\} = \tilde{f}(-u) \quad (2.3)$$

$$\mathcal{F}\{f^*(x)\} = \tilde{f}^*(-u) \quad (2.4)$$

$$\mathcal{F}\{f^*(-x)\} = \tilde{f}^*(u) \quad (2.5)$$

$$\mathcal{F}\{\tilde{f}(u)\} = f(-x) \quad (2.6)$$

The star on the function means complex conjugate.

#### Linearity theorem

The Fourier transform is a linear operation. For  $\alpha$  and  $\beta$ , two scalars.

$$\mathcal{F}\{\alpha f(x) + \beta h(x)\} = \alpha \mathcal{F}\{g(x)\} + \beta \mathcal{F}\{h(x)\} \quad (2.7)$$

#### Similarity theorem

For  $a$  real and positive

$$\mathcal{F}\{f(ax)\} = \frac{1}{a} \tilde{f}\left(\frac{u}{a}\right) \quad (2.8)$$

If you squeeze in one space you stretch in the other one, and vice-versa.

**Shift theorem**

$$\mathcal{F}\{f(x - a)\} = \tilde{f}(u)e^{-2i\pi ua} \quad (2.9)$$

We have the Fourier transform of the unshifted function,  $\tilde{f}(u)$ , multiplied by a complex exponential. The modulus stays the same, but a linear phase factor appears.

**Parseval's theorem**

$$\int_{-\infty}^{+\infty} |f(x)|^2 dx = \int_{-\infty}^{+\infty} |\tilde{f}(u)|^2 du \quad (2.10)$$

This theorem states that the energy is conserved between the two spaces. We can define, as well, the **generalised Parseval's theorem**

$$\int_{-\infty}^{+\infty} f(x)h^*(x)dx = \int_{-\infty}^{+\infty} \tilde{f}(u)\tilde{h}^*(u)du \quad (2.11)$$

**2.1.1.2 Circular symmetric functions**

Previously the Fourier transform was defined for one variable  $x$ . For a two dimensional or three dimensional variables  $\mathbf{r}$  (time as well can be added) the definition of the Fourier Transform is modified with an integration over the other dimensions. The properties above still hold.

$$\tilde{f}(\boldsymbol{\rho}) = \int_{-\infty}^{+\infty} f(\mathbf{r}) e^{-2i\pi\boldsymbol{\rho}\cdot\mathbf{r}} d\mathbf{r} \quad (2.12)$$

where  $\boldsymbol{\rho}$  is a multidimensional frequency. For a rotationally symmetric function  $f(\mathbf{r})$  we can write it as  $f(r = |\mathbf{r}|)$  we can define another transform called, the Hankel transform defined as follows

$$\mathcal{H}\{f(r)\} = 2\pi \int_0^{+\infty} r f(r) J_0(2\pi r \rho) dr, \quad (2.13)$$

where  $\rho = |\boldsymbol{\rho}|$  and  $J_0$  is the Bessel function of the first kind and of zero order.

$$J_0(z) = \frac{1}{\pi} \int_0^\pi e^{-iz \cos \theta} d\theta \quad (2.14)$$

## 2.1.2 Fourier transform of some functions

### 2.1.2.1 Circle function

The circle function is defined as

$$\text{circ}(r) = \begin{cases} 1 & r < 1 \\ \frac{1}{2} & r = 1 \\ 0 & \text{otherwise} \end{cases} \quad (2.15)$$

where  $r = \sqrt{x^2 + y^2}$ . Its Fourier transform is given by

$$\widetilde{\text{circ}}(\rho) = 2\pi \frac{J_1(2\pi\rho)}{2\pi\rho} \quad (2.16)$$

$J_1$  is the Bessel function of the first kind of first order.

### 2.1.2.2 Gaussian function

A normalised two dimensional Gaussian with a variance  $\sigma^2$  is written

$$\text{gaus}(r) = \frac{1}{2\pi\sigma^2} \exp\left(-\frac{r^2}{2\sigma^2}\right) \quad (2.17)$$

The we can show that the Fourier transform is given by

$$\widetilde{\text{gaus}}(\rho) = \exp(-2\pi^2\sigma^2\rho^2) \quad (2.18)$$

It is also a Gaussian.

## 2.1.3 Convolution and correlation

The one dimensional convolution of two functions  $f(x)$  and  $h(x)$ , denoted  $f * h$ ,  $[f * h](x)$ ,  $c(x)$  or  $f(x) * h(x)$ , is defined by

$$c(x) = \int_{-\infty}^{+\infty} f(x')h(x-x')dx' \quad (2.19)$$

$$= \int_{-\infty}^{+\infty} f(x-x'')h(x'')dx'' \quad (2.20)$$

The two definitions reflect the commutative property of the convolution. We can note the reversal ( $(x-x')$  instead of  $(x'-x)$ ) that makes the substitution possible, in contrast to correlation (section 2.1.3.2).



### 2.1.3.1 Convolution theorem

Consider two functions  $f(x)$  and  $h(x)$ , and their respective Fourier transforms  $\tilde{f}(u)$  and  $\tilde{h}(u)$ . The convolution theorem states:

$$\mathcal{F}\{f(x) * h(x)\} = \tilde{f}(u) \tilde{h}(u) \quad (2.21)$$

The convolution in the direct space corresponds to a multiplication in the Fourier space, and vice versa. The Fourier transform of a convolution equals the product of the transforms.

The one dimensional correlation (called sometimes *cross-correlation*) of two functions  $f(x)$  and  $h(x)$ , denoted  $f(x) \star h(x)$  is defined by

$$f(x) \star h(x) = \int_{-\infty}^{+\infty} f(x') h^*(x' - x) dx' = \int_{-\infty}^{+\infty} f^*(x + x'') h(x'') dx'' \quad (2.22)$$

The five-pointed star, or pentagram, denotes correlation. There is no reversal compared to the convolution. One thing to notice is the correlation is not commutative, unlike the convolution.  $f(x) \star h(x)$  does not necessarily equal  $h(x) \star f(x)$ . The link between (cross) correlation and convolution[10, 13] is the following:

$$f(x) \star h(x) = f^*(-x) * h(x) \quad (2.23)$$

In the case of statistical fluctuations of the electromagnetic wave, due to incoherent source or atmosphere turbulence, quantities such as correlation can be expressed as an ensemble average over all possible realisations. When we consider random variables, the average  $\langle f(u) h^*(u - x) \rangle$  is used instead of the infinite integral, and this will be discussed later in this chapter. We can consider the case of the correlation of the same function with itself. The autocorrelation is then

$$f(x) \star f(x) = f^*(-x) * f(x) \quad (2.24)$$

Autocorrelation can be shown to be maximum at the origin, i.e.  $x = 0$ .

### 2.1.3.2 Autocorrelation theorem

Consider the function  $f(x)$  and its Fourier transform  $\tilde{f}(u)$ . Using the Fourier transform property

$$\mathcal{F}\{f(x) \star f(x)\} = |\tilde{f}(u)|^2 \quad (2.25)$$

### 2.1.4 Energy and power spectra

The three dimensional energy spectrum, or spectral density  $\Phi$ , of the wave function  $f(\mathbf{r})$  is defined by

$$\Phi(\boldsymbol{\rho}) = |\tilde{f}(\boldsymbol{\rho})|^2 \quad (2.26)$$

It is the square modulus of the Fourier transform of the wave function. Thus, the phase information is lost, for a complex wave function.

The power spectrum (a statistical quantity) is the ensemble average of the energy spectrum

$$\Phi(\boldsymbol{\rho}) = \langle |\mathcal{F}\{\Psi(\mathbf{r})\}|^2 \rangle \quad (2.27)$$

By looking at Eq.(2.25), we can see that the Fourier transform of the statistical autocorrelation of wave function is the power spectrum.

### 2.1.5 Sampling theorem

The sampling theorem states that a bandlimited function, i.e. a function whose Fourier transform is zero for  $|f| > f_{\max}$ , if it is to be fully specified, must be sampled at a rate greater than twice the maximum frequency  $f_s > 2f_{\max}$ . Equivalently the sampling interval must be  $\delta x \leq \frac{1}{2f_{\max}}$

## 2.2 Linear system theory

Physical processes may be modelled by linear systems theory. If  $f(x, y)$  denotes the input of the system, the output  $g(x, y)$  is given by

$$g(x, y) = \mathcal{S}f(x, y), \quad (2.28)$$

where  $\mathcal{S}$  is the operator of the system. A linear system obeys the principle of superposition, that is the response to an input decomposed into a sum of elementary functions, is equal to the sum of the responses to each elementary input functions.

$$\mathcal{S} \left( \sum_j c_j f_j(x, y) \right) = \sum_j c_j \mathcal{S}f_j(x, y) \quad (2.29)$$

### 2.2.1 Point spread function

Let consider an optical system, which is linear in intensity (incoherent imaging) or complex amplitude (coherent imaging). Let us keep the general case where the system can be shift-variant (space-variant) or shift-invariant (space-invariant).  $f$  is the function representing the two dimensional object and  $g$  is the function representing the two dimensional image.  $f$  and  $g$  are assumed to be square integrable. Then, the functions lie in  $\mathbb{L}_2$  and

$$g(\mathbf{r}) = \int_{-\infty}^{+\infty} h(\mathbf{r}, \mathbf{r}') f(\mathbf{r}') d\mathbf{r}' \quad (2.30)$$

or in operator form

$$\mathbf{g} = \mathcal{H}\mathbf{f} \quad (2.31)$$

We can decompose the object function  $f$  in elementary elements. Those elements are the delta functions,  $\delta$ , that can be regarded as basis functions for the  $\mathbb{L}_2$ . If we know the response for an elementary element we know it for the whole object. The resultant field for a elementary element (delta function) is called the *impulse response function* or *point spread function* (PSF) in optics.

$$h(\mathbf{r}, \mathbf{r}_0) = \int h(\mathbf{r}, \mathbf{r}') \delta(\mathbf{r}' - \mathbf{r}_0) d\mathbf{r}' \quad (2.32)$$

#### 2.2.1.1 Shift-invariant systems

In optical imaging, a shift-invariant (stationary) optical system is usually called isoplanatic. Isoplanaticity requires that the point spread function is the same for all field angles. In practice, a system can be defined to be isoplanatic only over a region where the aberrations are sensibly constant. For a shift-invariant system,  $h(\mathbf{r}, \mathbf{r}')$  only depends on the difference between the two points  $\mathbf{r}$  and  $\mathbf{r}'$ . The image  $h(\mathbf{r}, \mathbf{r}')$  of a point source located at  $\mathbf{r}'$  is translated by  $\mathbf{r}'$  of the image  $h(\mathbf{r}, \mathbf{0})$  of a point source located at the origin of the object plane.  $h(\mathbf{r}, \mathbf{r}') = h(\mathbf{r} - \mathbf{r}', \mathbf{0})$ , where the zero second argument can be dropped to become  $h(\mathbf{r} - \mathbf{r}')$ . The point spread function (PSF) is then defined as

$$h(\mathbf{r}) = \int_{-\infty}^{+\infty} h(\mathbf{r} - \mathbf{r}') \delta(\mathbf{r}') d\mathbf{r}' \quad (2.33)$$

Then, Eq.(2.30) becomes a convolution

$$g(\mathbf{r}) = \int_{-\infty}^{+\infty} h(\mathbf{r} - \mathbf{r}') f(\mathbf{r}') d\mathbf{r}' \quad (2.34)$$

We can write it in the convolution formalism discussed above as

$$g(\mathbf{r}) = f(\mathbf{r}) * h(\mathbf{r}) \quad (2.35)$$

In Eq.(2.35),  $f$ ,  $g$  represent either intensities (incoherent imaging) or complex amplitudes (coherent imaging).

### 2.2.2 Transfer functions

The *transfer function* of a linear isoplanatic system is the Fourier transform of the point spread function,  $\tilde{h}(\boldsymbol{\rho})$ .

$$\text{TF}(\boldsymbol{\rho}) = \tilde{h}(\boldsymbol{\rho}) \quad (2.36)$$

The *optical transfer function* (OTF) is defined as the normalised *transfer function*.

$$\text{OTF}(\boldsymbol{\rho}) = \frac{\tilde{h}(\boldsymbol{\rho})}{\tilde{h}(0)} \quad (2.37)$$

A property of the Fourier transform, is that if the function  $f$  is real, its Fourier transform  $\tilde{f}$  is Hermitian. The *modulation transfer function* (MTF) is defined as the modulus of the optical transfer function.

$$\text{MTF}(\boldsymbol{\rho}) = \frac{|\tilde{h}(\boldsymbol{\rho})|}{\tilde{h}(0)} = |\text{OTF}(\boldsymbol{\rho})| \quad (2.38)$$

The MTF expresses the ratio of the output modulation to the input modulation.

$$\text{MTF}(\boldsymbol{\rho}) = \frac{M_g}{M_f} \quad (2.39)$$

where  $M_f$  is the *modulation* of the function  $f$  defined as,

$$M_f = \frac{f_{max} - f_{min}}{f_{max} + f_{min}} \quad (2.40)$$

For incoherent imaging, the OTF of the optical system is given by the autocorrelation of the pupil function,  $P(\mathbf{r})$ .  $\text{OTF}_P(\boldsymbol{\xi} = \frac{\mathbf{r}}{\lambda f_T}) = P(\mathbf{r}) * P^*(-\mathbf{r})$ , where  $f_T$  is the focal length.

## 2.3 Random variables

In this section we will consider random variables, i.e. variables that are the results of some non-deterministic process or experiment. A random variable can be continuous

(taking values over a continuous range such as intensity of atmospherically induced scintillation) or discrete (taking values from a discrete set such as photon counts in a detector).

### 2.3.1 Probability functions

The probability of a random variable,  $X$ , to have a value less or equal to a specific value  $x$  is given by

$$F_X(x) = \Pr(X \leq x) \quad (2.41)$$

where  $\Pr(\cdot)$  is the probability and  $F(\cdot)$  is the *cumulative distribution function* (cdf) of the random variable  $X$ . We can define the probability for  $X$  to be between the values  $x$  and  $x + dx$ , dropping the subscript notation  $X$  in the cumulative distribution function,

$$\Pr(x < X \leq x + dx) = F(x + dx) - F(x) \quad (2.42)$$

The probability density function is defined as the derivative of the cumulative density function at the points where the derivative exists

$$p(x) = \frac{dF(x)}{dx} \text{ almost everywhere.} \quad (2.43)$$

$p(x)dx$  is the probability that the random variable  $X$  lies between  $x$  and  $x + dx$ .

#### Properties of the probability density function

1.  $p(x)$  is positive;  $p(x) \geq 0$
2.  $p(x)$  is normalised;  $\int_{-\infty}^{+\infty} p(x) dx = 1$

If we consider now, instead of a continuous random variable, a discrete random variable,  $x$  with a set of realisations (outcomes)  $\{x_1, x_2, \dots, x_M\}$  or a countably infinite set  $\{x_i, i = 1, \dots, \infty\}$ , the cumulative density function is the following

$$F(x) = \sum_{x_i \leq x} p(x_i) \delta(x - x_i) \quad (2.44)$$

### 2.3.2 Moments

The *expectation value* of a continuous random variable  $x$ , also called the *mean*, denoted  $\langle x \rangle$ ,  $\bar{x}$  or  $E\{x\}$  is defined by

$$E\{x\} = \langle x \rangle = \bar{x} = \int_{-\infty}^{+\infty} x p(x) dx \quad (2.45)$$

$E$  and  $\langle \rangle$  denote the statistical expectation operator or the ensemble average. For a discrete random variable  $x$  the mean is defined by

$$E\{x\} = \sum_i x_i \Pr(x_i) \quad (2.46)$$

We can define general higher order moments,  $E\{x^n\}$ , or  $\langle x^n \rangle$

$$E\{x^n\} = \langle x^n \rangle = \int_{-\infty}^{+\infty} x^n p(x) dx \quad (2.47)$$

#### 2.3.2.1 Central moments

We can define moments that are centred around the mean,  $\bar{x}$ .

$$E\{(x - \bar{x})^n\} = \langle (x - \bar{x})^n \rangle = \int_{-\infty}^{+\infty} (x - \bar{x})^n p(x) dx \quad (2.48)$$

An important parameter is the second order central moment called *variance*, often denoted  $\sigma^2$ , which is a measure of the spread of the random variable around its mean.

$$\sigma^2 = \text{Var}\{x\} = E\{(x - \bar{x})^2\} = \int_{-\infty}^{+\infty} (x - \bar{x})^2 p(x) dx \quad (2.49)$$

One can show that

$$\sigma^2 = \langle x^2 \rangle - \langle x \rangle^2 \quad (2.50)$$

Note that the variance is the square of the *standard deviation*,  $\sigma$ .

### 2.3.3 Joint probability

We can consider the probability of two events A and B both occurring. The corresponding *joint probability* is denoted  $\Pr(A \cap B)$  or  $\Pr(A, B)$ . The intersection of outcomes between event A and B is the same as that between B and A (commutativity). If the random variables are *statistically independent* the joint probability becomes

the product of the probabilities of the two variables.  $\Pr(B, A) = \Pr(A) \Pr(B)$ . The two-dimensional cumulative distribution function is written

$$F(x, y) = \int_{-\infty}^x \int_{-\infty}^y p(x', y') dx' dy' \quad (2.51)$$

$$p(x, y) = \frac{\partial^2}{\partial x \partial y} F(x, y) \quad (2.52)$$

In the case of two statistically independent, the joint PDF and the joint cdf of the two random variable are equal to their product, as in the case of the probability.

### 2.3.4 Joint moments

The joint moments of two random variables  $x$  and  $y$  and denoted  $\langle x^n y^m \rangle$  are defined by

$$\langle x^n y^m \rangle = \int_{-\infty}^{+\infty} \int_{-\infty}^{+\infty} x^n y^m p(x, y) dx dy \quad (2.53)$$

The first joint moment is the *correlation* of the two variables

$$\langle xy \rangle = \int_{-\infty}^{+\infty} \int_{-\infty}^{+\infty} x y p(x, y) dx dy \quad (2.54)$$

The *covariance* is the first order central joint moment.

$$\begin{aligned} \langle (x - \bar{x})(y - \bar{y}) \rangle &= \int_{-\infty}^{+\infty} \int_{-\infty}^{+\infty} (x - \bar{x})(y - \bar{y}) p(x, y) dx dy \\ &= \langle xy \rangle - \langle x \rangle \langle y \rangle \end{aligned} \quad (2.55)$$

With the two equations, we can define the *correlation coefficient*, which is the normalised covariance.

$$\rho = \frac{\langle (x - \langle x \rangle)(y - \langle y \rangle) \rangle}{\sigma_x \sigma_y} \quad (2.56)$$

The correlation coefficient lies between 0 and 1.

### 2.3.5 Conditional probability and Bayes' rule

We can consider the probability of an event  $A$  has occurred considering event  $B$  has occurred. We can say conversely, what is the probability of event  $A$ , given event  $B$  occurred. The probability is denoted  $\Pr(A|B)$  and is defined as

$$\Pr(A|B) = \frac{\Pr(A, B)}{\Pr(B)}, \quad (2.57)$$

if  $\Pr(B) \neq 0$ . This can be written as

$$\Pr(A, B) = \Pr(B) \Pr(A|B) \quad (2.58)$$

$\Pr(A|B)$  is a probability *a posteriori*. It needs the knowledge first of the prior probability  $\Pr(B)$  of  $B$ . The conditional probability  $\Pr(A|B)$  is in general different from the probability *a priori*  $\Pr(A)$ . Those two probability can be related, expressing the conditional probability,  $\Pr(B|A)$ , of event  $B$  given event  $A$  occurred. As  $\Pr(A, B) = \Pr(B, A) = \Pr(A) \Pr(B|A)$ , it comes

$$\Pr(B|A) = \frac{\Pr(A|B) \Pr(B)}{\Pr(A)} \quad (2.59)$$

Eq.(2.59) is *Bayes' rule*.

## 2.4 Random processes

We consider now a process that has a set of outcomes to be described, where each outcome is a random variable in time or space, or both. Let  $\mathbf{f}$  be a  $M$ -dimensional random vector, constituted of  $M$  scalar random variables,  $\mathbf{f} = \{f_i, i = 1, \dots, m\}$ . each  $f_i$  take values in  $(-\infty, +\infty)$ . If the random variable is continuous, it becomes  $f(\mathbf{r})$  where  $f$  is a function with different realisation at point  $\mathbf{r}$ . The variable  $\mathbf{r}$  can represent time, space or both unless it is stated. The value of a random process at one point is a random variable. Moments are defined as follows

$$E\{[f(\mathbf{r})]^n\} = \langle [f(\mathbf{r})]^n \rangle = \int_{-\infty}^{+\infty} [f(\mathbf{r})]^n p[f(\mathbf{r})] df(\mathbf{r}) \quad (2.60)$$

### 2.4.1 Multiple-point expectations

The expectation for two points is given by

$$E\{f(\mathbf{r}_1)f(\mathbf{r}_2)\} = \langle f(\mathbf{r}_1)f(\mathbf{r}_2) \rangle = \int_{-\infty}^{+\infty} \int_{-\infty}^{+\infty} f(\mathbf{r}_1)f(\mathbf{r}_2) p[f(\mathbf{r}_1), f(\mathbf{r}_2)] df(\mathbf{r}_1)df(\mathbf{r}_2), \quad (2.61)$$

where  $f(\mathbf{r}_1)$  and  $f(\mathbf{r}_2)$  are two random variables and  $p[f(\mathbf{r}_1), f(\mathbf{r}_2)]$  is their joint density.



## 2.4.2 Covariance and correlation

For the continuous case of two random processes  $f(\mathbf{r})$  and  $g(\mathbf{r}')$  we talk about the *cross-correlation function* defined as

$$R_{fg}(\mathbf{r}, \mathbf{r}') = \langle f(\mathbf{r})g^*(\mathbf{r}') \rangle \quad (2.62)$$

The *cross-covariance function* is defined as

$$K_{fg}(\mathbf{r}, \mathbf{r}') = \langle [f(\mathbf{r}) - \langle f(\mathbf{r}) \rangle][g^*(\mathbf{r}') - \langle g^*(\mathbf{r}') \rangle] \rangle = R_{fg}(\mathbf{r}, \mathbf{r}') - \bar{f}(\mathbf{r})\bar{g}^*(\mathbf{r}') \quad (2.63)$$

In the atmospheric case, we often consider the autocorrelation or the autocovariance, and an important function for the study of the fluctuations of different quantities. The autocorrelation function of a random process  $f(\mathbf{r})$  is defined by

$$R_f(\mathbf{r}_1, \mathbf{r}_2) = \langle f(\mathbf{r}_1)f^*(\mathbf{r}_2) \rangle \quad (2.64)$$

The autocovariance is defined by

$$\begin{aligned} K_f(\mathbf{r}_1, \mathbf{r}_2) &= \langle [f(\mathbf{r}_1) - \langle f(\mathbf{r}_1) \rangle][f^*(\mathbf{r}_2) - \langle f^*(\mathbf{r}_2) \rangle] \rangle \\ &= R_f(\mathbf{r}_1, \mathbf{r}_2) - \bar{f}(\mathbf{r}_1)\bar{f}^*(\mathbf{r}_2) \end{aligned} \quad (2.65)$$

We find for  $\mathbf{r}_1 = \mathbf{r}_2 = \mathbf{r}$  the variance defined by

$$K_f(\mathbf{r}, \mathbf{r}) = \langle |[f(\mathbf{r}) - \langle f(\mathbf{r}) \rangle]|^2 \rangle = R_f(\mathbf{r}, \mathbf{r}) - |\bar{f}(\mathbf{r})|^2 \quad (2.66)$$

For the discrete case we speak about the *covariance matrix*, which is the generalization of a univariate variance.

$$K_{ij} = \langle (f_i - \bar{f}_i)(f_j - \bar{f}_j)^* \rangle, \quad (2.67)$$

where the asterisk indicates the complex conjugate, in the case of  $f$  being complex. The diagonal elements of the covariance matrix,  $K_{ii}$  are the variances  $\sigma_i^2$ .

$$K_{ii} = \text{Var}\{f_i\} = \langle |f_i - \bar{f}_i|^2 \rangle \quad (2.68)$$

### 2.4.2.1 Stationarity, isotropy and ergodicity

The atmosphere provides neither homogeneous (spatial-stationarity) nor isotropic random variables (first-order temporal and spatial statistics), but we can assume a local isotropy and stationarity, over a region comparable to the outer scale  $L_0$ [67]. Temporally, the functions  $f(\mathbf{r})$  can be assumed to be stationary over time increments or stationary increments[35], for some restricted time period.

### 2.4.2.2 Stationarity

Stationarity in the *wide sense* requires that the mean and autocorrelation have no preferred origin, that is the mean is a constant and the autocovariance Eq.(2.64) depends on the vector difference of the coordinates.

$$\langle f(\mathbf{r}) \rangle = \bar{f}; \quad (2.69)$$

$$R(\mathbf{r}_1, \mathbf{r}_2) = R(\mathbf{r}_1 - \mathbf{r}_2); \quad (2.70)$$

If all  $n$  point probability distribution functions at a fixed time or position are the same for all times or positions, the process is said *strictly* stationary. It is more restrictive than wide-sense stationarity. We can write the autocorrelation and autocovariance  $R_f/K_f(\mathbf{r}_1, \mathbf{r}_2) = R_f/K_f(\mathbf{r}_1 - \mathbf{r}_2) = R_f/K_f(\Delta\mathbf{r})$ . *In the atmospheric literature the autocorrelation  $R_f(\Delta\mathbf{r})$  is often denoted as  $B_f(\Delta\mathbf{r})$ .*

$$K_f(\Delta\mathbf{r}) = \langle [f(\mathbf{r}) - \langle f(\mathbf{r}) \rangle][f^*(\mathbf{r} + \Delta\mathbf{r}) - \langle f^*(\mathbf{r} + \Delta\mathbf{r}) \rangle] \rangle \quad (2.71)$$

Atmospheric turbulence is a random process where turbulence induced perturbations are often assumed to be wide sense stationary.

The autocorrelation is related to the power spectrum by a Fourier transform relation by the *Wiener-Khintchine theorem* defined as

$$\Phi(u) = \mathcal{F}\{R(\Delta x)\} = \int_{-\infty}^{+\infty} \langle f(x)f^*(x + \Delta x) \rangle e^{-2i\pi u\Delta x} d\Delta x \quad (2.72)$$

### 2.4.2.3 Isotropy

Isotropy implies a symmetry in rotation where the spatial statistical quantity depending on the vector  $\mathbf{r}$  can be represented by the modulus  $r = |\mathbf{r}|$ . If the process is stationary, the autocovariance or autocorrelation between two points in space will only depend on the modulus of the separation vector.

### 2.4.2.4 Ergodicity

A stationary random process is said to be ergodic if ensemble averages can be replaced by time averages. This implies that such realisation contains all the essential statistical parameters of the whole process.

## 2.4.3 Some distributions

### 2.4.3.1 Normal distribution

We consider a continuous random vector  $\mathbf{g} \in \mathbb{R}^M$  ( $\mathbb{R}^M$  is the  $M$ -dimensional vector space of real numbers). The normal (Gaussian) multivariate normal PDF of a vector  $\mathbf{g}$  is written

$$p(\mathbf{g}) = [(2\pi)^M \det(\mathbf{K})]^{-\frac{1}{2}} \exp \left[ -\frac{1}{2} (\mathbf{g} - \bar{\mathbf{g}})^t \mathbf{K}^{-1} (\mathbf{g} - \bar{\mathbf{g}}) \right] \quad (2.73)$$

where  $\mathbf{K}$  is the  $M \times M$  covariance matrix of  $\mathbf{g}$  defined in Eq.(2.67) and where  $\bar{\mathbf{g}} = (\bar{g}_1, \dots, \bar{g}_M)$  is the vector of means. The subscript  $t$  denote the transpose and  $\bar{\mathbf{g}}$  is the mean vector of  $\mathbf{g}$ . If  $\mathbf{f}$  is real,  $\mathbf{K}$  is a symmetric matrix and a positive definite matrix.

### 2.4.3.2 Poisson distribution

A Poisson probability of a random vectors is applicable for random variables that are all independent. The Poisson probability for a discrete random vector is given by  $\mathbf{g} = g_1, \dots, g_M$  with independent components has the form

$$\Pr(\mathbf{g}) = \prod_{i=1}^M e^{-\bar{g}_i} \frac{(\bar{g}_i)^{g_i}}{g_i!}, \quad (2.74)$$

where  $\bar{g}_i, i = 1, \dots, M$  represent the mean (or the variance that equals the mean for Poisson probability).

### 2.4.3.3 Log-normal distribution

A variable  $\mathbf{g}$  is log-normal distributed if its natural logarithm  $\ln(\mathbf{g})$  is normally distributed. The distribution is

$$p(\mathbf{g}) = [(2\pi)^M \mathbf{g}^2 \det(\mathbf{K})]^{-\frac{1}{2}} \exp \left[ -\frac{1}{2} (\ln(\mathbf{g}) - \overline{\ln(\mathbf{g})})^t \mathbf{K}^{-1} (\ln(\mathbf{g}) - \overline{\ln(\mathbf{g})}) \right] \quad (2.75)$$

if we consider a one dimensional variable the distribution is

$$p(g) = \frac{1}{\sqrt{2\pi} \sigma_{\ln g}} \exp \left[ -\frac{1}{2} \frac{(\ln g - \overline{\ln(g)})^2}{\sigma_{\ln g}^2} \right] \quad (2.76)$$

The mean of a one dimensional variable log-normal distributed is given by

$$\bar{g} = \exp \left( \frac{2 \overline{\ln(g)} + \sigma_{\ln g}^2}{2} \right) \quad (2.77)$$

and the variance is given by

$$\text{Var}\{g\} = \exp\left(\overline{\ln(g)} + \sigma_{\ln g}^2\right) (\exp \sigma_{\ln g}^2 - 1) \quad (2.78)$$

---

# Chapter 3

## Atmospheric optics

---

In this chapter, atmospheric turbulence properties will be discussed. The intensity fluctuations of the light induced by refractive index fluctuations of the atmosphere (scintillation) will be treated before discussing the concept of a remote turbulent profiler based on scintillation patterns to quantify the values of the refractive index fluctuations of the atmospheric layers.

### 3.1 Atmospheric turbulence

The wavefront from starlight is distorted by atmospheric turbulence, due to random fluctuations of the refractive index of the air of the atmosphere. The optical strength of the atmospheric refractive index fluctuations,  $C_n^2(h)$ , determine the contribution of the effect on the wavefront. The fluctuations of the refractive index, depending on temperature, will cause random optical path length of the atmosphere in time and in space. The sun's heat warms the Earth's surface, then heated air masses are in motion. At night, regions of approximately the same turbulence strength are formed, organised in strata of turbulent eddies. Large turbulent eddies, having a unique temperature, are dissipated in smaller eddies in a random and continuous way.

#### 3.1.1 Structure of the atmosphere

The Earth's atmosphere is divided into several layers, characterised by their vertical distribution of temperature (Fig. 3.1). The portion of the lower atmosphere is called the troposphere. The troposphere is the most active region with a pronounced wind

motion, rich in water vapour and clouds, wherein the temperature is decreasing fairly regularly with respect to the altitude. Its size varies according to latitude, going from 7 km at poles up to 20 km at the equator. It is in this portion of the atmosphere that most of the weather occurs. There is a buffer zone named the tropopause, then starts the middle atmosphere including the stratosphere, where the temperature increases, up to about 50 km height and the mesosphere, where the temperature decreases. Beyond is the high atmosphere, formed by the thermosphere and the exosphere, characterised by an increasing temperature. We can consider that the Earth's atmospheric layer does not go above 1500 km. Weather phenomena occur in the troposphere and the lower stratosphere. With the fast decrease of the atmospheric pressure with the altitude, we can consider that 90% of the atmospheric mass is located under 16 km, and the 99% of it is under 30 km.

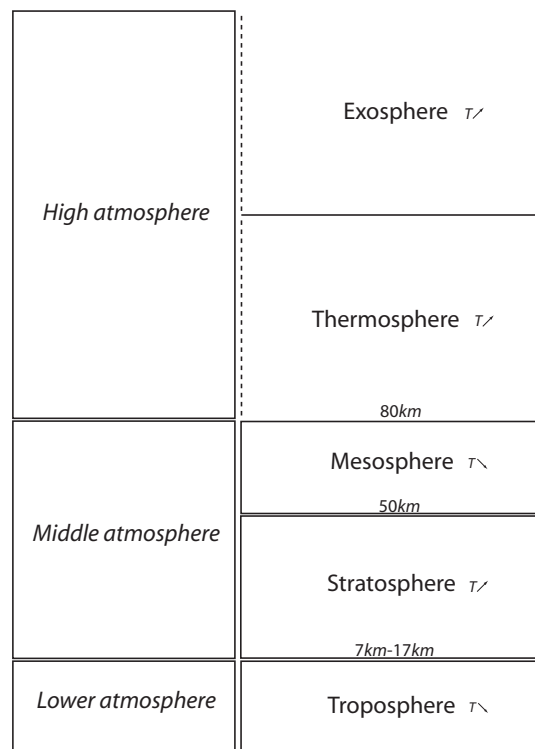


Fig. 3.1: Structure of the atmosphere.

### 3.1.2 Turbulent zones

Within the troposphere (*tropo-* comes from Greek meaning “turning”), the bottom layer, in contact with the surface of the earth, is called the atmospheric boundary layer (abbreviated BL, named also the ground layer (GL)). The horizontal forces of friction with the Earth’s relief, acting on the air movement that would keep the balance of the wind between the Coriolis force and the horizontal pressure gradient, modify the displacements and the exchanges of energy and mass within a layer thick of about 1500 m. An even lower layer, part of the boundary layer, exists called the surface (boundary) layer (SL), where the interactions between the surface and the wind are the strongest; its thickness is about 30 m. Ground-air friction is stronger where wind shear generate mechanical turbulence exceeding buoyant forces, and a differential temperature is present too due to warming during day time and cooling during night time. Above the atmospheric boundary layer is the free atmosphere (FA) where the effect of the surface friction on the air motion becomes less important. The dynamics are more complicated and turbulence depends on wind shear and gravity waves. The boundary layer is a big contribution of atmospheric turbulence. The importance of the contribution of the turbulence in the ground layer is significant, on the order of 60% found in different observatories[71].

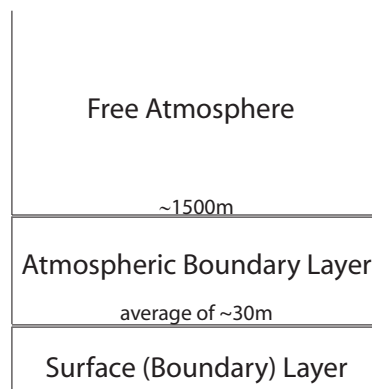


Fig. 3.2: Turbulent zones in the atmosphere.

### 3.1.3 Statistics of refractive index fluctuations

The effects of turbulence on imaging are important to understand in order to be able to model image formation, adaptive optics, etc. Consequently, the statistics of spatial and temporal structure of atmospheric turbulence are important. The understanding of turbulence is derived from fluid motion study. A fluid is laminar when the flow is smooth, regular and organised in parallel layers with few exchanges between them. The velocity inside the layers is constant. When the average velocity becomes higher, a fluid is turbulent. It shows irregularities in time and space. The fluid parcels deviate from the mean flow, with no apparent preferential direction or velocity, with a tendency to mix, becoming unstable and random. The fluid's behaviour is not predictable any more, and a statistical approach is needed to describe it. The dimensionless Reynolds number,  $\mathcal{R}$  based upon geometrical structure of the flow, characterises the condition of the fluid between laminar and turbulent:

$$\mathcal{R} = \frac{V_0 L_0}{\nu_0}, \quad (3.1)$$

where  $V_0$  is a characteristic velocity,  $L_0$  a characteristic size of the flow and  $\nu_0$  is the kinematic viscosity of the fluid. When the value of the Reynolds number exceeds a critical value, typically included between 1000 and 2000, the fluid becomes turbulent. In the atmosphere, typical values for air flow are;  $\nu_0 = 15 \times 10^{-6} \text{ m}^2\text{s}^{-1}$ ,  $V_0 = 1\text{ms}^{-1}$  and  $L_0 = 15\text{m}$ , which gives a Reynolds number  $\mathcal{R} = 10^6$ . It is much greater than the critical value, which corresponds to a fully developed turbulence, and the atmosphere is considered to be always turbulent.

The most common model to describe the atmosphere is the Kolmogorov model[50].

#### 3.1.3.1 Kolmogorov law

Kolmogorov assumed that the velocity fluctuations can be represented by a locally homogeneous and isotropic random field for scales less than the largest eddies or the energy source. In fully developed turbulence, the kinetic energy of large scale motions is transferred to smaller and smaller scale motions. Motions on a small scale are statistically isotropic. Motions at scale  $L$  have a characteristic velocity  $V$ . When the Reynolds number  $\mathcal{R}$  becomes small enough, the break up process stops and the kinetic energy is dissipated into heat by viscous friction. In a stationary state, the rate  $\varepsilon_0$  of viscous dissipation must be equal to the rate of production of



turbulent energy. A cascade of energy occurs from large scale size to smallest. The largest turbulent eddies have characteristic size  $L_0$  called the external or outer scale, while the dissipation into heat happens for a scale size  $l_0$  called the inner scale. The Kolmogorov law is valid within the inertial range included between  $l_0$  and  $L_0$ .

In the spectral domain the kinetic energy  $E(\kappa)$ , with  $\kappa = \sqrt{\kappa_x^2 + \kappa_y^2 + \kappa_z^2}$  the spatial wave number (modulus of vector spatial wave vector  $\boldsymbol{\kappa}$ ) can be expressed, by a dimensional reasoning, by

$$E(\kappa) \propto \kappa^{-\frac{5}{3}}. \quad (3.2)$$

Eq.(3.2) is valid in the inertial range  $\frac{2\pi}{L_0} \leq \kappa \leq \frac{2\pi}{l_0}$

$L_0$  is the outer scale (typically some tens of metres) and  $l_0$  the inner scale (a few millimetres), with  $\kappa = |\boldsymbol{\kappa}|$ . The 3D power spectrum is also described by

$$\Phi(\boldsymbol{\kappa}) \propto \kappa^{-\frac{11}{3}}, \quad (3.3)$$

where  $\kappa = \sqrt{\kappa_x^2 + \kappa_y^2 + \kappa_z^2}$

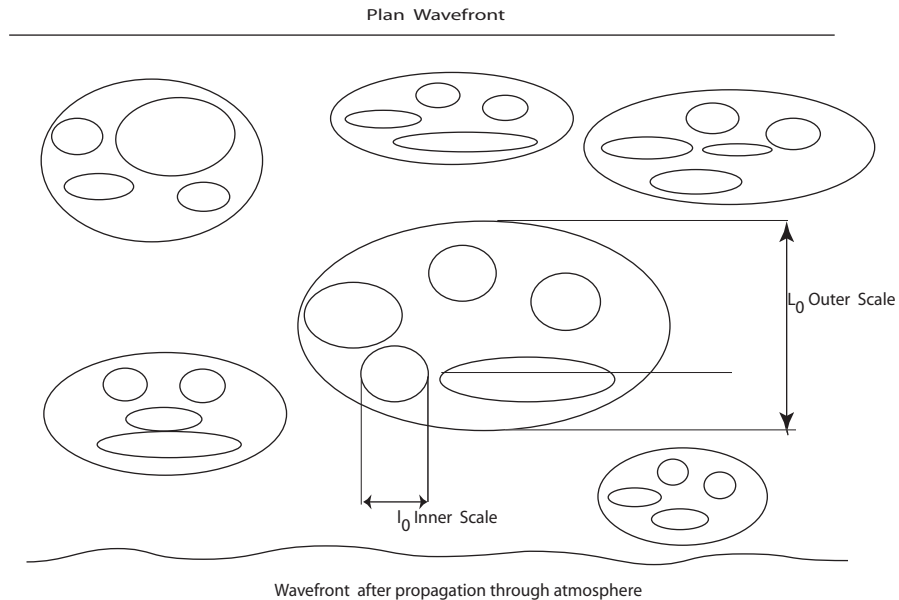


Fig. 3.3: Outer and inner scale.

Scalar quantities additive of the turbulent flow, passive (not affecting the dynamic of the medium) and conservative (not disappearing by chemical reaction),

like the temperature  $T$  and humidity  $C$  follow Kolmogorov law[56]. Let us call a scalar quantity following the Kolmogorov law as  $q_K = \langle q_K \rangle + \tilde{q}_K$ ; it follows that

$$\Phi_{q_K}(\boldsymbol{\kappa}) \propto \kappa^{-\frac{11}{3}}, \quad (3.4)$$

within the inertial range.

The refractive index  $n(\mathbf{r}, t)$  can be written as the sum of a mean  $\langle n \rangle$  and a randomly fluctuating term  $\tilde{n}(\mathbf{r}, t)$ .

$$n(\mathbf{r}, t) = \langle n \rangle + \tilde{n}(\mathbf{r}, t). \quad (3.5)$$

For air the mean refractive index is close to unity. Refractive index variations in the turbulent atmosphere arise mainly from temperature inhomogeneities. It is common to refer to the refractive index inhomogeneities as turbulent eddies which can be seen as pockets of air with a characteristic refractive index. At optical wavelengths, the dependence of the refractive index of air upon pressure and temperature, following the Gladstone law, is given by

$$\tilde{n} = -\frac{77.6P}{T^2} 10^{-6} \tilde{T}, \quad (3.6)$$

where  $T$  is the temperature and  $\tilde{T}$  the temperature fluctuation in Kelvin, and  $P$  is the pressure in millibar. From Eq.(3.6) the power spectrum of the refractive index fluctuations follow as well the Kolmogorov law, Eq.(3.3).

Expressing the covariance  $B_{q_K}(\Delta\mathbf{r})$  as defined in Eq.(2.71)

$$B_{q_K}(\Delta\mathbf{r}) = \langle [q_K(\mathbf{r}) - \langle q_K(\mathbf{r}) \rangle][q_K(\mathbf{r} + \Delta\mathbf{r}) - \langle q_K(\mathbf{r} + \Delta\mathbf{r}) \rangle] \rangle \quad (3.7)$$

The covariance of the fluctuating part  $\tilde{q}_K$  is related to the power spectrum of the same fluctuating part denoted  $\Phi_{q_K}$ , according to the Wiener-Khintchine theorem by

$$B_{q_K}(\Delta\mathbf{r}) = \int_{-\infty}^{\infty} \Phi_{q_K}(\boldsymbol{\kappa}) e^{i\boldsymbol{\kappa} \cdot \Delta\mathbf{r}} d\boldsymbol{\kappa}. \quad (3.8)$$

For a quantity following the Kolmogorov law, the power spectrum,  $\Phi_{q_K}(\boldsymbol{\kappa})$  Eq.(3.4) (being at the power minus eleven thirds) is not well behaved at the origin and the autocorrelation does not exist. Tatarskii[67] introduced a function  $D$ , the *structure function*, related to the covariance, describing the mean squared fluctuation between two points separated by  $\Delta\mathbf{r}$  :

$$D_{q_K}(\Delta\mathbf{r}) = \langle |q_K(\mathbf{r} + \Delta\mathbf{r}) - q_K(\mathbf{r})|^2 \rangle, \quad (3.9)$$

where  $\langle \rangle$  denotes the ensemble average.

The structure function is related to the covariance  $B_{q\kappa}$  (when the covariance exists), by

$$D_{q\kappa}(\Delta\mathbf{r}) = 2[B_{q\kappa}(0) - B_{q\kappa}(\Delta\mathbf{r})], \quad (3.10)$$

The structure function of the temperature[56] and then by extension, all the quantities following Kolmogorov law can be expressed as

$$D_{q\kappa}(\Delta\mathbf{r}) = C_{q\kappa}^2 (\Delta r)^{\frac{2}{3}}, \quad (3.11)$$

where  $C_{q\kappa}^2$  is the structure constant of the fluctuations.

The power spectrum of the refractive index fluctuations becomes [67]

$$\Phi_n(\boldsymbol{\kappa}) = 0.033 C_n^2 \kappa^{-\frac{11}{3}}, \quad (3.12)$$

where  $\kappa = \sqrt{\kappa_x^2 + \kappa_y^2 + \kappa_z^2}$ , and lies in the inertial range.

$C_n^2$  is the structure constant of the refractive index fluctuations, with units in  $\text{m}^{-\frac{2}{3}}$ . It characterises the optical energy of the turbulence and it measures the atmospheric turbulence contribution for a wave propagating through it. The typical values go from  $10^{-13}\text{m}^{-\frac{2}{3}}$  for strong turbulence to  $10^{-17}\text{m}^{-\frac{2}{3}}$  for weak turbulence. The structure constant of the refractive index fluctuations actually varies with altitude  $h$  of the turbulent layer,  $C_n^2(h)$ . Then the Kolmogorov spectrum is written

$$\Phi_n(\boldsymbol{\kappa}) = 0.033 C_n^2(h) \kappa^{-\frac{11}{3}}, \quad (3.13)$$

Note that just a single function  $C_n^2(h)$  *fully characterises* the spatial properties of atmospheric turbulence. There are other models to describe atmospheric turbulence, that can be extended outside the inertial range. The modified Von Kármán spectrum takes into account the outer and inner scale. Introducing  $\kappa_0 = \frac{2\pi}{L_0}$  and  $\kappa_m = \frac{5.92}{l_0}$ , the Von Kármán spectrum[23] is an empirical formula that rolls off the Kolmogorov spectrum at low and high frequencies, given by

$$\Phi_n^{VK}(\boldsymbol{\kappa}) = \frac{0.033 C_n^2(h)}{(\kappa^2 + \kappa_0^2)^{\frac{1}{6}}} e^{-\frac{\kappa^2}{\kappa_m^2}}, \quad (3.14)$$

The role of inner scale is to reduce the value of  $\Phi_n^{VK}(\boldsymbol{\kappa})$  compared to  $\Phi_n(\boldsymbol{\kappa})$  for wave numbers bigger than the upper limit  $\frac{2\pi}{l_0}$ . The outer-scale has an effect for lower wave numbers. For wavefront sensing the outer scale is usually of great importance.

$L_0$  can impact adaptive optics for the new generation of extremely large telescope designs[52, 20]. When considering scintillation, particularly strong scintillation, the inner scale becomes more significant[22].

The Kolmogorov model is the most common model used for scintillation. In this dissertation the Kolmogorov law will be used.

$C_n^2(h)$  varies with both height above the ground and local atmospheric conditions[35]. Given the refractive index fluctuation profile  $C_n^2(h)$  we can derived quantities of interest for astronomy related to the  $n$ -th order moments,  $M(n)$  defined as

$$M(n) = \int_0^\infty h^n C_n^2(h) dh, \quad (3.15)$$

where  $n$  may be fractional.

We can derive other quantities of interest for astronomical imaging from these moments, such as the turbulence coherence length defining long-time average image quality  $r_0$ , called the Fried parameter, related to  $M(0)$ , or the isoplanatic angle  $\vartheta_0$ , related to  $M(\frac{5}{3})$ , representing the angle within which we can consider that light propagates through the same optical path in turbulent layers:

$$r_0 = \left[ 0.423k^2 \sec Z \int_0^\infty dh C_n^2(h) \right]^{-\frac{3}{5}} \quad (3.16)$$

$$\vartheta_0 = \left[ 2.905k^2 (\sec Z)^{\frac{8}{3}} \int_0^\infty h^{\frac{5}{3}} dh C_n^2(h) \right]^{-\frac{3}{5}} \quad (3.17)$$

where  $k = \frac{2\pi}{\lambda}$  is the optical wavenumber and  $Z$  is zenith distance.

The long-exposure full width at half the maximum (FWHM) of the atmospheric optical transfer function, called seeing, is limited by the Fried parameter  $r_0$ . The seeing is given

$$\beta = 0.98 \frac{\lambda}{r_0} \quad (3.18)$$

Typical seeing values in good astronomical sites are around 0.8 arcsec, and “bad” seeing is above 1.5 arcsec.

### 3.1.3.2 Atmospheric temporal statistics

The temporal dependence of  $n(\mathbf{r}, t)$  over time has not been treated yet. In the case of atmospheric turbulence there are two time scales, one due to the motion of

atmosphere across the path of interest, and another one due to the dynamics of the turbulence itself (i.e. the dynamic turbulent eddies). The advection effect (transfer of heat by the horizontal movement of the air) can be estimated as  $\frac{L_0}{V_\perp}$ ,  $L_0$  is the outer scale and  $V_\perp$  is the mean transverse wind speed. Taking 10 m for the outer scale and  $10 \text{ ms}^{-1}$  for the wind speed, it gives a time scale of 1 s. Concerning the other temporal effect, it arises from wind fluctuations (turn over of the turbulent eddies). The time scale of this effect can be estimated to be 10% of the mean wind speed, that is to say 10 s time constant[11]. Thus, by neglecting the temporal dynamics of the eddies (taken as frozen in space) compared to the mean turbulent flow, the temporal properties can be introduced invoking the Taylor's hypothesis, or the frozen turbulence hypothesis[35]. Taylor's hypothesis assumes that over a short time interval a given realisation of the random structure,  $\tilde{n}$ , translates with constant transverse velocity, determined by the local wind conditions. Time differences are then equivalent to spatial shifts. The Taylor hypothesis means that for a single layer of turbulence, the refractive index fluctuations at a time  $t + \tau$  can be related to the refractive index fluctuations  $t$ , by

$$\tilde{n}(\mathbf{r}, t + \tau) = \tilde{n}(\mathbf{r} - \mathbf{V}_\perp(\tau), t), \quad (3.19)$$

where  $\mathbf{V}_\perp$  is the mean transverse velocity.

### 3.1.4 Propagation of light through atmospheric turbulence

As an optical field propagates through an atmospheric turbulence zone, the random variations of the index of refraction will cause perturbations of its phase crossing a turbulent zone. Free-space propagation will create both perturbations of the phase and of the amplitude. We consider monochromatic planes waves, of wavelength  $\lambda$ , propagating from a star at zenith towards a ground-based observer. Each point in the atmosphere will be represented by a vector horizontal coordinate  $\mathbf{r}$ , and an altitude  $h$  from the ground. The field at coordinates  $(\mathbf{r}, h)$  will be denoted by its complex amplitude

$$\Psi_h(\mathbf{r}) = |\Psi_h(\mathbf{r})|e^{i\phi_h(\mathbf{r})}, \quad (3.20)$$

where the phase  $\phi_h(\mathbf{r})$  is assumed to be a real Gaussian random process with zero-mean,  $\langle \phi_h(\mathbf{r}) \rangle = 0$ .

### 3.1.4.1 One thin layer

Consider one turbulent layer, that acts as random-phase screen, of thickness  $\delta h$  chosen to be large compared to the correlation scale of the inhomogeneities but small enough for diffraction effects to be negligible over the distance  $\delta h$  (*thin screen approximation*)[62].  $\Psi_{h+\delta h}(\mathbf{r}) = 1$  is the layer input and after crossing of the layer of thickness  $\delta h$ , the resulting complex field is

$$\Psi_h(\mathbf{r}) = e^{i\phi(\mathbf{r})}, \quad (3.21)$$

where the phase variation,  $\phi(\mathbf{r})$  caused by the random variations of the index of refraction  $n(\mathbf{r}, h)$  deduced from the optical geometry is

$$\phi(\mathbf{r}) = k \int_h^{h+\delta h} dz n(\mathbf{r}, z), \quad (3.22)$$

where  $k = \frac{2\pi}{\lambda}$  is the optical wave number

### 3.1.4.2 Free space propagation

Neglecting multiple scattering using the *Born approximation*, and since optical wavelengths are much smaller than the scale of the observed wavefront perturbation, the *Fresnel approximation* can be used[34] and the field on the ground due to the field at an altitude  $z$  is

$$\Psi_0(\mathbf{r}) = \Psi_z(\mathbf{r}) * p_z(\mathbf{r}) \quad (3.23)$$

The equation has the form of a convolution as in Eq.(2.35).  $p_z(\mathbf{r})$  is the point spread function of the Fresnel propagation, which is a shift-invariant operator, defined as

$$p_z(\mathbf{r}) = \frac{1}{i\lambda z} e^{\frac{i\pi r^2}{\lambda z}}, \quad (3.24)$$

with  $r = |\mathbf{r}|$ . The field at the distance  $z$  is found using the expression for the point spread function in Eq.(3.24)

$$\Psi_0(\mathbf{r}) = \Psi_z(\mathbf{r}) * \frac{1}{i\lambda z} e^{\frac{i\pi r^2}{\lambda z}} \quad (3.25)$$

Eq.(3.25) is the *Fresnel Diffraction* of the wave over a distance of propagation  $z$ .

### 3.1.4.3 Statistical properties of the field

The covariance of the phase fluctuations is defined as

$$B_\phi(\Delta\mathbf{r}) = \langle \phi(\mathbf{r})\phi(\mathbf{r} + \Delta\mathbf{r}) \rangle = k^2 \delta h \int_{-\infty}^{+\infty} B_n(\Delta\mathbf{r}, z) dz \quad (3.26)$$

Using local isotropy property, the fluctuation in the  $z = \text{constant}$  plane,  $W(\mathbf{f}, z)$  have spectrum given by  $W(\mathbf{f}, 0)$ [11]. The two-dimensional power spectrum of the phase fluctuations is then

$$W_\phi(\mathbf{f}) = k^2 \delta h W_n(\mathbf{f}, 0) \quad (3.27)$$

The two-dimensional power spectrum expressed with the spatial frequencies is related to the two-dimensional power spectrum expressed with the spatial wave number by

$$\Phi_n(f_x, f_y, f_z) = (2\pi)^3 \Phi_n(\kappa_x = 2\pi f_x, \kappa_y = 2\pi f_y, \kappa_z = 2\pi f_z) \quad (3.28)$$

where  $\mathbf{f} = (f_x, f_y, f_z)$  is a spatial vector frequency with dimension of an inverse length. Then the two dimensional power spectrum of the phase fluctuations Eq.(3.27) becomes

$$W_\phi(\mathbf{f}) = 9.7 \times 10^{-3} k^2 \mathbf{f}^{-\frac{11}{3}} C_n^2(h) \delta h \quad (3.29)$$

## 3.2 Stellar scintillation

An optical wave propagating through a random medium such as the atmosphere will experience irradiance fluctuations called scintillation. There are many articles describing the theory of scintillation[4, 27, 28, 29].

### 3.2.1 Phase and amplitude statistics

#### 3.2.1.1 Effect of a thin layer

To describe the optical path fluctuations, the small perturbation approximation is made (typically valid for vertical paths when the zenith angle does not exceed  $60^\circ$ ). The phase fluctuation caused by a “thin” layer is taken to be very small compared to unity, so that

$$\phi(\mathbf{r}) \ll 1 \quad (3.30)$$

With this assumption, the field at the layer output given by Eq.(3.21) can be written

$$\Psi_h(\mathbf{r}) \simeq 1 + i\phi(\mathbf{r}) \quad (3.31)$$

The complex field at the ground is a result of a free propagation, and is given using the Fresnel convolution Eq.(3.25)

$$\Psi_o(\mathbf{r}) = 1 + i\phi(\mathbf{r}) * \frac{1}{i\lambda h} e^{\frac{i\pi\mathbf{r}^2}{\lambda h}} \quad (3.32)$$

The Fourier transform of a constant is a delta function, and the Fourier transform of a convolution is a multiplication of the Fourier transforms. Defining the complex quantity  $\epsilon(\mathbf{r})$  as

$$\epsilon(\mathbf{r}) = \phi(\mathbf{r}) * \frac{1}{\lambda h} e^{\frac{i\pi\mathbf{r}^2}{\lambda h}} \quad (3.33)$$

The complex field at the ground,  $\Psi_o(\mathbf{r})$ , becomes

$$\Psi_o(\mathbf{r}) = 1 + \epsilon(\mathbf{r}) \quad (3.34)$$

$\epsilon$  defines the relative fluctuations of the complex amplitude at the ground due to the layer at altitude  $h$ . Its real part,  $\chi(\mathbf{r})$ , describes the relative fluctuations of the modulus  $|\Psi_o(\mathbf{r})|$  and its imaginary part,  $\phi_o(\mathbf{r})$ , describes the relative fluctuations of the phase  $\phi(\mathbf{r})$ ,

$$\chi(\mathbf{r}) = \phi(\mathbf{r}) * \frac{1}{\lambda h} \cos\left(\frac{\pi\mathbf{r}^2}{\lambda h}\right) \quad (3.35)$$

$$\phi_o(\mathbf{r}) = \phi(\mathbf{r}) * \frac{1}{\lambda h} \sin\left(\frac{\pi\mathbf{r}^2}{\lambda h}\right) \quad (3.36)$$

They both follow Gaussian statistics as the phase is Gaussian, and their power spectra are

$$W_\chi(\mathbf{f}) = W_\phi(\mathbf{f}) \sin^2(\pi\lambda h\mathbf{f}^2) \quad (3.37)$$

$$W_{\phi_o}(\mathbf{f}) = W_\phi(\mathbf{f}) \cos^2(\pi\lambda h\mathbf{f}^2) \quad (3.38)$$

Eq.(3.37) and Eq.(3.38) are obtained by taking the Fourier transform of  $\epsilon(\mathbf{r})$ . Using the convolution theorem (Eq.(2.21)) the Fourier transform is

$$\tilde{\epsilon}(\mathbf{f}) = \tilde{\phi}(\mathbf{f}) \cdot i \exp(-i\pi\lambda h\mathbf{f}^2), \quad (3.39)$$



where the last term is obtained by taking the Fourier transform of a Gaussian function (Eq.(2.18)) for  $\sigma^2 = -\frac{\lambda h}{2i\pi}$ . Then the Fourier transform of the log amplitude and of the phase are given by

$$\tilde{\chi}(\mathbf{f}) = \tilde{\phi}(\mathbf{f}) \sin(\pi\lambda h\mathbf{f}^2) \quad (3.40)$$

$$\tilde{\phi}_0(\mathbf{f}) = \tilde{\phi}(\mathbf{f}) \cos(\pi\lambda h\mathbf{f}^2) \quad (3.41)$$

Using the power spectrum of the phase defined in Eq.(3.29) the power spectrum of the fluctuation are given by

$$W_\chi(\mathbf{f}) = 9.7 \times 10^{-3} k^2 \mathbf{f}^{-\frac{11}{3}} C_n^2(h) \delta h \sin^2(\pi\lambda h\mathbf{f}^2) \quad (3.42)$$

$$W_{\phi_0}(\mathbf{f}) = 9.7 \times 10^{-3} k^2 \mathbf{f}^{-\frac{11}{3}} C_n^2(h) \delta h \cos^2(\pi\lambda h\mathbf{f}^2) \quad (3.43)$$

The power spectra contain, a term in  $\mathbf{f}^{-\frac{11}{3}}$  that come from the Kolmogorov power law of the turbulence, the structure constant of the refractive index fluctuations integrated on the layer  $C_n^2(h)\delta h$  and a third term corresponding to the filtering of Fresnel propagation.

### 3.2.1.2 Effect of multiple layers

When we consider multiple layers the fluctuations at ground level add linearly. Their power spectra add also because the fluctuations are assumed to be statistically independent[62]. The power spectra Eq.(3.42) and Eq.(3.43) become

$$W_\chi(\mathbf{f}) = 9.7 \times 10^{-3} k^2 \mathbf{f}^{-\frac{11}{3}} \int_0^\infty C_n^2(h) dh \sin^2(\pi\lambda h\mathbf{f}^2) \quad (3.44)$$

$$W_{\phi_0}(\mathbf{f}) = 9.7 \times 10^{-3} k^2 \mathbf{f}^{-\frac{11}{3}} \int_0^\infty C_n^2(h) dh \cos^2(\pi\lambda h\mathbf{f}^2) \quad (3.45)$$

## 3.2.2 Scintillation statistics

Scintillation corresponds to intensity fluctuations. If the power spectrum of the phase is taken as almost equal to the power spectrum of the relative fluctuations of the complex amplitude (neglecting the log-amplitude), it is the near-field approximation. The near-field approximation is used for angle-of-arrival fluctuations like adaptive optics system or the differential image motion monitor (DIMM[64]) instrument.

Writing the complex amplitude at the ground with  $\chi(\mathbf{r})$  and  $\phi_0(\mathbf{r})$  it becomes

$$\Psi_o(\mathbf{r}) = 1 + \chi(\mathbf{r}) + i\phi_0(\mathbf{r}) \quad (3.46)$$

The intensity is, neglecting the term of second order, given by

$$I(\mathbf{r}) = |\Psi_o(\mathbf{r})|^2 \simeq 1 + 2\chi(\mathbf{r}) \quad (3.47)$$

The quantity  $2\chi(\mathbf{r})$  describes the relative fluctuations of the intensity. The easiest quantity to measure is the “amount” of scintillation or the scintillation index  $\sigma_I^2$  defined as the variance of the relative irradiance (Intensity  $I$ ) fluctuations.

$$\sigma_I^2 = \frac{\langle\langle I \rangle - I \rangle^2}{\langle I \rangle^2} = \frac{\langle I^2 \rangle}{\langle I \rangle^2} - 1, \quad (3.48)$$

where the angular brackets denote an ensemble average or, equivalently, a long-time average.

Based on weak-fluctuation theory, Tatarskii[67] predicted that the correlation length of the light spots (flying shadows) is proportional to the first Fresnel zone scale  $\sqrt{h\lambda}$  (the small perturbation hypothesis). In second order statistics, we can derive the power spectrum of the relative irradiance fluctuations  $W_I(k)$  related to the power spectrum of the refractive index fluctuations  $\phi_n(k)$ . Following Eq.(3.47) the power spectrum of the relative irradiance fluctuations  $W_I(k)$  is related to the power spectrum of the relative amplitude fluctuations

$$W_I(\mathbf{f}) = 4W_\chi(\mathbf{f}) \quad (3.49)$$

The power spectrum of the relative irradiance fluctuations using is

$$W_I(\mathbf{f}) = 3.9 \times 10^{-2} k^2 \mathbf{f}^{-\frac{11}{3}} \int_0^\infty dh C_n^2(h) \sin^2(\pi\lambda h \mathbf{f}^2), \quad (3.50)$$

We can derive the scintillation index, which is the integral of Eq.(3.50), over frequency  $\mathbf{f}$

$$\sigma_I^2 = 19.2 \lambda^{-\frac{7}{6}} (\cos Z)^{-\frac{11}{6}} \int_0^\infty h^{\frac{5}{6}} C_n^2(h) dh \quad (3.51)$$

where  $Z$  is the zenith angle. For a given layer  $h$  the contribution to the scintillation index grows as the distance of the layer get larger as the power five-sixths,  $h^{\frac{5}{6}}$ .

### 3.2.3 Wavelength dependence

The amplitude of scintillation has a dependence on wavelength of  $\lambda^{-\frac{7}{6}}$ [25] ( $\sigma_I^2 \propto \lambda^{-\frac{7}{6}}$  Eq.(3.51)). The wavelength dependence is strong for small telescope aperture (at least smaller than 20 cm[28]) and big zenith angle[16] ( $Z > 60^\circ$ ). In broadband averaging, no significant bandwidth dependence is noted[28]

### 3.2.4 Aperture filtering

When a large telescope is used, the aperture function  $P(\mathbf{r})$  (which can be circular, annular, with spider or without) filters out some the high frequencies in the power spectrum[62, 25]. The aperture has a cut-off frequency inversely proportional to its diameter lowering the high frequency content of the power spectrum of irradiance  $W_I(\mathbf{k})$  and then the scintillation index is lowered. For the scintillation index it means a lower value due to the washing out of the small details (small shadows being washed out). The aperture filtering function is given by  $F_p(\mathbf{f}) = |\tilde{P}(\mathbf{f})|^2$  For the case of an annular aperture,  $F_p$  the aperture filter function[81] is given by

$$F_p(q, \mathbf{f}) = \left\{ \frac{2J_1(2\pi a \mathbf{f})}{2\pi a \mathbf{f}} - q^2 \left[ \frac{2J_1(2\pi b \mathbf{f})}{2\pi b \mathbf{f}} \right] \right\}^2 \quad (3.52)$$

The two-dimensional shadow-pattern  $W_I(\mathbf{f})$  becomes,

$$W_I^F(\mathbf{f}) = W_I(\mathbf{f}) \cdot F_p(\mathbf{f}), \quad (3.53)$$

where  $a$  is the aperture of the telescope,  $b$  the inner radius,  $f$  a spatial frequency,  $q$  the ratio between the inner radius and the outer one.

### 3.2.5 Neglecting scintillation effects in high angular resolution techniques

Adaptive optics techniques analyse the incoming distorted wavefront with a wavefront sensor. The Shack-Hartmann wavefront sensor divides the telescope aperture into many smaller subapertures, and a lenslet array is used to produce multiple spots onto a detector. The theoretical formula of the image centroid formed after a lens include the log-amplitude of the wave. In practice, the log-amplitude is neglected and the displacements of image centroids are supposed proportional to the

average wavefront slopes over the subapertures. For adaptive optics system under weak-turbulence conditions, taking into account the log-amplitude of the wave, and not only the phase of the wave, would give a more accurate measurement of the image centroid between 10% to 18%[76]. Scintillation affects also the quality of phase reconstruction from Hartmann data of tip-tilt and high-order aberrations[76].

### 3.3 SCIDAR

The concept of the SCIDAR (SCIntillation Detection And Ranging) technique was proposed by Vernin & Roddier in 1973[73], and followed by other approaches over a number of years: Rocca, Roddier & Vernin 1974[61], Vernin & Roddier 1975[74], Azouit & Vernin 1980[9], Caccia et al. 1987[15]. Fuchs, Tallon & Vernin (1994)[31] established the basis for the generalised SCIDAR, which was developed and tested by Avila, Vernin & Masciadri in 1997[6] and finally exploited by Avila, Vernin & Cuevas in 1998[5] and Klückers et al. 1998[49]. The first monitoring of the velocity profiles using a generalised SCIDAR was published in 2001 by Avila, Vernin & Sánchez[7].

SCIDAR has been very successfully exploited for several site characterization studies[49, 7, 63]. An automatically controlled SCIDAR instrument is installed at the Jacobus Kapteyn Telescope (JKT), at the observatory Roque de los Muchachos on La Palma island (Spain).[33]. The turbulence altitude and velocity profiles are recovered from an analysis of the autocorrelation of scintillation patterns for bright binary stars, recorded in the pupil plane of a large telescope. A binary star allows the separation of atmospheric turbulent layers by triangulation. For each layer at height  $h$ , there will be two correlated patterns of intensity fluctuations at the pupil plane separated by a distance  $d$ . According to triangulation  $d = \theta h$ , where  $\theta$  is the binary separation. The measurement quantity is the normalised scintillation spatial covariance function  $B(\mathbf{r})$ .

$$B(\mathbf{r}) = \frac{\langle [I(\mathbf{x}) - \langle I \rangle] [\langle I(\mathbf{x} + \mathbf{r}) - \langle I \rangle] \rangle}{\langle I \rangle^2} \quad (3.54)$$

where  $I(\mathbf{x})$  is the stellar intensity distribution in the pupil plane. Angular brackets denote ensemble average. Assuming that turbulence is isotropic, so  $C(\mathbf{r}) = B(r = |\mathbf{r}|)$  and  $\langle I \rangle$  is independent of time. The correlation of a single star is given using

the Wiener-Khintchine theorem Eq.(2.72) on the power spectrum of the intensity fluctuations at the ground. The power spectrum of the intensity is rotationally symmetric so the Fourier transform is a Hankel transform and the covariance is equal to

$$B(r) = 2\pi \int_0^{+\infty} f W_I(f) J_0(2\pi r f) df, \quad (3.55)$$

where  $f$  is the modulus of spatial frequency. Then we can rewrite the previous equation using Eq.(3.50).

$$B(r) = 3.9 \times 10^{-2} 2\pi k^2 \int_0^{+\infty} dh C_n^2(h) \int_0^{\infty} df f^{-\frac{8}{3}} \sin^2(\pi \lambda h f^2) J_0(2\pi r f) \quad (3.56)$$

Eq.(3.56) can be rewritten as to show the altitude dependence

$$B(r) = \int_0^{\infty} dh B_h(r, h), \quad (3.57)$$

$$B_h(r, h) = 3.9 \times 10^{-2} 2\pi k^2 C_n^2(h) \int_0^{\infty} df f^{-\frac{8}{3}} \sin^2(\pi \lambda h f^2) J_0(2\pi r f) \quad (3.58)$$

$B_h(r, h)$  represents the intensity fluctuation autocorrelation density per unit altitude produced by a layer located at an altitude  $h$ . The width of the autocorrelation peak is related to the height of the layer. The correlation length or average scale size of the scintillation is proportional to the width of the Fresnel zone  $\sqrt{\lambda h}$ .

The double star covariance can be derived from the single star covariance as[61]:

$$B_{**}(r, \theta) = \int_h dh \left\{ \frac{1 + \alpha^2}{(1 + \alpha)^2} B_h(r) + \frac{\alpha}{(1 + \alpha)^2} (B_h(r - \theta h) + B_h(r + \theta h)) \right\}, \quad (3.59)$$

where  $\alpha$  is relative magnitude of the binary star and  $\theta h$  separation of scintillation pattern. Short time exposures around a few milliseconds are used to freeze the turbulence. The  $C_n^2(h)$  profile is obtained by solving an inverse problem. If the plane of analysis of the scintillation is the same as that of the pupil plane of the telescope, the turbulent layer near the ground does not produce scintillation (scintillation develops after some significant propagation distance). The layer is “invisible”, so the idea is to defocus the image by using different set of lenses or by moving the observation plane to be able to resolve the scintillation effect due to the other layers, typically those near the ground. This is the concept of the *generalised* SCIDAR[31]. Fig. 3.4, shows the principle of double star SCIDAR

A fairly large telescope (diameter  $\geq 1$  m) and fast sensitive light detectors are needed to realise a profile monitor. Another disadvantage of classical or generalised

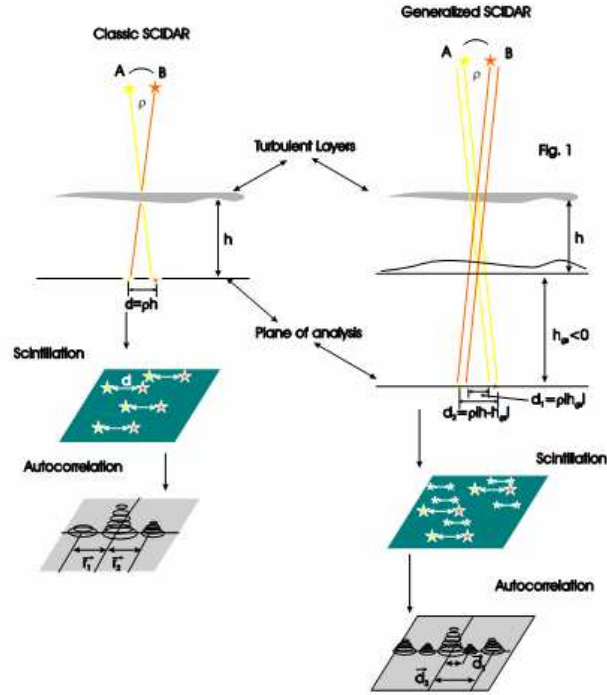


Fig. 3.4: Classic and Generalised Double Star SCIDAR (courtesy of Cruz et al.[24]).

SCIDAR is that a double star is used, meaning that one needs to find a bright enough binary with a good separation. This puts a significant limitation on sky coverage. The height resolution is typically about 200 – 500m[49].

### 3.4 Single star SCIDAR

An alternative, simple profile monitor (spatio-temporal correlation measurement of the profile) can in principle be constructed with a small telescope using a *single star* as a light source. A number of spatial filtering techniques applied to scintillation signal detection from single stars have also been proposed for this particular problem [57, 51]. The two-colour single star scintillation cross-correlation has also been used[16]. Recalling previous expressions Eq.(3.57) and Eq.(3.58), the autocorrelation for a single star is given by

$$B(r) = \int_0^{\infty} dh B_h(r, h), \quad (3.60)$$

We can re-write this to reveal the dependence upon the refractive index fluctuations

$$B(r) = \int_0^{\infty} dh C_n^2(h) K(r, h), \quad (3.61)$$

$$K(r, h) = 3.9 \times 10^{-2} 2\pi k^2 \int_0^{\infty} df f^{-\frac{8}{3}} \sin^2(\pi \lambda h f^2) J_0(2\pi r f) \quad (3.62)$$

where  $f$  is the modulus of spatial frequency. The autocorrelation contains the effect of all the layers encountered during the propagation process. Thus the autocorrelation is a superimposition of  $N$  peaks stacked, corresponding to  $N$  layers (see Fig. 3.5). For a visible wavelength of 550 nm, in the height range from 0 up to 25 km the atmospheric induced scintillation has a scale sizes ranging from 2 to 12 cm. In principle therefore a telescope with an aperture greater than this may be used to quantify  $B(r)$ .

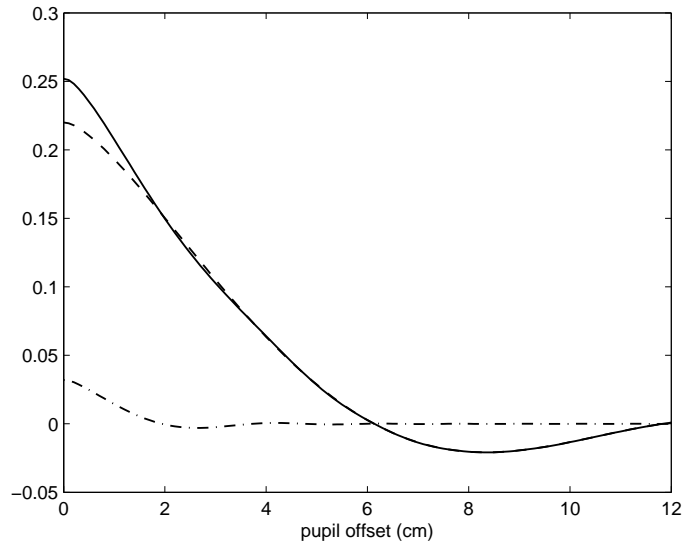


Fig. 3.5: Autocorrelation for different layers. Layer at 1 km (dashed-dotted), layer at 10 km (dashed), sum of layers at 1 and a 10 km (solid).

We can rewrite this equation in matrix form

$$B(r) = K(r, h)C_n^2(h) + n(r), \quad (3.63)$$

where  $K$  represents the kernel, which contains the theoretical autocovariance of a single star,  $B$  the autocovariance of the scintillation pattern and  $n(r)$  the noise.

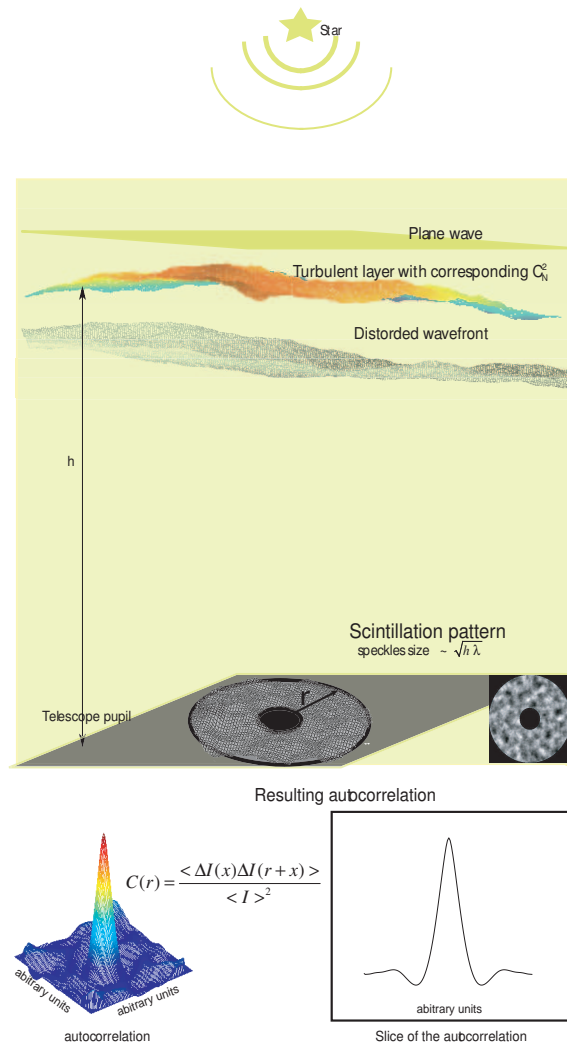


Fig. 3.6: Single star SCIDAR.

Eq.(3.63) is a Fredholm equation of the first kind [80, 12] . We need to invert it to obtain the refractive index profile  $C_n^2(h)$ . Unlike double star SCIDAR , the inverse problem single star SCIDAR is *difficult* because the covariance data consists only of a central peak. It is important that the central peak is sampled sufficiently to allow different measurements of it to be clearly distinguished.

### 3.4.1 Wind profile

The wind vector and its modulus can be found from a single star spatio-temporal cross-correlation analysis[15, 49]. If a layer at altitude  $h$  moves with a horizontal



wind velocity vector  $\mathbf{v}_h(\mathbf{r})$ , at ground level the flying shadow produced propagates with the same velocity. Using Taylor's hypothesis of frozen turbulence, after a time  $\tau$  the two elements are separated by  $\mathbf{v}_h(\mathbf{r})\tau$

$$B(r, \tau, h) = B(r - v\tau, h) = 3.9 \times 10^{-2} 2\pi k^2 \int_0^\infty df f^{-\frac{8}{3}} \sin^2(\pi \lambda h f^2) J_0(2\pi(r - v\tau)f) \quad (3.64)$$

From  $B(r, \tau, h)$  we can extract the velocity of each layer, their altitude and refractive index structure constant. The position of each peak gives the vector  $\mathbf{v}_h(\mathbf{r})$  of this layer. The shape of the peak gives the altitude  $h$  and the height of the peak gives the integrated value of  $C_n^2(h)\delta h$ . With the wind profile in addition of the  $C_n^2$  profile, one can derive other atmospheric parameters of interest such as the coherence time of the wavefront[58]

$$\tau_0 = \left[ 2.905 k^2 \int_0^\infty v^{\frac{5}{3}} dh C_n^2(h) \right]^{-\frac{3}{5}} \quad (3.65)$$

### 3.4.2 Multi-generalised single star SCIDAR

Based on the concept of a single star SCIDAR used in generalised mode we develop in this thesis the concept of a single star SCIDAR with different conjugation planes (see Fig. 3.8). The feasibility is based upon work of Johnston[44], Klückers[48] and Stevens[66]. With multiple measurement planes the problem to solve can be written as

$$B_{MP}(r) = K_{MP}(r, h)C_n^2(h) + n(r), \quad (3.66)$$

where  $B_{MP}$  denotes a matrix containing now P sets of single star covariance vectors measurements. The single star covariance matrices  $K_i$  for  $i = 1, 2, \dots, P$  contain theoretical covariances that are offset from the origin by the distance between the measurement layer and the telescope aperture.  $B_{MP}$  contains P one dimensional covariance slices, end to end, corresponding to the average covariances calculated from the scintillation measurements made at each plane. The conjugations below the telescope pupil allow retrieval of information about the boundary layer thanks to the extra propagation letting scintillation develop. The conjugations above permit better estimation of the layer located at this altitude; the effect of the layer at this altitude is not detected in the resulting autocorrelation thus this layer is one layer less to find in the overall other layers contributing. If the layer has a big

contribution, in particular the resolution of this layer is improved. If we call  $j$  the layer at height  $h_c$ , the autocorrelation conjugated at this plane is

$$B_{h_c}(r) = \sum_{i \neq j} B_i \quad (3.67)$$

### 3.4.3 Other Single star profilers

There are other single star turbulent profilers using a small telescope, and different techniques to extract atmospheric parameters.

#### 3.4.3.1 Spatio-temporal single star SCIDAR

This uses cross-correlation with 2 exposure times to separate contributions of different layers by their velocity difference. Wind dispersion in layers is included in the model. An instrument with a 25-cm telescope is under development[72, 37]. Results show good agreement with balloon sounding[36].

#### 3.4.3.2 MASS

MASS (Multi-Aperture Scintillation Sensor) is based on the analysis of the scintillation of bright stars. The spatial scale of the scintillation depends on the distance to the layer. This dependence is used to separate the contributions from different layers by means of zones of a small telescope pupil (8-14 cm), providing a profile of the optical turbulence strength with a low vertical resolution ( $dh/h \approx 0.5$ ), and no information about the ground layer. The turbulence profile is derived from the statistical processing of the series of photon counts[70]. A comparison between double star SCIDAR and MASS had been made in Mauna Kea[71]. DIMM (Differential Image Motion Monitor[64]) gives the overall atmospheric turbulence profile,  $r_o$  and is used by most observatories. A combination of MASS with DIMM, MASS-DIMM, which gives information about the ground layer has been tested[69].

### Profile restoration

The first analytical solution was given by Peskoff in 1968[59]. Later Jarem[43] used Tikhonov's regularisation technique in profile inversion. This method was tested on a simulated profile by Stevens[66]. However, this is a typical inverse problem:

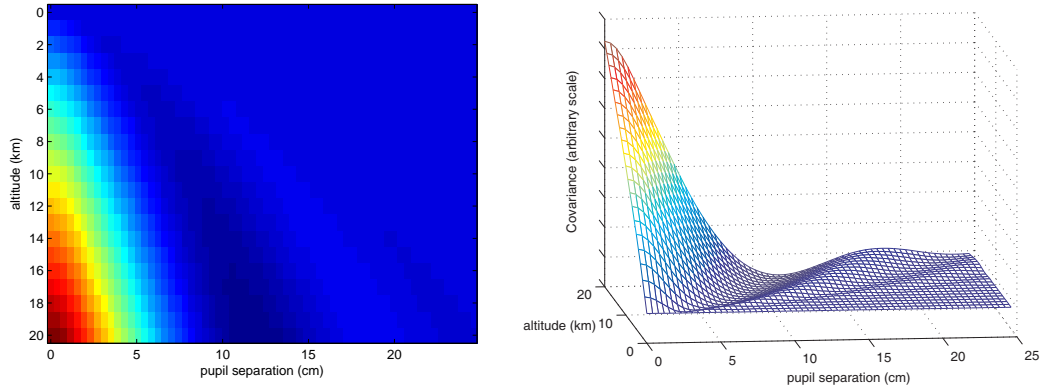


Fig. 3.7: Kernel of the single star SCIDAR.

the matrix  $K$  is ill-conditioned (the ratio of the largest eigenvalue to the smallest one is called the condition number of a matrix; large condition numbers mean ill-conditioned matrices). In such cases, direct inverse solution is so sensitive to the noise in the input data that it is useless in practice. The covariance matrix for the single star SCIDAR is highly singular [48], see Fig. 3.7.

An investigation of the sensitivity of the single star and crossed beam techniques to noise illustrates this and is achieved by decomposing the corresponding  $m \times n$   $K$  matrix, using the singular value decomposition (SVD)

$$K = U\Sigma V^\dagger, \quad (3.68)$$

where  $\Sigma$  is a diagonal matrix containing the singular values of  $K$  and  $V^\dagger$  is the transpose matrix of  $V$ . Matrices  $U$  and  $V$  contain respectively the left and right singular vectors of  $K$ [60]. The scintillation from a single star at a number of different planes, obtained by propagating the wavefront over different distances, is used to improve the conditioning of the inverse problem. The blurring process due to propagation in the atmosphere causes information to be lost. In this case it is necessary to incorporate additional information to enable the components of the problem to be estimated. In astronomical, or incoherent, imaging it is common to enforce positivity in an attempt to achieve the closest possible match to the actual object. This comes from the fact that we are measuring intensities that are positive. Thus the components of the problem are positive. It is also necessary to regularise the deconvolution problem to enable its inversion in the presence of noise. Due to the ill-posed nature of the deconvolution problem, the quality of the reconstruction

depends on the assumed noise statistics and the available object prior information.

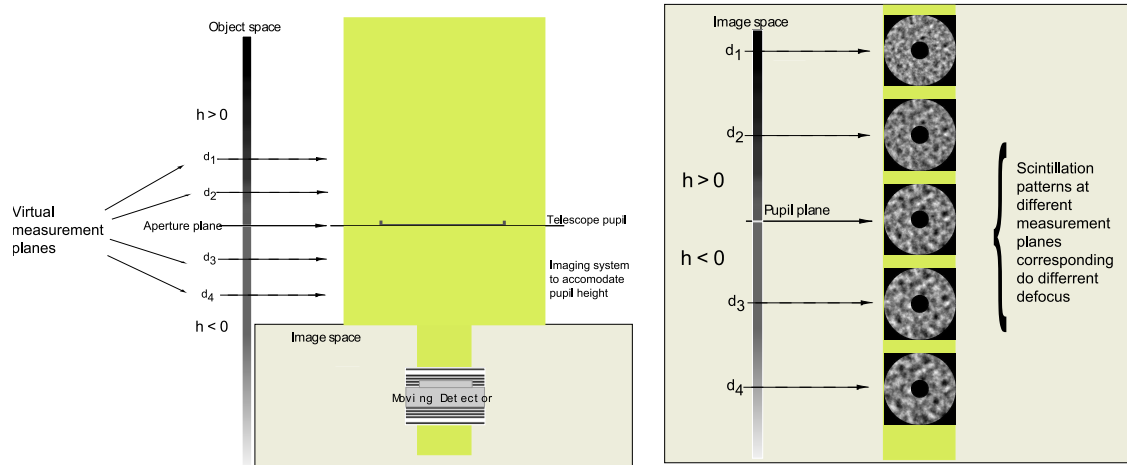


Fig. 3.8: Sequenced generalised single star SCIDAR.

### 3.4.4 Other atmospheric profilers

#### 3.4.4.1 In situ $C_n^2(h)$

The measure of the refractive index fluctuation can be achieved by launching meteorological balloons equipped with temperature sensors[8] that can characterise the structure constant of the temperature fluctuations  $C_T^2(h)$  linked to the structure constant  $C_n^2(h)$  by the Gladstone formula Eq.(3.6). The resolution is good (5-10 m) but the obtaining of the profile takes a long time (several hours).

#### 3.4.4.2 SLODAR

SLODAR (SLOpe Detection And Ranging) is based on an analogous binary star triangulation method as the double star SCIDAR. It is an extension based on angle of arrival theory. The turbulence altitude profile is recovered from the time-averaged spatio-angular cross-correlation of the instantaneous wavefront slopes, measured in the telescope pupil plane by using a Shack-Hartmann wavefront sensor to observe a bright binary star[77]. Wind velocity is measurable as well. The resolution in altitude varies between 150 and 1500 m, depending on the double star separation (like in double star SCIDAR). SLODAR is able to characterise very well turbulence

---

at lower altitudes ( $< 2$  km). Additionally, a larger magnitude differential can be tolerated compared to double star SCIDAR technique[78]. A portable version is in development with a 40 cm telescope[79].

#### **3.4.4.3 3D mapping of atmospheric turbulence**

There are efforts to obtain a 3D mapping of optical turbulence using atmospheric numerical models. Those techniques use meteorological parameters such as temperature, wind speed and topography of the site. The refractive index fluctuation profile and other atmospheric parameters can be obtained[54, 55].

---

# Chapter 4

## Inverse problems

---

An inverse problem occurs when the causes have to be found indirectly from the effects. The estimation of the  $C_n^2(h)$  profile from a set of generalised single star SCIDAR correlation functions is a typical inverse problem. The problem can be formulated as  $\mathbf{g} = \mathcal{S}\mathbf{f}$ , where  $\mathbf{f}$  represent the causes and the operator of the system  $\mathcal{S}$  is the linear operator integral, convolution or a matrix. The operator  $\mathcal{S}$ , the measurement, is that of the *forward problem*. The *inverse problem* is estimating  $\mathbf{f}$  given the data  $\mathbf{g}$ ; in practice, measurement noise plays a crucial role. An example of an inverse problem in astronomy is the deconvolution of images knowing the point spread function of the system, to find the object. Finding the object is not straightforward because different objects can give the same measurement image. Most inverse problems cannot be solved analytically, and computational methods are essential. Discretisation can lead to ill-posedness in matrix equation inversion. We talk then of an *ill-posed problem*. In that case, there may be ways to “cure”, or *regularise* by different techniques.

### 4.1 Mathematical basis

This section will treat the operator properties that are needed to understand inverse problems.

### 4.1.1 Linearity and boundedness

An operator is denoted  $\mathcal{H} : \mathbb{U} \longrightarrow \mathbb{V}$ , where  $\mathbb{U}$  and  $\mathbb{V}$  are both Hilbert spaces<sup>1</sup>. An operator  $\mathcal{H}$  acts on functions  $\mathbf{f}$  in space  $\mathbb{U}$  and transforms  $\mathbf{f}$  to function  $\mathbf{g}$  in space  $\mathbb{V}$ .

$$\mathbf{g} = \mathcal{H}\mathbf{f} \quad (4.1)$$

The operator  $\mathcal{H}$  is linear if

$$\mathcal{H}(\mathbf{f}_1 + c\mathbf{f}_2) = \mathcal{H}\mathbf{f}_1 + c\mathcal{H}\mathbf{f}_2 \quad (4.2)$$

for all scalars and all vectors in  $\mathbb{U}$ . A linear operator  $\mathcal{H}$  is bounded if there a positive number  $M$  such that for all  $\mathbf{f}$

$$\|\mathbf{g}\| = \|\mathcal{H}\mathbf{f}\| \leq M \|\mathbf{f}\| \quad (4.3)$$

A bounded operator cannot produce an image of infinite norm when operating on a vector of finite norm. The smallest  $M$  verifying the inequality is called the norm of  $\mathcal{H}$ , and we write  $M = \|\mathcal{H}\|$ .

### 4.1.2 Range and domain

Consider a linear operator  $\mathcal{H} : \mathbb{U} \longrightarrow \mathbb{V}$ , where the two spaces are Hilbertian as above. The set of vectors  $\mathbf{f}$  of  $\mathbb{U}$  is called the *domain* of  $\mathcal{H}$ . The vector  $\mathbf{g}$  is the *image*, denoted  $\mathcal{D}(\mathcal{H})$ , of the vector  $\mathbf{f}$ . The output set has to be distinguished between the actual values and the possible values. The possible values represent the space  $\mathbb{V}$ , while the actual values of images  $\mathbf{g}$ , called range of  $\mathcal{H}$ , denoted  $\mathcal{R}(\mathcal{H})$ , can be a subspace of  $\mathbb{V}$ .

### 4.1.3 Continuity and compactness

The operator  $\mathcal{H}$  is continuous if and only if

$$\text{if a sequence } \mathbf{f}_j \in \mathbb{U}, \text{ when } \lim_{j \rightarrow \infty}, \text{ then } \lim_{j \rightarrow \infty} \mathcal{H}\mathbf{f}_j = \mathcal{H}\mathbf{f}. \quad (4.4)$$

Bounded linear operators are continuous and vice versa. A compact operator[10] is one that maps a bounded sequence into one having a convergent subsequence.

<sup>1</sup> appendix A gives more details about Hilbert spaces

A sequence  $\mathbf{f}_j$  in  $\mathbb{U}$  is bounded ( $\|\mathbf{f}_j\| \leq C$ ), then the sequence  $\mathcal{H}\mathbf{f}_j$  contains a convergent subsequence if the operator  $\mathcal{H}$  is compact. Any linear operator with a finite-dimensional range is compact. In particular, matrix operators are compact.

#### 4.1.4 Matrix operators

Considering an  $M \times N$  real matrix  $\mathbf{H}$ , that can be viewed as a compact linear operator, mapping  $\mathbb{R}^N$  to  $\mathbb{R}^M$ , we have in a matrix form

$$\mathbf{g} = \mathbf{H}\mathbf{f} \quad (4.5)$$

or more explicitly

$$g_m = \sum_{n=1}^N H_{mn} f_n \quad (4.6)$$

The number of linearly independent rows or columns of  $H$  is called the rank, denoted rank  $H$ ,  $R(\mathbf{H})$ , or simply  $R$ . The rank is always less than or equal to the smaller of the number of rows  $M$  or columns  $N$ .  $R \leq \min(M, N)$ .

#### 4.1.5 Adjoint operator

The adjoint operator of a bounded operator  $\mathcal{H}$ , noted  $\mathcal{H}^\dagger$  mapping from  $\mathbb{V}$  to  $\mathbb{U}$  is the unique operator such that

$$(\mathbf{g}_2, \mathcal{H}\mathbf{f}_1)_{\mathbb{V}} = (\mathcal{H}^\dagger \mathbf{g}_2, \mathbf{f}_1)_{\mathbb{U}} \quad (4.7)$$

It can be shown that the norm of the adjoint operator  $\mathcal{H}^\dagger$  of a bounded operator  $\mathcal{H}$  is the same as that of  $\mathcal{H}$ ;  $\|\mathcal{H}^\dagger\| = \|\mathcal{H}\|$ . If  $\mathcal{H}^\dagger = \mathcal{H}$  for bounded operator  $\mathcal{H}$ , possible for  $\mathbb{U} = \mathbb{V}$ , the operator is said to be self-adjoint or *Hermitian*. If  $\mathcal{H}^\dagger = \mathcal{H}^{-1}$ , again possible for  $\mathbb{U} = \mathbb{V}$ , the operator is said to be *unitary*.

#### 4.1.6 Null space of an operator

The null space of a linear operator  $\mathcal{H}$ , noted  $\mathcal{N}(\mathcal{H})$  is the set of vectors  $\mathbf{f}$  in  $\mathbb{U}$  that satisfy  $\mathcal{H}\mathbf{f} = 0$

$$\mathcal{N}(\mathcal{H}) = \{\mathbf{f} \in \mathbb{U}; \mathcal{H}\mathbf{f} = 0\}. \quad (4.8)$$

The *null* space is a linear subspace and also is closed if the operator  $\mathcal{H}$  is continuous. If the operator is a convolution operator representing an imaging system, the null



space is also called the subspace of the *invisible objects*, because any objects  $\mathbf{f}$  give an image which is zero. The vectors  $\mathbf{f}$  can be uniquely decomposed as  $\mathbf{f} = \mathbf{f}_{meas} + \mathbf{f}_{null}$ .

### 4.1.7 Inverse operator

The inverse operator of a bounded operator  $\mathcal{H}$ , noted  $\mathcal{H}^{-1}$  mapping from  $\mathbb{V}$  to  $\mathbb{U}$  is the operator such that

$$\mathcal{H}\mathcal{H}^{-1} = \mathcal{I}_{\mathbb{V}} \quad (4.9)$$

$$\mathcal{H}^{-1}\mathcal{H} = \mathcal{I}_{\mathbb{U}} \quad (4.10)$$

The inverse operator,  $\mathcal{H}^{-1}$  does not necessarily exist, while the adjoint operator  $\mathcal{H}^\dagger$  does. If the operator  $\mathcal{H}$  is invertible ( $\mathcal{H}^{-1}$  exists) the operator is said *non-singular*, and it has no null space. If the operator is not invertible it is said to be singular.

### 4.1.8 Singular value decomposition

The singular value decomposition of an operator is a very important tool.

#### 4.1.8.1 Eigenanalysis

We recall briefly the notions of eigenvalues and eigenvectors. For a linear operator  $\mathcal{H}$ ,  $\mathbb{U} \rightarrow \mathbb{U}$ , the eigenvectors and eigenvalues satisfy the eigenvalue equation

$$\mathcal{H}\psi = \lambda\psi \quad (4.11)$$

The eigenvectors are  $\psi$  and the eigenvalues are  $\lambda$ .

#### 4.1.8.2 Singular value decomposition of a matrix

When a  $M \times N$  matrix  $\mathbf{H}$  is singular we can decompose the matrix using a singular value decomposition (SVD)[10, 12]. We assume  $\mathbf{H}$  is a matrix with rank  $R$ , mapping  $\mathbb{E}^N$  to  $\mathbb{E}^M$ .  $\mathbf{H}$  can be written as

$$\mathbf{H} = \mathbf{U}\mathbf{\Sigma}\mathbf{V}^\dagger \quad (4.12)$$

where  $\mathbf{U} = [\mathbf{u}_1, \dots, \mathbf{u}_M]$  is  $M \times M$  orthonormal matrix,  $\mathbf{V}$  is  $N \times N$  orthonormal matrix, and  $\mathbf{\Sigma}$  is  $M \times N$  a rectangular diagonal matrix with entries  $s_j \{j = 1, \dots, R\}$

and 0 elsewhere. Conventionally we order the singular values  $s_j$  by decreasing order,

$$s_1 \geq s_2 \geq \dots \geq s_R \geq 0, \quad (4.13)$$

Note that in Eq.(4.12) it is the adjoint of  $\mathbf{V}$ . Matrices  $\mathbf{U}$  and  $\mathbf{V}$  are unitary, i.e  $\mathbf{U}^\dagger \mathbf{U} = \mathbf{I}_U$  and  $\mathbf{V}^\dagger \mathbf{V} = \mathbf{I}_V$ . They are orthogonal as well, meaning that  $\langle \mathbf{u}_i, \mathbf{u}_j \rangle = \delta_{ij}$  and  $\langle \mathbf{v}_i, \mathbf{v}_j \rangle = \delta_{ij}$ .  $\mathbf{U} = \mathbf{u}_i, i = 1, \dots, R$  are the singular vectors. The ratio  $C = s_1/s_R$  of the largest to smallest singular value, is called the *condition number* of a matrix. A matrix with a large condition number is called *ill-conditioned* and can lead to big round-off errors. Relative errors in the data,  $\delta \mathbf{g}$  and in the solution  $\delta \mathbf{f}$  are related to the condition number

$$\frac{\|\delta \mathbf{f}\|}{\|\mathbf{f}\|} \leq C \frac{\|\delta \mathbf{g}\|}{\|\mathbf{g}\|}$$

#### 4.1.8.3 Hermitian operators

For any linear operator  $\mathcal{H}, \mathbb{U} \longrightarrow \mathbb{V}$ , we can construct two Hermitian (self-adjoints) operators,

$$\overline{\mathcal{H}} = \mathcal{H}^\dagger \mathcal{H}, \quad \tilde{\mathcal{H}} = \mathcal{H} \mathcal{H}^\dagger \quad (4.14)$$

The first operator maps  $\mathbb{U} \longrightarrow \mathbb{U}$ , and the second maps  $\mathbb{V} \longrightarrow \mathbb{V}$ . It is easy to show that  $\tilde{\mathcal{H}}$  satisfies also the property of an adjoint operator. Another property is that they are nonnegative-definite (or positive semi-definite) and compact. Nonnegative-definite means that the eigenvalues are real and nonnegative, or equivalently  $(\overline{\mathcal{H}}\mathbf{u}, \mathbf{u})_{\mathbb{U}} \geq 0$ . Using the properties of adjoint operators and using the norm definition for a vector  $\mathbf{u}$  we can write  $(\overline{\mathcal{H}}\mathbf{u}, \mathbf{u})_{\mathbb{U}} = (\mathcal{H}^\dagger \mathcal{H}\mathbf{u}, \mathbf{u})_{\mathbb{U}} = (\mathcal{H}\mathbf{u}, \mathcal{H}\mathbf{u})_{\mathbb{V}} = \|\mathcal{H}\mathbf{u}\|_{\mathbb{V}}^2 \geq 0$ . We can show the same properties for the other Hermitian operator  $\tilde{\mathcal{H}}$ . If we use the results for the SVD of a matrix, for the operator  $\mathcal{H}$  this time, writing the eigenvectors  $\mathbf{u}$  and eigenvalues  $\mathcal{H}\mathbf{u} = \lambda\mathbf{u}$ , it becomes  $\|\mathcal{H}\mathbf{u}\|_{\mathbb{V}}^2 = \lambda^2 \|\mathbf{u}\|_{\mathbb{U}}^2 \geq 0$ . Eigenvalues for  $\tilde{\mathcal{H}}$  are in fact the same[12]: the two operators  $\overline{\mathcal{H}}$  and  $\tilde{\mathcal{H}}$  have the same eigenvalues.

$$\overline{\mathcal{H}}\mathbf{u}_n = \mathcal{H}^\dagger \mathcal{H}\mathbf{u}_n = s_n^2 \mathbf{u}_n \quad (4.15)$$

$$\tilde{\mathcal{H}}\mathbf{v}_n = \mathcal{H} \mathcal{H}^\dagger \mathbf{v}_n = s_n^2 \mathbf{v}_n \quad (4.16)$$

#### 4.1.8.4 Pseudo-inverse of a matrix

The pseudo-inverse, or Moore-Penrose inverse, of a linear operator  $\mathcal{H}$ , represented by a matrix  $\mathbf{H}$ , noted  $\mathbf{H}^+$  is a generalisation of the inverse. The Moore-Penrose pseudo-inverse exists and is unique for all matrices, all operators with a finite-dimensional range and many integral operators. For an  $M \times N$  matrix, the pseudo-inverse is a matrix  $N \times M$  that satisfies

$$\mathbf{H}\mathbf{H}^+\mathbf{H} = \mathbf{H} \quad (4.17)$$

$$\mathbf{H}^+\mathbf{H}\mathbf{H}^+ = \mathbf{H}^+ \quad (4.18)$$

$$(\mathbf{H}\mathbf{H}^+)^\dagger = \mathbf{H}\mathbf{H}^+ \quad (4.19)$$

$$(\mathbf{H}^+\mathbf{H})^\dagger = \mathbf{H}^+\mathbf{H}. \quad (4.20)$$

If the inverse of  $(\mathbf{H}^\dagger\mathbf{H})$  exists, then the pseudo-inverse is defined as

$$\mathbf{H}^+ = (\mathbf{H}^\dagger\mathbf{H})^{-1}\mathbf{H}^\dagger \quad (4.21)$$

#### 4.1.8.5 Pseudo-inverse and SVD

If  $R = N$ , then all the singular values are non-negative but non-null and the pseudo-inverse is, with the SVD decomposition,

$$\mathbf{H}^+ = \mathbf{V}(\boldsymbol{\Sigma}^\dagger\boldsymbol{\Sigma})^{-1}\boldsymbol{\Sigma}^\dagger\mathbf{U}^\dagger \quad (4.22)$$

If  $R < N$ , we have  $R$  non-null singular values and  $N - R$  null values. The matrix  $(\boldsymbol{\Sigma}^\dagger\boldsymbol{\Sigma})^{-1}$  does not exist, but we can keep the non-null singular values,  $s_1 > s_2 \dots > s_R > 0$ , and define the  $R \times R$  matrix  $\boldsymbol{\Sigma}_R = \text{diag}(s_1, \dots, s_R)$ , and “shrink”  $\mathbf{U}_R$  and  $\mathbf{V}_R$  to  $R \times R$  matrices, smaller versions of  $\mathbf{U}$  and  $\mathbf{V}$ .

We can define a general pseudo-inverse for any rank  $R$ , as

$$\mathbf{H}^+ = \mathbf{V}\boldsymbol{\Sigma}^+\mathbf{U}^\dagger \quad (4.23)$$

where

$$\Sigma_{ij}^+ = s_i^+ \begin{cases} \frac{1}{s_j} & \text{for } i = j \text{ and } j \leq R \\ 0 & \text{otherwise} \end{cases} \quad (4.24)$$

## 4.2 Well-posed and ill-posed problems

The definition of a well-posed (correctly set) problem is due to Hadamard[38]. Given the mapping  $\mathcal{H} : \mathbb{U} \longrightarrow \mathbb{V}$ , equation

$$\mathbf{g} = \mathcal{H}\mathbf{f} \quad (4.25)$$

is well-posed if the solution  $\mathbf{f}$

- (a) exists for any data. For each  $\mathbf{g} \in \mathbb{V}$ , there exists a  $\mathbf{f} \in \mathbb{U}$  such that  $\mathbf{g} = \mathcal{H}\mathbf{f}$ . (*Existence*)
- (b) is unique  $\mathcal{H}\mathbf{f}_1 = \mathcal{H}\mathbf{f}_2$  only if  $\mathbf{f}_1 = \mathbf{f}_2$  (*Uniqueness*)
- (c) depends continuously on data.  $\forall$  sequence  $\mathbf{f}_j \in \mathbb{U}$ , when  $\lim_{j \rightarrow \infty} \mathcal{H}\mathbf{f}_j = \mathcal{H}\mathbf{f}$ , then  $\lim_{j \rightarrow \infty} \mathbf{f}_j = \mathbf{f}$ .  $\mathcal{H}^{-1}$  is continuous. (*Stability*)

The first requirement means that for each set of data there exists an object called the solution. The second means that the solution found is unique. The third requirement means that infinitesimal changes in the initial data result in infinitesimal changes in the solution, or that  $\mathcal{H}$  is continuous. An equation is ill-posed if it is not well-posed. To find a solution if the problem is ill-posed, it might be necessary to enlarge the solution space to respect existence, and introduce constraints for uniqueness. In imaging, the operator can be an integral operator or a convolution common in astronomy.

### 4.2.1 Linear integral equation

The general form of a linear integral equation is

$$g(x') = \int_{\alpha}^{\beta} h(x', x) f(x) dx, \quad (4.26)$$

where  $h(x', x)$  is called the kernel of the transform. Eq.(4.26) is a linear Fredholm integral equation of the *first* kind[80]. The Fredholm first kind integral operator is a compact operator on  $\mathbb{L}_2$ . Convolution and the Fourier transform are integral transforms.

### 4.2.2 Functional

A functional, that will be denoted  $\mathcal{J}$ , is a mapping which associates a number (real or complex) to each vector, or function. The functional is an important concept in the inverse problem field.

### 4.2.3 Resolution

The direct solution can be given using singular values decomposition by  $\mathbf{f} = \mathbf{H}^+ \mathbf{g}$ . The pseudo-inverse is obtained by singular value decomposition (Eq.(4.23)).

$$\mathbf{f}_d = \mathbf{V} \boldsymbol{\Sigma}^+ \mathbf{U}^\dagger \mathbf{g} \quad (4.27)$$

$$= \sum_{s_i \geq 0} s_i^+ (\mathbf{u}_i^\dagger \mathbf{g}_i) \mathbf{v}_i \quad (4.28)$$

Instability arises due to division by small singular values. A filter can be applied to the small singular values keeping only the singular values bigger than a certain value for instance.

A key component of the functional is some measure of the distance in data space between  $\mathbf{g}$  and  $\mathbf{Hf}$ , so we are led to define the discrepancy functional or data-agreement functional  $\mathcal{J}_{data}(\mathbf{Hf}, \mathbf{g})$ . In least-square data methods, this functional is just the squared Hilbert space norm.

$$\mathcal{J}_{data}(\mathbf{Hf}, \mathbf{g}) = \|\mathbf{g} - \mathbf{Hf}\|^2 \quad (4.29)$$

In all cases the noise is another parameter to take into account. The equation Eq.(4.25) becomes

$$\mathbf{g} = \mathcal{H}\mathbf{f} + \mathbf{n} \quad (4.30)$$

where  $\mathbf{n}$  represents the noise. The noise is a very important parameter and can change the way of dealing with the problem.

In the presence of (random) noise, a statistical approach is used.

## 4.3 Regularisation methods

A reasonable way to compute a meaningful “smooth” solution, i.e. a solution which has some useful properties in common with the exact solution to the underlying

and unknown-unperturbed problem, is to filter out the high-frequency components associated with the small singular values. Regularisation suppresses the recovery of singular vectors that correspond to small singular values, which are the components that transmit the fine details. Regularisation methods are techniques to get closer to the the accurate solution in the absence of noise. The idea of regularisation is to consider a set of approximate solutions depending on a positive parameter called the regularisation parameter. Regularisation makes a compromise between ill-posedness and accuracy. The next section treats the Tikhonov regularisation method.

### 4.3.1 Tikhonov regularisation

The regularisation functional is

$$\mathcal{J}_{reg}(\mathbf{f}) = \|\mathbf{f}\|^2 \quad (4.31)$$

$$\mathcal{J}(\mathbf{H}\mathbf{f}, \mathbf{g}) = \|\mathbf{g} - \mathbf{H}\mathbf{f}\|^2 + \gamma \|\mathbf{f}\|^2 \quad (4.32)$$

The regularisation parameter  $\gamma$  quantifies the trade-off between data fidelity and stability. The parameter acts as a filter on the singular values[12].

### 4.3.2 Regularisation parameter selection

The choice of the regularisation parameter is important and difficult. In this section we consider the case of Tikhonov regularisation. Different analytical approaches exist to find the value of the regularisation parameter[75, 12]. They fold in two categories either some statistics parameter (such as variance) about the noise is known or do not. A brief overview will be presented here. First we define some quantities that will be used in these theories.

The predictive error is defined as

$$\mathbf{p}_\gamma = \mathbf{H}(\mathbf{f}_\gamma - \mathbf{f}) = \mathbf{H}\mathbf{f}_\gamma - \mathbf{H}\mathbf{f} \quad (4.33)$$

The regularised solution can be expressed as

$$\mathbf{f}_\gamma = \mathbf{R}_\gamma \mathbf{g} = \mathbf{R}_\gamma (\mathbf{H}\mathbf{f} + \mathbf{n}) \quad (4.34)$$

where  $\mathbf{R}_\gamma$  is the regularisation matrix

The regularised residual is defined as

$$\mathbf{r}_\gamma = \mathbf{H}\mathbf{f}_\gamma - \mathbf{g} \quad (4.35)$$

We define the symmetric influence matrix to be

$$\mathbf{A}_\gamma = \mathbf{H}\mathbf{R}_\gamma \quad (4.36)$$

Then using this influence matrix the predictive error and regularised residual become

$$\mathbf{p}_\gamma = (\mathbf{A}_\gamma - \mathbf{I})\mathbf{H}\mathbf{f} + \mathbf{A}_\gamma\mathbf{n} \quad (4.37)$$

$$\mathbf{r}_\gamma = \mathbf{H}\mathbf{f}_\gamma - \mathbf{g} = (\mathbf{A}_\gamma - \mathbf{I})\mathbf{g} \quad (4.38)$$

#### 4.3.2.1 Generalised Cross-validation

The Generalised Cross-validation[12] (GCV) is based on the norm of the regularised residual  $\|\mathbf{r}_\gamma\|^2$ . The method consists of finding the regularisation parameter  $\gamma$  that minimises the GCV functional

$$\text{GCV}(\gamma) = \frac{\frac{1}{n} \|\mathbf{r}_\gamma\|^2}{\left[\frac{1}{n} \text{Tr}(\mathbf{I} - \mathbf{A}_\gamma)\right]^2} \quad (4.39)$$

where  $\text{Tr}$  denotes the trace operator. The trace of a matrix  $N \times N$   $\mathbf{A}$  is the sum of the main diagonal elements:

$$\text{Tr}(\mathbf{A}) = \sum_{i=1}^N A_{i,i}$$

#### 4.3.2.2 L-curve

The regularised residual norm  $\|\mathbf{r}_\gamma\|^2$ , as well as the norm of the extra information which is the solution itself  $\|\mathbf{f}_\gamma\|^2$  have to be minimised. It is based on a graphic representation of the logarithm of the regularised residual norm against the logarithm of the norm of the solution that has  $L$  shape. The optimal choice of the regularisation parameter is one that corresponds to a point on the curve near the ‘‘corner’’. This point represents a solution with a favourable balance between the two types of errors.[40, 14].

### 4.3.2.3 Unbiased Predicted Risk Estimator

The Unbiased Predicted Risk Estimator (UPRE) is based on the norm of the predictive error, but the variance  $\sigma^2$  of the noise (white)  $\mathbf{n}$  is used to find the optimal regularisation parameter [75]. The method consists in searching for the regularisation parameter  $\gamma$  minimising the expected value of the predictive risk  $U(\gamma)$

$$U(\gamma) = \frac{1}{n} \|\mathbf{r}_\gamma\|^2 + \frac{2\sigma^2}{n} \text{Tr}(\mathbf{A}_\gamma) - \sigma^2 \quad (4.40)$$

## 4.4 Statistical methods

Statistical methods take into account the random nature of the noise. The data are seen as a realisation of a random process. Statistical methods give an efficient means of dealing with measurement errors.

### 4.4.1 Maximum likelihood estimation

One general method of finding an estimate is the maximum-likelihood (ML) estimation. The noise probability is considered and the data and the objects are considered as deterministic. The likelihood probability distribution is given by the probability distribution of the noise. The likelihood function is defined as the likelihood function for the object  $\mathbf{f}$  given the data  $\mathbf{g}$  by

$$L(\mathbf{f}) = p(\mathbf{g}|\mathbf{f}) = p(\mathbf{n} = \mathbf{g} - \mathbf{H}\mathbf{f}) \quad (4.41)$$

The log likelihood is

$$l(\mathbf{f}) = \ln p(\mathbf{g}|\mathbf{f}) \quad (4.42)$$

The maximum-likelihood estimator is the vector  $\mathbf{f}$  that maximises the log likelihood function

$$\hat{\mathbf{f}}_{ML} = \underset{\mathbf{f}}{\text{argmax}} \{l(\mathbf{f})\} \quad (4.43)$$

The case of Poisson noise and Gaussian noise are two main cases, with sometimes a mixture between the two.



#### 4.4.1.1 Gaussian Noise

For white Gaussian noise Eq.(2.73) the covariance matrix is symmetric (section 2.4.3.1) with independent and identical distributed elements and the same known variance value  $\sigma^2$ , then  $\mathbf{K} = \sigma^2 \mathbf{I}_M$ . The determinant of the covariance matrix is  $\det(\mathbf{K}) = \det(\sigma^2 \mathbf{I}_M) = (\sigma^2)^M$ .

$$p(\mathbf{g}|\mathbf{f}) = (2\pi\sigma^2)^{-\frac{M}{2}} \exp \left[ -\frac{1}{2\sigma^2} \sum_{i=1}^M (g_i - [\mathbf{Hf}]_i)^2 \right] \quad (4.44)$$

$$\ln p(\mathbf{g}|\mathbf{f}) = \text{constant} - \frac{1}{2\sigma^2} \sum_{i=1}^M (g_i - [\mathbf{Hf}]_i)^2 \quad (4.45)$$

$$\mathcal{J}_{data}(\mathbf{Hf}, \mathbf{g}) = \sum_{i=1}^M (g_i - [\mathbf{Hf}]_i)^2 = \|\mathbf{g} - \mathbf{Hf}\|^2 \quad (4.46)$$

The ML estimation for a Gaussian noise (white or not) is equivalent to the least-square method.

$$\hat{\mathbf{f}} : \max_{\mathbf{f}} \{p(\mathbf{g}|\mathbf{f})\} \Leftrightarrow \min_{\mathbf{f}} \|\mathbf{g} - \mathbf{Hf}\|^2 \quad (4.47)$$

#### 4.4.1.2 Poisson Noise

The log probability for when the noise is a Poisson noise is given by

$$\ln \Pr(\mathbf{g}|\mathbf{f}) = \sum_{i=1}^M \{-[\mathbf{Hf}]_i + g_i \ln[[\mathbf{Hf}]_i] - \ln g_i!\} \quad (4.48)$$

Since  $\ln(g!)$  is a constant that does not affect the minimization, we can write the fit-to-data functional as

$$\mathcal{J}_{data}(\mathbf{Hf}, \mathbf{g}) = \sum_{i=1}^M \{-[\mathbf{Hf}]_i + g_i \ln[[\mathbf{Hf}]_i]\} \quad (4.49)$$

Note that in this case the discrepancy functional is not the Euclidean norm. It is defined from the Kullback-Leibler distance (KL)  $d_{KL}(\mathbf{g}_1, \mathbf{g}_2) = \sum_{i=1}^M \{g_{1i} \ln(\frac{g_{1i}}{g_{2i}})\}$

### 4.4.2 Bayesian estimation

This is a straightforward application of Bayes' theorem. In Bayesian methods, both the data and the object are treated in a probabilistic manner and it permits the use

of *a priori* information about the object. Expressing  $l(\mathbf{f}) = \ln p(\mathbf{g}|\mathbf{f})$  using Bayes' rule keeping the term of the object, Eq.(2.59) the maximum *a posteriori* estimator, or MAP estimator is given by

$$\hat{\mathbf{f}}_{MAP} = \operatorname{argmax}_{\mathbf{f}} \{\ln p(\mathbf{g}|\mathbf{f}) + \ln p(\mathbf{f})\} \quad (4.50)$$

$p(\mathbf{f})$  is called the *a priori* probability density function.

### 4.4.3 Maximum entropy

The maximum entropy principle is like other Bayesian methods in that it makes explicit use of prior information, the entropy of the object[65]. Those techniques have an extra functional in the form of  $\ln(\mathbf{f})$ . The method explicitly constrains the solution to be positive. Entropy techniques have been used for double star SCIDAR [7, 49].

## 4.5 Optimization

An iterative search for the solution can be used as regularisation. It is applicable for large problems or badly conditioned matrices. There is an iterative way of finding a solution to minimise unconstrained problems. If the form is quadratic the set of solutions is convex. If  $\mathbf{H}$  has null functions, many different  $\mathbf{f}$  can give the same  $\mathbf{H}\mathbf{f}$  and hence the same likelihood; which one is obtained by the algorithm depends on the null components of the initial estimate. A general approach to functional minimisation is to choose a search direction in the reconstruction space, take a step in that direction, and repeat the process iteratively. The iteration rule for algorithms in this class is thus

$$\hat{\mathbf{f}}_{k+1} = \hat{\mathbf{f}}_k + \tau_k \mathbf{d}_k, \quad (4.51)$$

where  $\mathbf{d}_k$  is the search direction for the  $k^{th}$  iteration and  $\tau_k$  is the size of the step in that direction.

### 4.5.1 Functional minimisation

The minimisation of the fit-to-data functional in the least-square sense (Eq.(4.46)) is

$$\|\mathbf{H} \mathbf{f} - \mathbf{g}\|^2 = (\mathbf{Hf} - \mathbf{g}, \mathbf{Hf} - \mathbf{g}) \quad (4.52)$$

$$= (\mathbf{Hf}, \mathbf{Hf}) - (\mathbf{Hf}, \mathbf{g}) - (\mathbf{g}, \mathbf{Hf}) + (\mathbf{g}, \mathbf{g}) \quad (4.53)$$

Using properties of scalar product for real space (see appendix A) we have

$$(\mathbf{Hf}, \mathbf{g}) = (\mathbf{g}, \mathbf{Hf})^* = (\mathbf{g}, \mathbf{Hf}) \quad (4.54)$$

Eq.(4.53) becomes

$$\|\mathbf{H} \mathbf{f} - \mathbf{g}\|^2 = (\mathbf{Hf}, \mathbf{Hf}) - 2(\mathbf{Hf}, \mathbf{g}) + (\mathbf{g}, \mathbf{g}) \quad (4.55)$$

When Tikhonov regularisation is used, minimising the functional (Eq.(4.32)) is equal to the quadratic form as follows

$$q(\mathbf{f}) = \frac{1}{2} \mathbf{f}^\dagger \mathbf{Q} \mathbf{f} - \mathbf{f}^\dagger \mathbf{b} + \mathbf{c} \quad (4.56)$$

with

$$\mathbf{Q} = \mathbf{H}^\dagger \mathbf{H} + \gamma \mathbf{I} \quad (4.57)$$

$$\mathbf{b} = \mathbf{H}^\dagger \mathbf{g} \quad (4.58)$$

and  $\mathbf{c}$  a constant.

$$q(\mathbf{f}) = \frac{1}{2} (\mathbf{Q} \mathbf{f}, \mathbf{f}) - (\mathbf{b}, \mathbf{f}) + \mathbf{c} \quad (4.59)$$

Replacing the value of  $\mathbf{Q}$  and  $\mathbf{b}$  in Eq.(4.59)

$$q(\mathbf{f}) = \frac{1}{2} ((\mathbf{H}^\dagger \mathbf{H} + \gamma \mathbf{I}) \mathbf{f}, \mathbf{f}) - (\mathbf{H}^\dagger \mathbf{g}, \mathbf{f}) + \mathbf{c} \quad (4.60)$$

$$= \frac{1}{2} (\mathbf{H}^\dagger \mathbf{H} \mathbf{f}, \mathbf{f}) + \frac{1}{2} (\gamma \mathbf{I} \mathbf{f}, \mathbf{f}) - (\mathbf{H}^\dagger \mathbf{g}, \mathbf{f}) + \mathbf{c} \quad (4.61)$$

Rearranging the equation with transpose operator properties, Eq.(4.61) becomes

$$q(\mathbf{f}) = \frac{1}{2} (\mathbf{Hf}, \mathbf{Hf}) + \frac{1}{2} \gamma (\mathbf{f}, \mathbf{f}) - (\mathbf{Hf}, \mathbf{g}) + \mathbf{c} \quad (4.62)$$

$$q(\mathbf{f}) = \frac{1}{2} (\mathbf{Hf}, \mathbf{Hf}) - (\mathbf{Hf}, \mathbf{g}) + \frac{1}{2} \gamma (\mathbf{f}, \mathbf{f}) + \mathbf{c} \quad (4.63)$$

Noting that if we set  $\gamma$  to zero and the constant  $\mathbf{c}$  is taken to  $\|\mathbf{g}\|^2$ , Eq.(4.63) is equal to Eq.(4.53)

We can lighten the notation of the function leaving the dependence of  $\mathbf{f}$  only;  $\mathcal{J}(\mathbf{Q}\mathbf{f}, \mathbf{b}) = \mathcal{J}(\mathbf{f})$  The gradient of  $\mathcal{J}(\mathbf{f})$  is  $\nabla \mathcal{J}_k = \mathbf{Q}\mathbf{f} - \mathbf{b}$ . It is equal to zero for  $\mathbf{Q}\mathbf{f} = \mathbf{b}$

The second derivative of  $\mathcal{J}(\mathbf{Q}\mathbf{f}, \mathbf{b})$  is called the Hessian and is equal to

$$Hess\mathcal{J}(\mathbf{Q}\mathbf{f}, \mathbf{b}) = \mathbf{Q} = \mathbf{H}^\dagger\mathbf{H} + \gamma\mathbf{I} \quad (4.64)$$

The matrix  $\mathbf{Q} = \mathbf{H}^\dagger\mathbf{H} + \gamma\mathbf{I}$  is symmetric positive definite.  $\mathbf{Q}$  is symmetric if  $\mathbf{Q} = \mathbf{Q}^\dagger$ .

$$\mathbf{Q}^\dagger = (\mathbf{H}^\dagger\mathbf{H} + \gamma\mathbf{I})^\dagger = \mathbf{H}^\dagger(\mathbf{H}^\dagger)^\dagger + \gamma\mathbf{I}^\dagger = (\mathbf{H}^\dagger\mathbf{H} + \gamma\mathbf{I}) \quad (4.65)$$

Positive definite matrix means that the eigenvalues are real and positive or that the eigenvalues are all positive. Equivalently we can write  $(\mathbf{Q}\mathbf{f}, \mathbf{f}) > 0$ .  $(\mathbf{Q}\mathbf{f}, \mathbf{f}) = ((\mathbf{H}^\dagger\mathbf{H} + \gamma\mathbf{I})\mathbf{f}, \mathbf{f}) = ((\mathbf{H}^\dagger\mathbf{H}\mathbf{f}, \mathbf{f}) + \gamma(\mathbf{I}\mathbf{f}, \mathbf{f})) > 0$ .  $\lambda^2 \|\mathbf{f}\|^2 + \gamma \|\mathbf{f}\|^2$

As  $\mathbf{Q}$  is symmetric definite positive, the functional  $\mathcal{J}(\mathbf{H}\mathbf{f}, \mathbf{g})$  is strictly convex and the minimiser  $\hat{\mathbf{f}}_\gamma$  is unique for the value of  $\gamma$ . The minimiser is given by

$$\hat{\mathbf{f}}_\gamma = (\mathbf{H}^\dagger\mathbf{H} + \gamma\mathbf{I})^{-1}\mathbf{H}^\dagger\mathbf{g} \quad (4.66)$$

Tikhonov regularisation acts as a filter on the small singular values. Using SVD decomposition one can shown that Eq.(4.66) can be written as

$$\hat{\mathbf{f}}_\gamma = w_\gamma \mathbf{f}_d \quad (4.67)$$

$$= \sum_{i=1}^N \frac{s_i (\mathbf{u}_i^\dagger \mathbf{g}_i)}{s_i^2 + \gamma} \mathbf{v}_i \quad (4.68)$$

The Tikhonov filter is

$$w_\gamma = \frac{s^2}{s^2 + \gamma} \quad (4.69)$$

#### 4.5.1.1 Steepest descent

The method of steepest descent is the simplest of the gradient methods. The search starts at an arbitrary point and then slides down the gradient; the descent converges slowly because it has to take a right angle turn after each step, and consequently search in the same direction as earlier steps. Finding the minimum of  $\mathcal{J}(\mathbf{f})$  requires

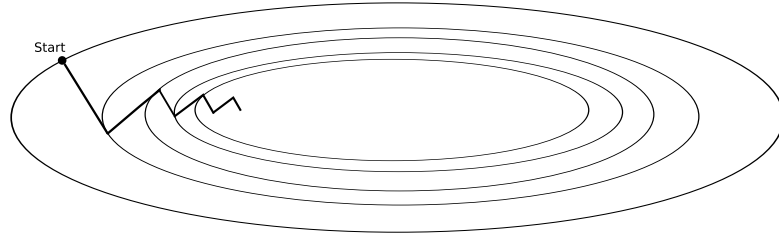


Fig. 4.1: Steepest descent method.

setting the gradient to zero, which we see is equivalent to solving the set of linear equations  $\mathbf{H}\mathbf{f} = \mathbf{g}$ .

The direction search is the negative gradient  $\mathbf{d}_k = -\nabla\mathcal{J}_k$ , and the step  $\tau_k$  is found using a line search of  $\tau_k$  that satisfies  $\tau_k = \operatorname{argmin}_{\tau>0} \{\mathcal{J}(\mathbf{f}_{k+1} + \tau_k\mathbf{d}_k)\}$ . The new iteration is given by  $\mathbf{f}_{k+1} = \mathbf{f}_k + \tau_k\mathbf{d}_k$ . For a symmetric positive definite matrix  $\mathbf{Q}$  an optimal step exists and is given by

$$\tau_k = \frac{\nabla\mathcal{J}_k^\dagger \nabla\mathcal{J}_k}{\nabla\mathcal{J}_k^\dagger \mathbf{Q} \nabla\mathcal{J}_k} \quad (4.70)$$

#### 4.5.1.2 Conjugate gradient descent

The minimum is reached in fewer steps than would be the case using the method of steepest descent. In the conjugate gradient descent technique, the new search direction is taken to be orthogonal to the previous one with respect to the quadratic matrix  $\mathbf{Q}$ [53]. Given a symmetric matrix  $\mathbf{Q}$ , two vectors  $\mathbf{d}_1$  and  $\mathbf{d}_2$  are said to be  $\mathbf{Q}$ -orthogonal, or conjugate with respect to  $\mathbf{Q}$ , if  $(\mathbf{d}_1^\dagger \mathbf{Q} \mathbf{d}_2) = 0$ . The method is as follows:

Start with the direction given by the initial negative gradient  $\mathbf{d}_0 = -\nabla\mathcal{J}_0$ , then use  $\mathbf{d}_k$  to update the iteration  $\mathbf{f}_{k+1} = \mathbf{f}_k + \tau_k\mathbf{d}_k$ , where  $\tau_k$  is defined as

$$\tau_k = -\frac{\nabla\mathcal{J}_k^\dagger \mathbf{d}_k}{\mathbf{d}_k^\dagger \mathbf{Q} \mathbf{d}_k} \quad (4.71)$$

Calculate the new conjugate gradient direction  $\mathbf{d}_{k+1}$ ,  $\mathbf{d}_{k+1} = -\nabla\mathcal{J}_{k+1} + \beta_k\mathbf{d}_k$

$$\beta_k = \frac{(\nabla\mathcal{J}_{k+1}^\dagger \mathbf{Q} \mathbf{d}_k)}{\mathbf{d}_k^\dagger \mathbf{Q} \mathbf{d}_k} \quad (4.72)$$

**Non-quadratic conjugate gradient** For the non-quadratic case other techniques exist like Fletcher-Reeves and Polak-Robiere methods. The differences are

that  $\tau_k$  is found using a line search and that  $\beta$  is defined differently. We have

$$\beta_k = \frac{(\nabla \mathcal{J}_{k+1}^\dagger \nabla \mathcal{J}_{k+1})}{(\nabla \mathcal{J}_k^\dagger \nabla \mathcal{J}_k)} \quad (4.73)$$

for the Fletcher-Reeves method or

$$\beta_k = \frac{(\nabla \mathcal{J}_{k+1} - \nabla \mathcal{J}_k)^\dagger \nabla \mathcal{J}_{k+1}}{\nabla \mathcal{J}_k^\dagger \nabla \mathcal{J}_k} \quad (4.74)$$

for the Polak-Robiere method.

## 4.6 Non-negativity

If a non-negative solution is sought, a constraint to the solution has to be used. The solutions will be searched on the set of non-negative objects. For the unconstrained problem, the minimum is found for the  $\mathbf{f}$  that solves

$$\frac{\partial \mathcal{J}(\mathbf{H}\mathbf{f}, \mathbf{g})}{\partial f_i} = 0 \quad (4.75)$$

for  $i$  at  $\mathbf{f} = \hat{\mathbf{f}}$ .

Now if a constraint of positivity is applied, the problem to solve is

$$\min \mathcal{J}(\mathbf{H}\mathbf{f}, \mathbf{g}) \text{ subject to } \mathbf{f} \geq 0 \quad (4.76)$$

The minimum may not occur at a point of zero derivative; it can also occur when one or more of the components  $f_n$  are zero, so long as the derivative is positive at this point. More conditions to find a minimum arise

$$\begin{cases} f_i \frac{\partial \mathcal{J}(\mathbf{H}\mathbf{f}, \mathbf{g})}{\partial f_i} = 0 \\ \frac{\partial \mathcal{J}(\mathbf{H}\mathbf{f}, \mathbf{g})}{\partial f_i} \geq 0 \end{cases} \quad (4.77)$$

for  $i$  at  $\mathbf{f} = \hat{\mathbf{f}}$ . These are the Karush-Kuhn-Tucker (KKT) conditions. These conditions imply that if  $\frac{\partial \mathcal{J}(\mathbf{H}\mathbf{f}, \mathbf{g})}{\partial f_i} > 0$ , then  $f_i = 0$  for  $i$  at  $\mathbf{f} = \hat{\mathbf{f}}$  and conversely.

### 4.6.1 Reparametrisation

Reparametrisation[21] allows to find a positive solution rewriting the object  $\mathbf{f}$  as a positive quantity such as an exponential or a square quantity.

For a square reparametrisation,  $\mathbf{f} = \mathbf{x}^2$

$$\mathcal{J}(\mathbf{H}\mathbf{x}^2, \mathbf{g})^{sr} = \|\mathbf{H}\mathbf{x}^2 - \mathbf{g}\|^2 + \gamma \|\mathbf{x}^2\|^2 \quad (4.78)$$

For an exponential reparametrisation  $\mathbf{f} = e^{\mathbf{z}}$

$$\mathcal{J}(\mathbf{H}e^{\mathbf{z}}, \mathbf{g})^{er} = \|\mathbf{H}e^{\mathbf{z}} - \mathbf{g}\|^2 + \gamma \|e^{\mathbf{z}}\|^2 \quad (4.79)$$

Note the exponential parameterisation has a physical interpretation in image restoration. If the entries in  $\mathbf{f}$  represent pixel intensities, then the entries in  $e^{\mathbf{z}}$  represent densities[39].

The drawback is that these reparametrisations change the error surface creating other extrema. The functionals are not convex and there is not a unique and stable solution.

## 4.6.2 Feasibility set and active set

The feasibility set, or constraint set  $\Omega$  is the set of objects that are non-negative, defined by

$$\Omega = \mathbf{f} | \mathbf{f} \geq 0 \quad (4.80)$$

The active set is a set that is enclosed in the feasible set. For nonnegativity constraint the feasible set is the vectors that are greater than or equal to 0. The feasible set is given by  $\Omega(\mathbf{f}) = f_i | f_i \geq 0$ . In the discrete case, where the objects to estimate is described by  $\mathbf{f} = f_i, i = 1, \dots, N$ , the active set is given by  $\mathcal{A}(\mathbf{f}) = \{i | f_i = 0\}$ . The complementary set to the active set is the inactive set, noted  $\mathcal{I}(\mathbf{f})$

The projected gradient of  $\mathcal{J}(\mathbf{H}\mathbf{f}, \mathbf{g})$  at  $\mathbf{f}$  on the feasibility set  $\Omega$  is given by

$$[\nabla_{\Omega} \mathcal{J}(\mathbf{H}\mathbf{f}, \mathbf{g})]_i \begin{cases} \frac{\partial \mathcal{J}(\mathbf{H}\mathbf{f}, \mathbf{g})}{\partial f_i} \in \mathcal{I}(\mathbf{f}) \\ 0 \text{ if } i \in \mathcal{A}(\mathbf{f}) \end{cases} \quad (4.81)$$

Let  $[\mathbf{D}_{\mathcal{I}}(\mathbf{f})]$  denote the diagonal matrix defined as

$$\mathbf{D}_{\mathcal{I}}(\mathbf{f})_{ii} = \begin{cases} 1 \text{ if } i \in \mathcal{I}(\mathbf{f}) \\ 0 \text{ if } i \in \mathcal{A}(\mathbf{f}) \end{cases} \quad (4.82)$$

Then

$$\nabla_{\Omega} \mathcal{J}(\mathbf{H}\mathbf{f}, \mathbf{g}) = \mathbf{D}_{\mathcal{I}}(\mathbf{f}) \nabla \mathcal{J}(\mathbf{H}\mathbf{f}, \mathbf{g}) \quad (4.83)$$

### 4.6.3 Projector on the feasibility set

The projector operator in the feasible set is the operator that sets to zero the negative values.

$$\mathcal{P}_{\Omega}\{\mathbf{f}\} = \begin{cases} f_i & \text{if } f_i \geq 0 \\ 0 & \text{otherwise} \end{cases} \quad (4.84)$$

## 4.7 Single star SCIDAR problem

Tikhonov-Miller regularisation[42, 80, 12] can be used to perform the inversion of the double star SCIDAR [46]. The Tikhonov regularisation method was also used by Stevens[66]. This method seems to be interesting to apply for the single star SCIDAR, and is the main contribution of this thesis.

Reverting to the inversion problem, we can rewrite Eq.(3.63) in matrix form, using the formalism of this chapter:

$$\mathbf{g} = \mathbf{H}\mathbf{f} + \mathbf{n}, \quad (4.85)$$

where  $\mathbf{H}$  represents the  $M \times N$  matrix kernel  $K(r, h)$  containing the theoretical autocovariance of a single star,  $\mathbf{g}$  the autocovariance  $B(r)$   $M \times 1$  vector measurements and  $\mathbf{n}$  the  $M \times 1$  vector noise. We need to invert Eq.(4.85) to obtain the refractive index profile  $C_n^2(h)$ , represented by  $\mathbf{f}$  the  $N \times 1$  vectors. The problem to be solved is an ill-posed one. The restoration of the profile is achieved by a maximum likelihood approach leading to a least square method solution assuming Gaussian noise using a quadratic programming[45]. The use of several measurement planes improves the condition of the matrix for a better resolution of the inverse problem. With  $p$  measurement planes Eq.(4.85) becomes

$$\mathbf{g}_{MP} = \mathbf{H}_{MP} \mathbf{f}_{MP} + \mathbf{n}, \quad (4.86)$$

where  $\mathbf{H}_{MP} = [\mathbf{H}_1, \dots, \mathbf{H}_p]^T$  is a matrix containing now  $m$  single star theoretical autocovariance matrices  $\mathbf{H}_i$ , with  $i = 1..p$  corresponding to the  $m$  measurements planes and  $\mathbf{g}_{MP} = [\mathbf{g}_1, \dots, \mathbf{g}_p]^T$  is obtained by putting the matrix of single star covariance corresponding to each measurement plane  $\mathbf{g}_i$  with  $i = 1..p$  into a vector. Assuming there are enough photons and we are limited only by the read out noise



of the detector, Gaussian noise in the autocorrelation data is assumed, and the function to minimise is a quadratic form:

$$\mathcal{J}_{data}(\mathbf{H}\mathbf{f}, \mathbf{g}) = \|\mathbf{H}_{MP}\mathbf{f} - \mathbf{g}_{MP}\|^2, \quad (4.87)$$

where  $\mathbf{g}$  is the autocorrelation data. A Tikhonov regularisation Eq.(4.31) is utilised to regularise this ill-posed problem. The new quadratic form to minimise is:

$$\mathcal{J}(\mathbf{H}\mathbf{f}, \mathbf{g}) = \|\mathbf{H}_{MP}\mathbf{f} - \mathbf{g}_{MP}\|^2 + \gamma \|\mathbf{f}_{MP}\|^2 \quad (4.88)$$

Quadratic programming[45] is used for inversion. The algorithm is as follows:

- 1 Start with a initial estimate  $\mathbf{f}_0$
- 2 The active set is defined for  $\frac{\partial \mathcal{J}(\mathbf{H}\mathbf{f}, \mathbf{g})}{\partial f_i} > 0$  and  $f_i < 0$ . A new estimate is obtained by the conjugate gradient method on the active set to obtain the new estimate  $\tilde{\mathbf{f}}_k$ .
- 3 Update the new estimate  $\mathbf{f}_{k+1} = \mathcal{P}\{\mathbf{f}_k + t_k(\tilde{\mathbf{f}} - \mathbf{f}_k)\}$ , where  $t_k$  in the range  $0 < t_k \leq 1$  is the bigger value ensuring  $\mathcal{J}_{data}(\mathbf{H}\mathbf{f}_{k+1}, \mathbf{g}) \leq \mathcal{J}_{data}(\mathbf{H}\mathbf{f}_k, \mathbf{g})$
- 4 The new active set is updated then go back to step 1.

---

## Chapter 5

# Single star SCIDAR equipment and data collection

---

The single star SCIDAR instrument was designed and constructed by Derek Coburn, a researcher in the Applied Optics Group, in consultation with myself and Prof. Dainty. The instrument is designed to record a sequence of pupil images of the same target at different defocussing heights (i.e. generalised SCIDAR mode). The single star SCIDAR instrument had to adhere to a number of requirements. A short exposure time, on the order of a millisecond, is needed to freeze the turbulence, and thus the scintillation pattern. The frame rate has to be high so that many statistically independent frames can be obtained to yield a large signal to noise ratio in the ensemble average autocovariance signal. A frame rate of about 100 Hz was achieved with the system. To get a good sky coverage, the sensitivity of the camera has to be high to access more stars in the sky. The change of height conjugation has to be fast. Ideally a real time output of the autocovariance is desirable, with the corresponding  $C_n^2(h)$  profile as well. The operation of acquisition, processing and alignment should ideally be done remotely. The instrument has to be portable to move from site to site. It should not have to be dedicated to a specific large telescope.

### 5.1 Instrument considerations

For a generalised SCIDAR system to reproduce scintillation patterns for target conjugate heights, a number of primary constraints must be satisfied [32]. The complex amplitude produced by one layer at an altitude  $h$ , propagates to the telescope pupil,

crosses the pupil and finally propagates to a conjugate plane at a distance  $d$  is given by [32]

$$\Psi_d(\mathbf{r}) \propto \left[ \mathcal{F}_{\frac{r}{\lambda d}}[P(\mathbf{r})] * \Psi_h\left(\frac{-h\mathbf{r}}{d}\right) \exp\left(\frac{i\pi r^2}{\lambda d}\left(\frac{h}{d}\right)\right) \right] \quad (5.1)$$

In Eq.(5.1)  $P$  is the pupil function of the telescope and  $\mathcal{F}_{\frac{r}{\lambda d}}$  means a Fourier transform evaluated at  $\frac{r}{\lambda d}$ .

The first constraint, related to the inherent diffraction limit of the instrument on the system imaging and the impact of a quadratic phase term on system imaging, is satisfied provided the size of the limiting aperture of the system is

$$D \gg \sqrt{\lambda h} \quad (5.2)$$

where  $h$  is the height of the layer of interest. The second condition relates to the diffraction limited performance in reproducing the phase and amplitude variations associated with the turbulence at the target layer. The coherence length must be wide enough to be sampled by the point spread function of the system imaging. The width of the point spread response associated with the limiting aperture of the system must be smaller than the average patch radius  $r_0$  over which the phase of the wavefront changes by  $\pi$ . The corresponding condition is,

$$D \gg \frac{\lambda h}{r_0} \quad (5.3)$$

The phase corrugations of the perturbed wavefront at the layer do not impact on the recorded scintillation data. Following similar reasoning it is necessary for the point spread function of the instrument to be sufficiently narrow to resolve the scintillation at the given layer in order to avoid blurring out of the scintillation. Therefore,

$$D \gg \frac{\lambda h}{\delta r}, \quad (5.4)$$

where  $\delta r$  is the minimum scale size of the scintillation produced by the layers above or below the target height. Together, these conditions indicate the height in the atmosphere (or, in generalised mode the height below the telescope pupil) that it is possible to conjugate to while faithfully reproducing the scintillation pattern for the target pupil given the pupil width of the imaging system. In practical terms portable telescopes whose aperture sizes range from 200 - 400 mm in width, for a wavelength of 550 nm, are limited to target heights less than 1 or 2 km from the

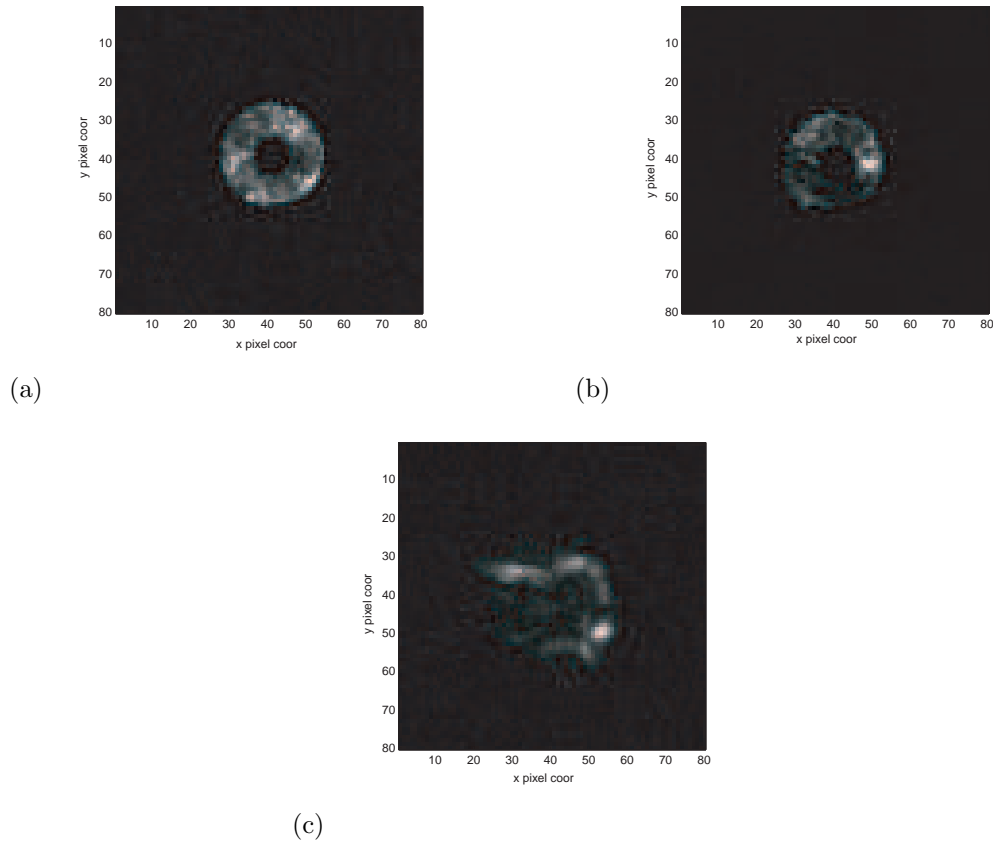


Fig. 5.1: Scintillation image of Capella at pupil plane (a), defocused at +2km (b) and defocused at +5.8km (c). Diffraction effects are significant for a defocussing of 5.8 km.

telescope pupil in order to minimise the impact of the instrument's diffraction limit on recorded patterns. Outside of this regime the diffraction effect of the instrument must be folded in to the analysis used to retrieve the  $C_n^2$  profile from the data and in general the assumption that the statistics of the scintillation is invariant across the sensing aperture is lost. Fig. 5.1 shows the scintillation patterns for different defocussing. Fig. 5.1c clearly shows the impact of the telescope finite pupil on a defocused pattern.

## 5.2 Instrument design

The single star SCIDAR instrument consists of a pupil imaging system bolted to the back flange of a 250mm diameter, f/10 Meade telescope. The LX200 series telescope

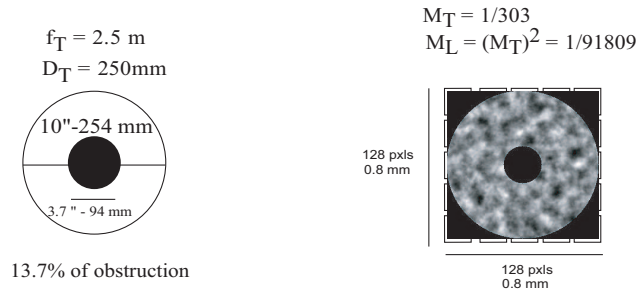


Fig. 5.2: Correspondance between telescope pupil and detected image.

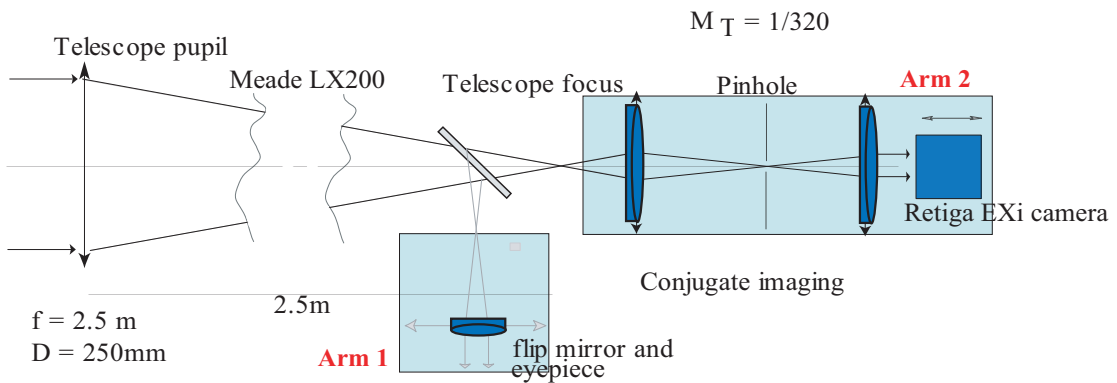


Fig. 5.3: Details of the single star SCIDAR system.

used was chosen with a view to the potential portability of the final single star SCIDAR device. The inherent benefits of this telescope are its global positioning system (GPS) assisted alignment, target “goto” functionality to point at the desired target and automated tracking. Its weakness is its poor mechanical construction: it is not designed for the mounting of scientific instruments. In operation, the telescope tracking error causes the defocussed pupil images of the SCIDAR instrument to move on the detector plane. Although the field of view of the instrument is of the order of 1 arcminute, excessive tracking error is undesirable as it can invalidate the measurement and requires that a larger area of the sensing camera be read, slowing frame acquisition times. With this in mind the tracking accuracy of the scope was supplemented by a separate tracking telescope fitted with an autoguider camera. This system, which piggybacks on top of the main tube of the LX200, gives a tracking accuracy in principle of the order of an arcsecond.

Fig. 5.3 shows detail of the system optics and Fig. 5.4 shows a photograph of the

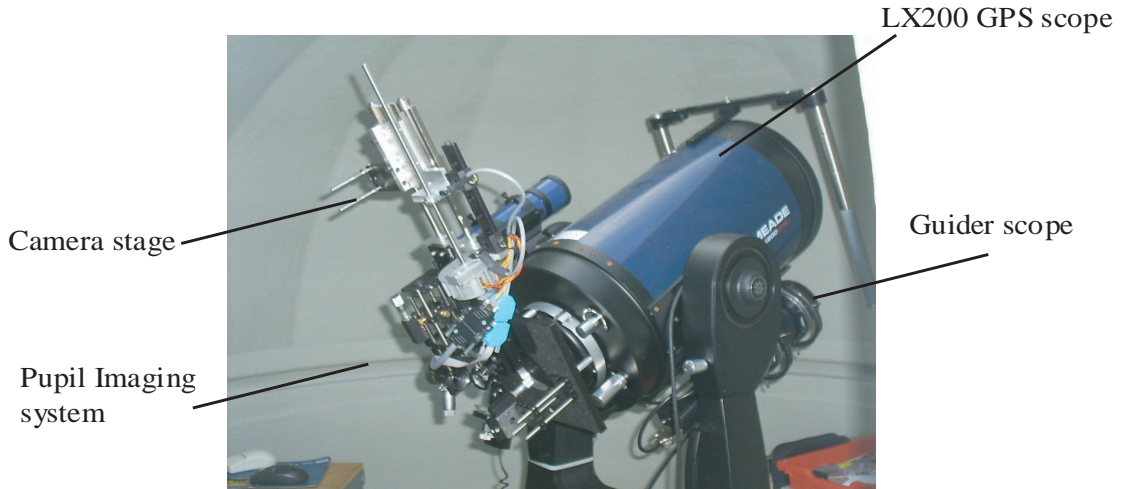


Fig. 5.4: System in the dome in Galway.

setup. The pupil imaging system at the output of the telescope contains two main optical arms with a flip mirror to direct the light along one or other as required. Arm 1 of the instrument houses an eyepiece to enable target star acquisition and centring. The optics in this arm can be interchanged with a DIMM measurement instrument if required to enable independent assessment of the turbulence conditions. At the time of development it was hoped that results from the instrument would eventually be assessed by comparing them with measurements obtained from simultaneous DIMM measurements. Arm 2 of the instrument contains the main pupil imaging and detection optics for the instrument. This conjugate imaging system in combination with the computer controlled camera stage allows heights from + 5.8 km to - 4.5 km to be targeted by the image sensor (in practice the telescope pupil limits the range to less than this). In operation the single star SCIDAR instrument produces demagnified pupil images of width  $\sim 0.78$  mm ( $M_T = 1/320$ ). This folds the lateral extent of the pupil targets from  $\sim 10$ km in object space down to 100mm in the conjugate image space ( $M_L = M_T^2$ ).

The system employs a Retiga EXi CCD camera interfaced to a standard desktop computer to sense and record the scintillation patterns formed by the conjugate imaging optics. This non-intensified camera has an rms read noise of  $8e^-$  with a spectral response extending from 400nm through the near infrared at a wavelength of 900 nm. In operation only a sub region of the 1.4 Mpixel CCD array is needed

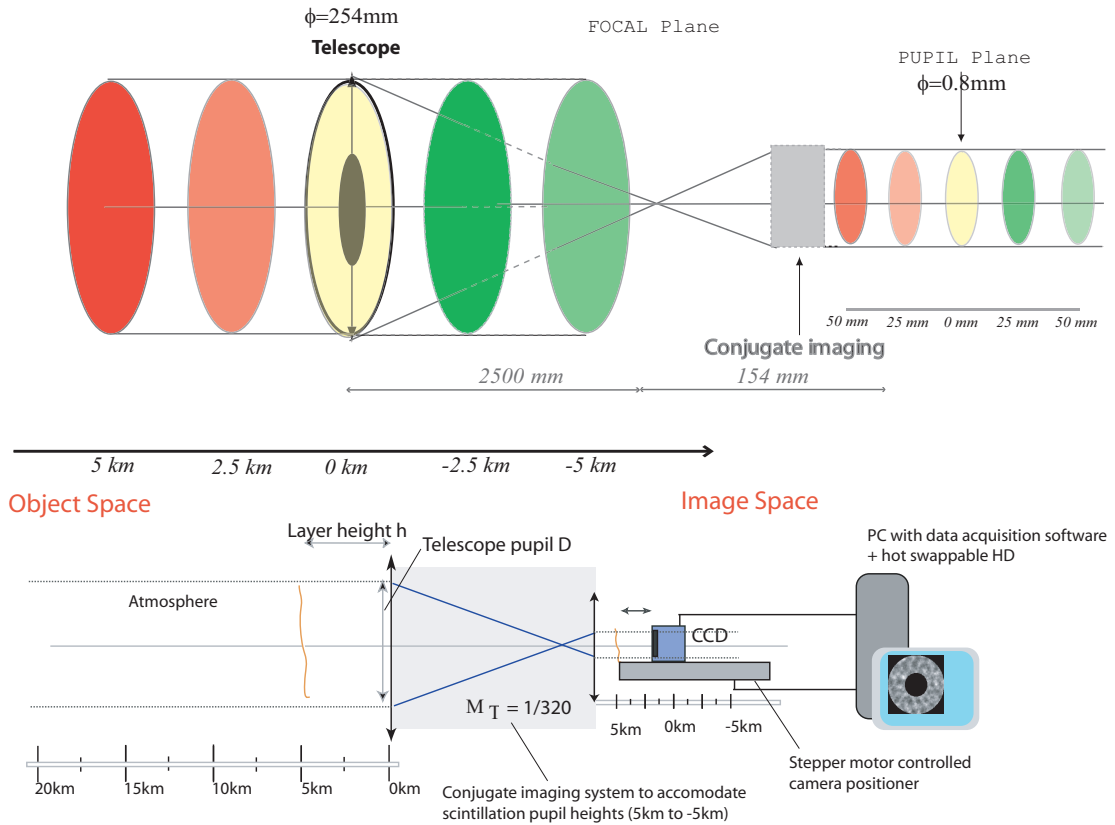


Fig. 5.5: Layout of the single star SCIDAR system.

to capture the extent of the pupil images. In addition, pixel binning is employed to give a spatial sampling size per pixel of  $\sim 0.8 \text{ mm} \times 0.8 \text{ mm}$  in the pupil for a binning by 4. Combining the region of interest and pixel binning give a maximum attainable frame rate of 110fps for exposure times of the order of 1ms (a typical exposure needed to freeze the scintillation). A star of visual magnitude 0.08 gives an approximate photon flux of over the bandwidth of the instrument of  $3400 \text{ photons.cm}^{-2}.\text{ms}^{-1}$ [3].

To conjugate to the required pupil heights the camera is moved laterally along the optical axis of the system by means of a stepper motor controlled stage. The stage enables the camera to be displaced in 0.025 mm steps in the image space at a maximum step rate of 300 steps/sec enabling the system to transfer quickly between target pupil heights. (In object space the camera motion translates to a rate of 800 m per second).

The camera and positioning stage are controlled by a purpose built PC using

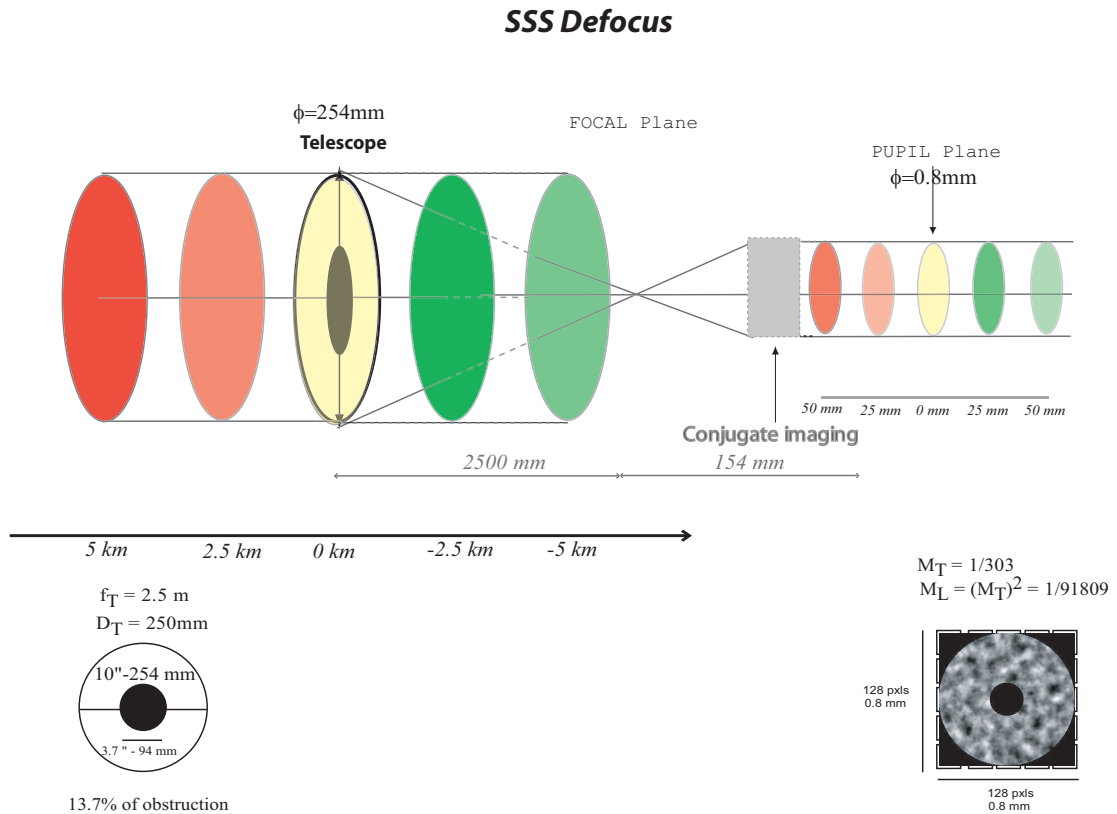


Fig. 5.6: Sequenced generalised single star SCIDAR.

acquisition software. This code has two main modes of operation “alignment and pupil image preview” and “test” mode. The active mode and basic settings of the system are controlled via a window-based graphical user interface and a text script file. In test mode the acquisition sequence is configured by a script file which dictates predefined exposure times, number of frames per sequence, target conjugate heights, camera region of interest and pixel binning setting. By modifying this simple text script it is possible to modify the details of an acquisition run quite readily. In the current system the live pupil images are archived to disk for off line analysis with only the basic image processing being performed on them in real time, namely dark image subtraction and flat field image correction. A basic test run consists of a cycle through a series of conjugate image planes (typically conjugate to +2km, +1km, 0km, -1km and -2km as specified by the script file). At each test plane a series of several thousand frames are recorded for the predefined frame exposure specified in the test configuration script. The basic data set consists of a series of



several thousand uncompressed tiff files indexed by a log file which records the time of acquisition of each file and target plane details as well as error status (if any) for frame reads and real time image processing.

### 5.3 Calibration

As the instrument performance relies on targeting different layers in the atmosphere, it is necessary to calibrate the height conjugation realised by the system. The calibration is performed by assessing relative pupil displacements of binary star components as a function of target heights programmed for the system. This enables the telescope entrance pupil and true conjugate magnification of the system to be determined.

### 5.4 Data reduction

Data reduction consists of reducing the thousands of scintillation frames to autocovariance data. The different conditions to reduce diffraction effects Eqs.(5.2), (5.3) and (5.4) are assumed to be respected. For a given pupil height, the scintillation

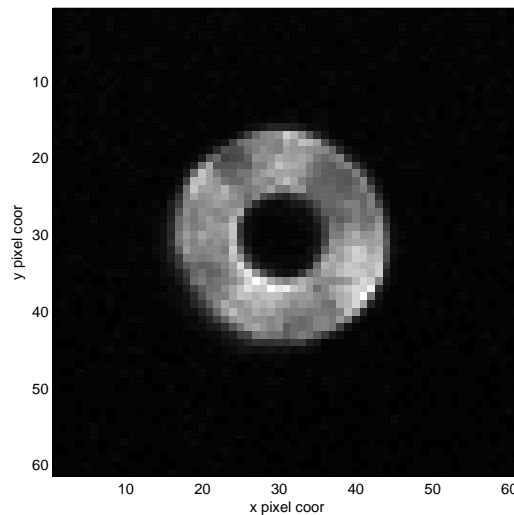


Fig. 5.7: Scintillation pattern for no pupil defocus.

index and average intensity per pixel are first calculated. A typical frame obtained

for no defocus is shown in Fig. 5.7. We calculate the relative normalised intensity for each frame[49, 68, 46]

$$I_i^n(x, y) = \frac{I_i(x, y) - \langle I(x, y) \rangle}{\langle I(x, y) \rangle}, \quad (5.5)$$

where  $\langle I(x, y) \rangle$  is the average intensity (Fig. 5.8). Pupil wander in defocus mode causes the scintillation pattern image to move on the detector. The pupil wander is due to two reasons; the autoguider did not track the star accurately and the main one is due to the tip/tilt atmospheric turbulence component of the phase changing and making the pupil image move on the detector. The tip/tilt effect gives a displacement of  $\pm 6$  pixels for target  $h=1\text{km}$ . Here, the average intensity is obtained by re-centring each frame by use of cross-correlation of the frames with the first one. The method is accurate to  $\pm 1$  pixel. Thus, in the normalisation pixels around on the edges of the average intensity are set close to zero.

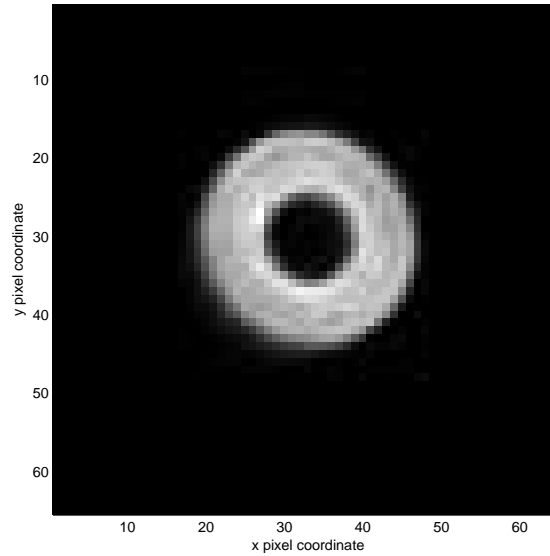


Fig. 5.8: Average scintillation pattern at the pupil plane obtained over 2000 frames.

The scintillation index can be calculated by averaging the relative intensities over all the  $N$  frames.

$$\sigma_i(x, y) = \frac{1}{N} \sum_{i=1}^N I_i^n(x, y) \quad (5.6)$$

The autocorrelation of each frame is obtained by Fourier transform

$$B_i^n(x, y) = \mathcal{F}^{-1}\{\mathcal{F}\{|I_i^n(x, y)|^2\}\} \quad (5.7)$$

The mean autocorrelation(Fig. 5.9) is taken on the average of the frames

$$B^{\text{mean}}(x, y) = \frac{1}{N} \sum_{i=1}^N B_i^n(x, y) \quad (5.8)$$

In order to account for the inherent suppression of data within the correlation

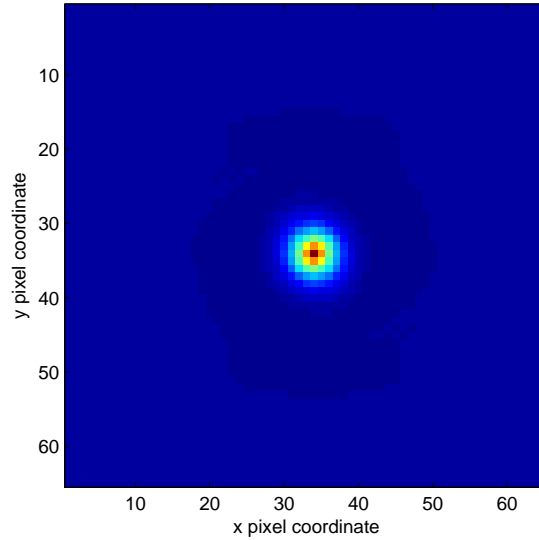


Fig. 5.9: Mean autocorrelation.

plane for large separation the resulting correlation is divided element by element by the autocorrelation of the pupil function (Fig. 5.10)(i.e. following the standard approach employed in binary SCIDAR [49]). This reflects the fact that there are fewer data autocorrelation of the average pupil function defined by points in the image to assess autocorrelation signal as the baseline separation is increased. The corrected autocorrelation is then (Fig. 5.11)

$$B(x, y) = \frac{B^{\text{mean}}(x, y)}{[Pup(x, y) \star Pup(x, y)]} \quad (5.9)$$

Assuming isotropy of turbulence,  $B(x, y)$  is used to obtain the one dimensional covariance  $B(r)$  built over radial cuts of the two dimensional correlation function (Fig. 5.12). The final autocorrelation is obtained by making an average over the radial distance (Fig. 5.13). This procedure is performed for all different altitude conjugations. Finally each autocorrelation  $B(r)_d$  is concatenated to build the system response for the turbulence conditions  $B_{MP}(r)$  (Fig. 5.14). This average is

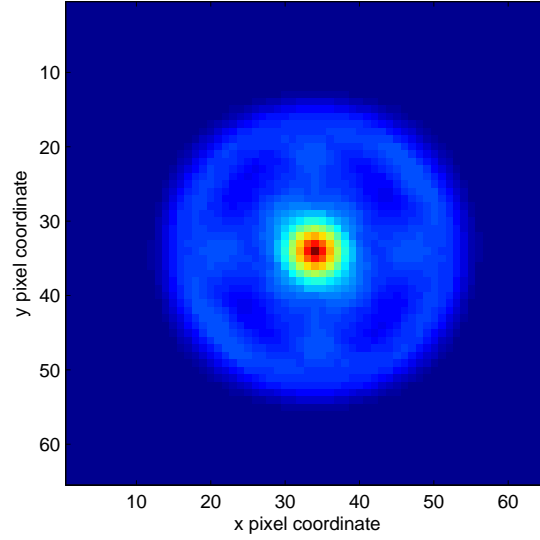


Fig. 5.10: Autocorrelation of the pupil function.

made over an extended period  $\simeq 5$  minutes.

$$B_{MP}(r) = [B_1 B_2 \dots B_P] \quad (5.10)$$

The theoretical autocorrelation used for the inversion, to obtain the  $C_n^2(h)$  profiles is built by concatenating the autocorrelation at the different measuring planes. The wavelength used is the mean wavelength from the spectrum of the star over the bandwidth of the camera.

Preliminary results of data obtained at an observing site in Galway, Ireland (between April 2005 and September 2005) with the instrument show the scintillation index  $\sigma_I^2$  for stars close to range from 0.05 to 0.35 indicating the scintillation is within the weak perturbation regime.

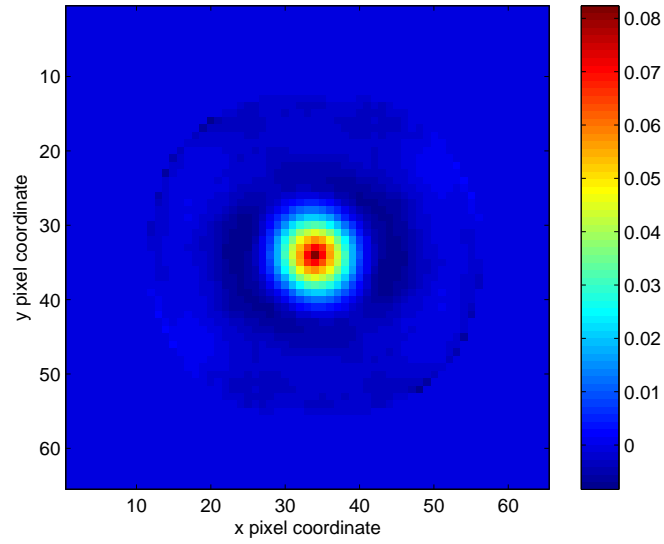


Fig. 5.11: Corrected normalised autocorrelation.

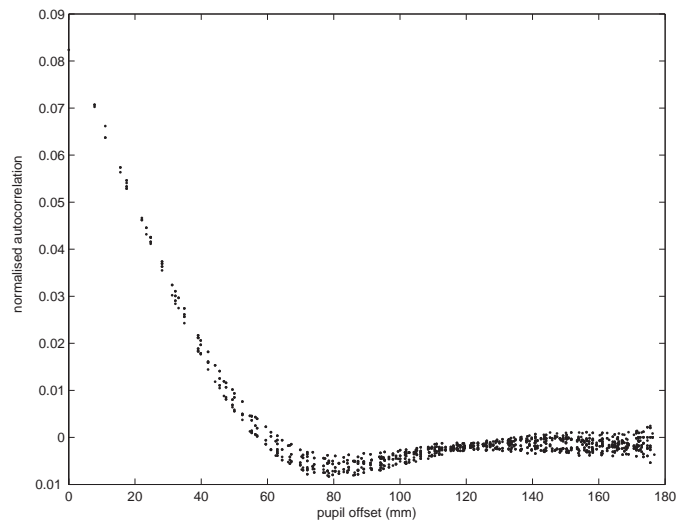


Fig. 5.12: One dimensional radial cuts autocorrelation. The spread of all the autocorrelations gives an idea of the noise.

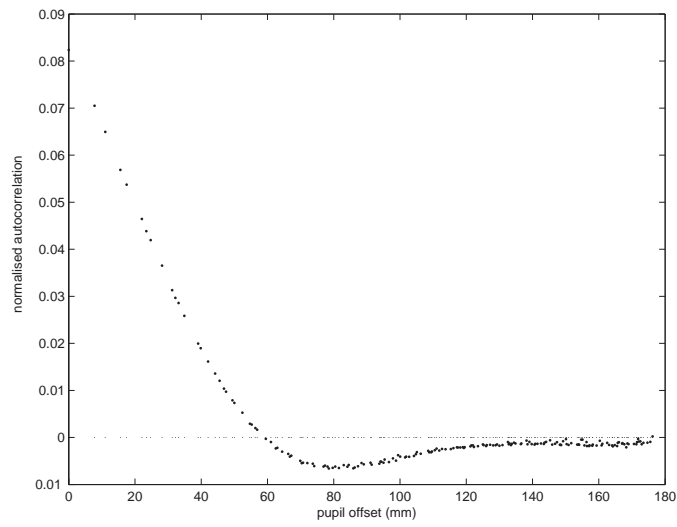


Fig. 5.13: One dimensional averaged autocorrelation.

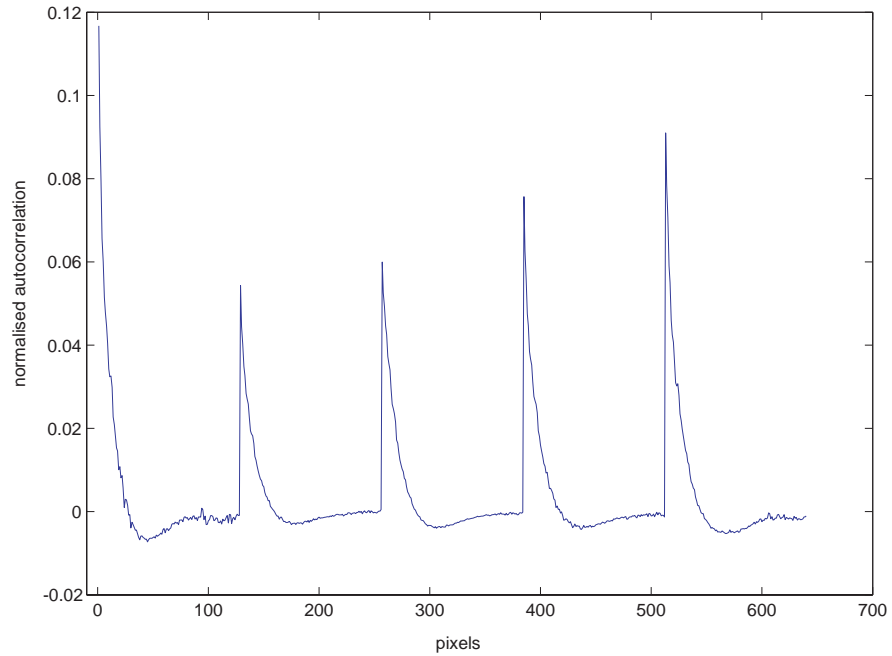


Fig. 5.14: Concatenated autocorrelation cuts from 5 defocussing values. The autocorrelations are ordered from the bigger altitude conjugation above the telescope pupil up to the bigger one below the telescope.

---

# Chapter 6

## Single star simulations

---

When a plane wave from a star propagates through atmospheric turbulence, it undergoes deformation due to the refractive index fluctuations. We assume weak phase perturbations, which is valid for observing at a good site at least for zenith angles less than approximately 60 deg. The structure of the atmosphere is assumed to be made of a finite number of thin layers, with free space in between where the wave propagates according to Fresnel propagation. The phase screens used in the simulations follow Kolmogorov statistics and were generated using the midpoint interpolation method[47]. In addition, weak turbulence theory is used, i.e. the value at the origin of the autocorrelation function, the scintillation index, is very much less than one.

### 6.1 Phase screens

Fast phase screen code provided by R.A Johnston<sup>1</sup> has been used to generate Kolmogorov phase screens using the midpoint displacement technique[41]. Before using them in the propagation process, a check has been made to see if they were following the Kolmogorov law. 1,000 phase screens have been generated for different screen resolutions and different  $\frac{D}{r_0}$  ratio.  $D$  is the size of the screen and  $r_0$  is the Fried parameter Eq.(3.16). A  $\frac{D}{r_0}$  ratio equal to one means the average patch of coherence in the phase screen  $r_0$  is equal to the whole size of the screen. The more the ratio increases the more patches of coherence will be present. Two examples for different  $\frac{D}{r_0}$  are given in Fig. 6.1 and in Fig. 6.2.

---

<sup>1</sup> Rachel Johnston of Applied Research Associates New Zealand

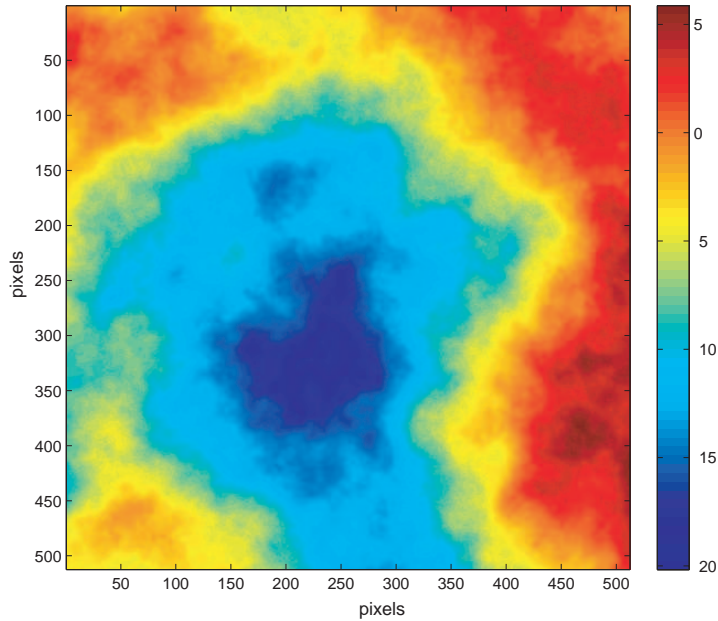


Fig. 6.1: Phase screen with  $\frac{D}{r_0} = 13$ . The colour scale is in radians.

One verification is to check if the structure function as defined in Eq.(6.1) was equal to the theoretical one Eq.(6.2). The structure function of the phase,  $D_\phi(\Delta r)$  as defined in Eq.(3.9) is

$$D_\phi(\Delta r) = \langle [\phi(r) - \phi(r + \Delta r)]^2 \rangle \quad (6.1)$$

It has the following expression in near field,

$$D_\phi(\Delta r) = 6.88 \left( \frac{\Delta r}{r_0} \right)^{\frac{5}{3}} \quad (6.2)$$

The calculation was made horizontally and vertically, for almost all the combinations size screens  $\frac{D}{r_0}$ . The Fig. 6.3 shows the horizontal, vertical and theoretical structure function for a screen resolution of 512x512 and a  $\frac{D}{r_0}$  ratio of 13 using a loglog scale. We can see that three lines are almost overlapping.

## 6.2 Propagation through turbulence

Fig. 6.4 illustrates the propagation through the atmospheric turbulence of a plane wave (at altitude  $h$ ), passing through one layer (with thickness  $\delta h$ ) and arriving to the ground. The propagation of a plane wave passing through one layer at altitude



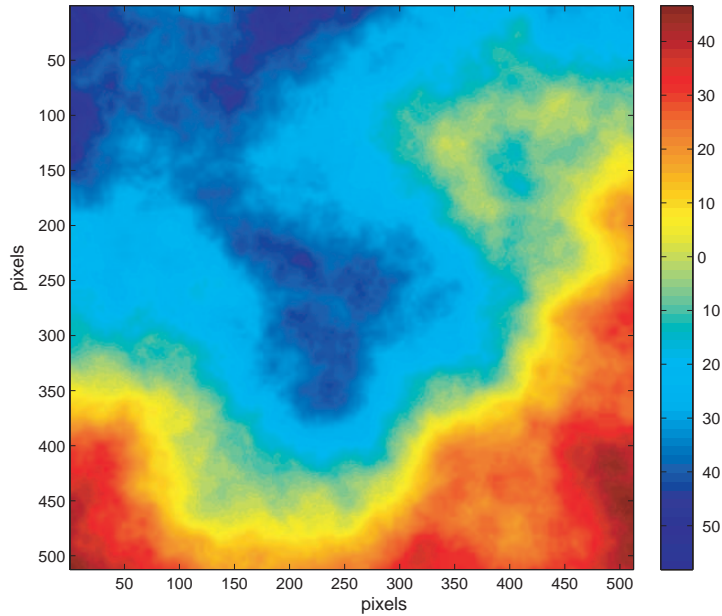


Fig. 6.2: Phase screen with  $\frac{D}{r_0} = 50$ . The colour scale is in radians. Note that this figure looks the same statistically as Fig. 6.1 but the scale is different.

$h$  with thickness  $\delta h$ , and arriving at the ground is expressed in two steps (section 3.2.1):

1. Through turbulent layers

$$\Psi_h(\mathbf{r}) = \Psi_{h+\delta h}(\mathbf{r}) \exp(i\phi(\mathbf{r})), \quad (6.3)$$

with  $\phi(\mathbf{r})$  the phase perturbation induced by the layer.

2. Fresnel propagation

$$\Psi_0(\mathbf{r}) = \Psi_h(\mathbf{r}) * \frac{1}{i\lambda h} \exp\left(\frac{i\pi\mathbf{r}^2}{\lambda h}\right), \quad (6.4)$$

where  $*$  denotes convolution.

The first regime is a simple multiplication of functions (or matrices). The wave undergoes Fresnel propagation  $p_h(\mathbf{r})$  (section 3.2.1), which is the second term of Eq.(6.4), over a distance  $h$ .

$$p_h(\mathbf{r}) = \frac{1}{i\lambda h} e^{\frac{i\pi\mathbf{r}^2}{\lambda h}} \quad (6.5)$$

To evaluate  $\Psi_0(\mathbf{r})$  after the Fresnel propagation in Eq.(6.4) we use the convolution theorem (Eq.(2.21)) of the Fourier transform making a multiplication of the Fourier

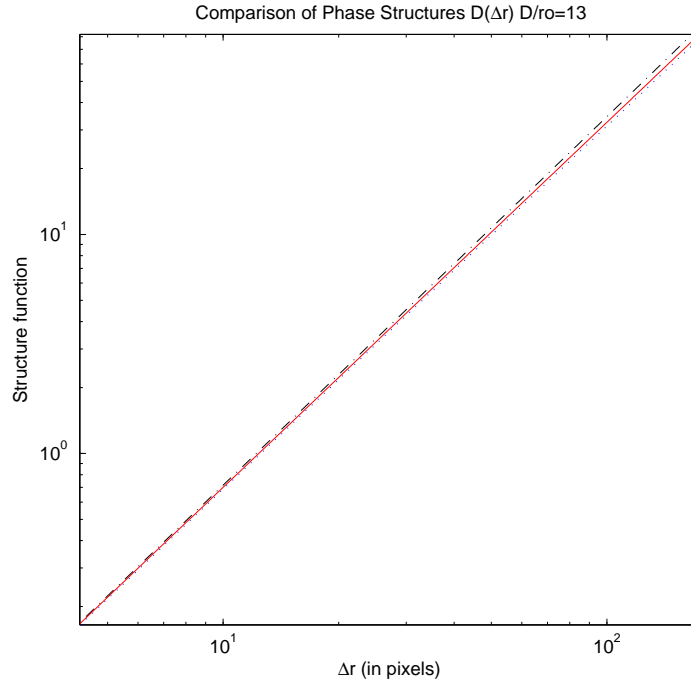


Fig. 6.3: Comparison of numerical horizontal (dash-dotted), numerical vertical (dotted) and theoretical (solid) phase structure function in loglog plot.  $\Delta r$  is in pixel spacing.

transform of two functions of a convolution and taking the inverse Fourier transform of the product. The function transfer of the turbulence,  $P_h(\mathbf{f})$  is defined, taking the Fourier transform of the impulse response  $p_h(\mathbf{r})$ .

$$P_h(\boldsymbol{\rho}) = e^{-i\pi\lambda h\mathbf{f}^2}, \quad (6.6)$$

$$\Psi_0(\mathbf{r}) = \mathcal{F}^{-1}[\mathcal{F}\{\Psi_h(\mathbf{r})\}.P_h(\mathbf{f})] \quad (6.7)$$

### 6.2.1 Sampling

For numerical simulation some sampling issues have to be met. They concern the sampling of phase of the phase screen, of the process of propagation from the phase screen to the observing plane, and the sampling of the scintillation pattern.

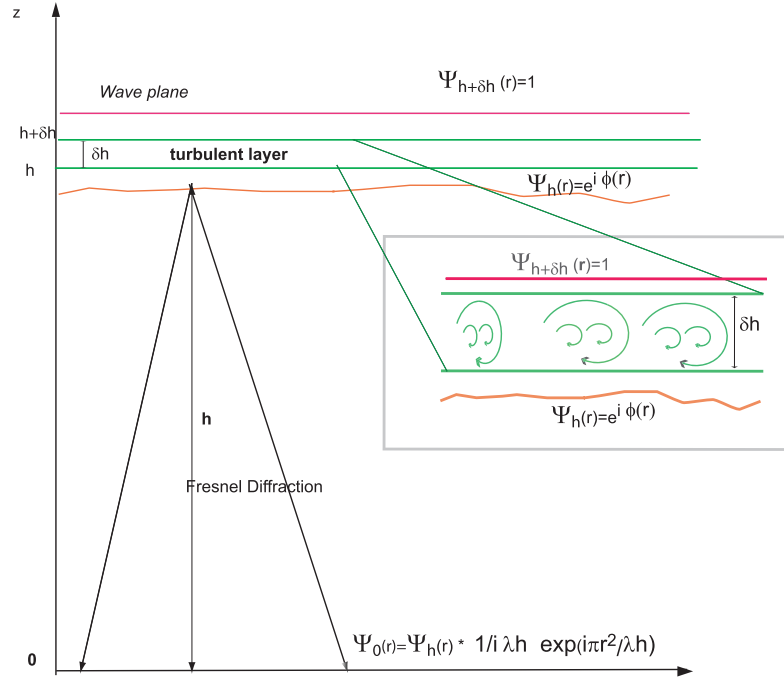


Fig. 6.4: Propagation through one turbulent layer.

### 6.2.1.1 Phase

The first sampling issue is that for the Kolmogorov phase screen to be well sampled, neighbouring pixels have to be separated by less than  $\pi$  radians.

$$\phi(\mathbf{r}) - \phi(\mathbf{r} + \Delta\mathbf{r}) \leq \pi \quad (6.8)$$

Using the statistical theoretical covariance of the phase (Eq.(6.2)) obtained from Kolmogorov theory

$$\langle [\phi(r) - \phi(r + \Delta r)]^2 \rangle = 6.88 \left( \frac{\Delta r}{r_0} \right)^{\frac{5}{3}} \leq \pi^2 \quad (6.9)$$

This give a phase sampling limit

$$\Delta\mathbf{r} \leq 1.2417 r_0 \quad (6.10)$$

Simulating a telescope of diameter  $D=25$  cm aperture with  $N \times N=32 \times 32$  or  $64 \times 64$  pixels, the maximum sampling is  $\frac{D}{32} \sim 8$  mm. This is smaller than the requirement of Eq.(6.10); for a typical  $r_0$  of 10cm we have  $\Delta\mathbf{r} \sim 0.08 r_0$

### 6.2.1.2 Fresnel propagation

Using the same argument, the variation of the argument of the transfer function of the atmosphere (Eq.(6.6)) must be less than  $\pi$ .

$$\pi \mathbf{f}^2 \Delta h \lambda \leq \pi \quad (6.11)$$

This gives the maximum propagation distance

$$h \leq \frac{4D^2}{\lambda(2N - 1)} \quad (6.12)$$

This gives for a diameter  $D=25$  cm, a number of pixels  $N=64$  and a wavelength  $\lambda=550$  nm, a maximum distance of 3579 m. However starting with a bigger size screen, keeping the same sampling  $\Delta \mathbf{r}$ , a screen of  $4 \times D= 1\text{m}$  with  $4 \times 64 = 256$  pixels allows a limit of 14 km. This permits us to make simulation with layers located at least 10 km distant from the ground.

### 6.2.1.3 Scintillation

Another sampling issue concerns the scintillation pattern. The sampling has to be fine enough to sample the size of the scintillation that is of the order of the first Fresnel zone. It has to be less than half of the smallest size of the irradiance fluctuation

$$\Delta \mathbf{r} \leq \frac{\sqrt{\lambda z}}{2} \quad (6.13)$$

For a range from 0 to 20 km, the typical size of the scintillation varies between 2 and 12 cm. This gives a higher sampling of  $\Delta \mathbf{r} \leq 1$  cm still respected for  $\Delta \mathbf{r} = \frac{0.25}{32} \sim 8$  mm

## 6.2.2 Edge effect

Edge effects are a problem of the simulations when we go into Fourier space to do the convolution product. As explained above, a bigger phase screen limits the edge effect. We always start with a screen size at least 4 times bigger. In addition, an apodising window can be used directly, in the direct space, on the incoming wave before Fresnel transform[2]. We use a Gaussian window to smooth the transfer function of the atmosphere in the Fourier space[44] which corresponds to another convolution of the wavefront with a Gaussian. A windowing to smooth the edges to

attenuate the pixel blurring in the resulting field after propagation. Starting with a big screen prevents edge effects from affecting the part of interest, and the window prevent the effect to propagate in the region of interest. In practice edge effects do not corrupt the region of interest and the Gaussian window is to avoid propagation of those effects.

$$w(\mathbf{r}) = \frac{1}{2\pi\sigma^2} \exp\left(-\frac{\mathbf{r}^2}{2\sigma^2}\right) \quad (6.14)$$

To simulate the different defocussing planes we propagate until the pupil plane then back propagate or forward propagate to obtain the different scintillation images.

Mainly simulations have been made for a  $64 \times 64$  pixels screen size, although the inversion has been applied on real data for a 32 pixel autocorrelation slice. The results are checked to correspond to the theoretical autocorrelation defined in Eq.(3.58).

Fig. 6.5, Fig. 6.6 and Fig. 6.7 show simulations with  $64 \times 64$  pixels of scintillation pattern, normalised autocorrelation and radial cut, for a layer located at 10 km with a value of  $r_o$  of 40 cm realised with 2000 frames. The different altitude conjugations are +5 km, +2.5km, 0km, -2.5km and -5km.

Fig. 6.5 displays simulated average intensities for the 5 measurement planes. From Fig. 6.5a to Fig. 6.5e we can see that the scintillation pattern gets bigger. The measurement plane is going further from the layer, so the scintillation develops creating bigger patterns.

The normalised autocorrelations are presented in Fig. 6.6. The isotropy of the autocorrelation is visible in the middle and a bit less on the edges but the values of the autocorrelation further from the centre get closer to zero.

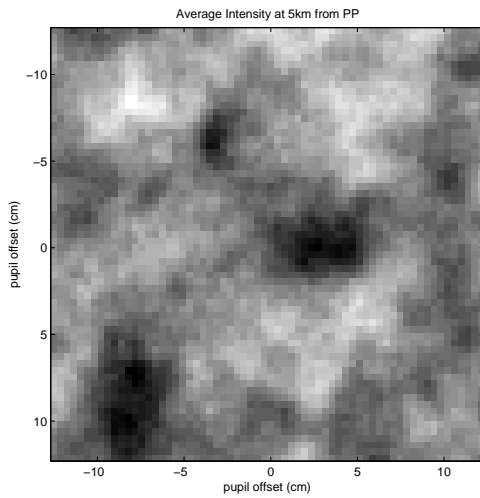
Fig. 6.7 shows the normalised averaged simulated autocorrelation radial cuts compared to the theoretical function. The 5 figures show a good agreement of the simulations with the theory.

### 6.2.3 Modelling diffraction effect

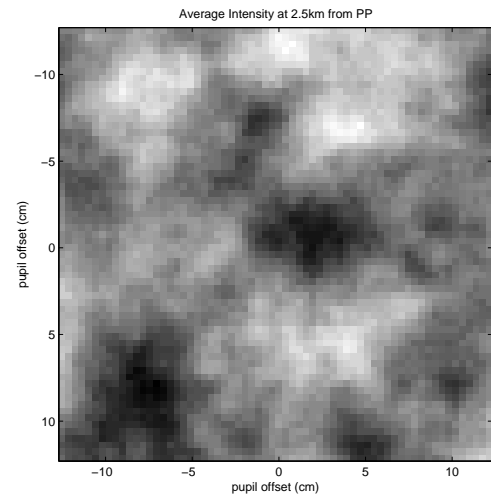
The blurring effect of the reimaging system can be neglected in the simulations but including the effect of diffraction for big defocussing distance, requires the development of the theory and a full expression of the system that has not been

---

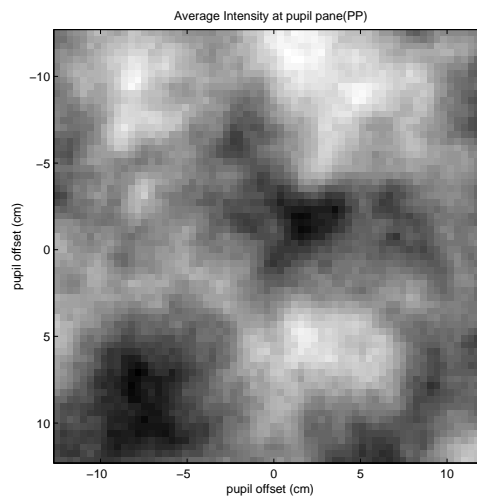
realised yet. Thus, the simulation does not account of the pupil propagation for extra propagation in defocus mode.



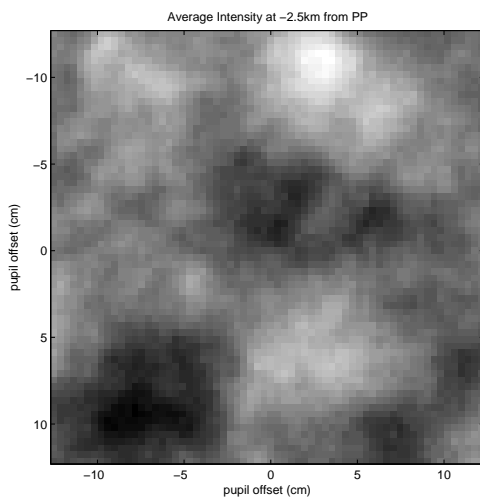
(a) Simulated intensity for pupil conjugation at +5km.



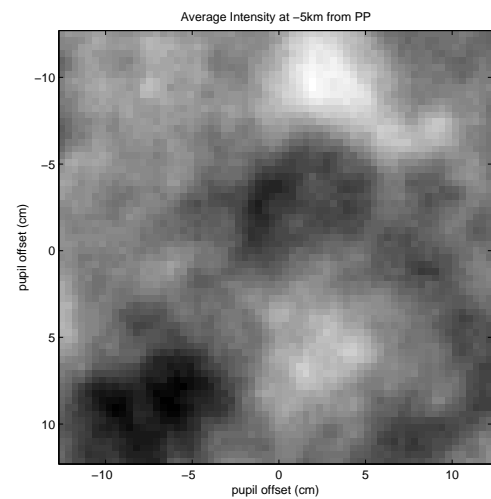
(b) Simulated intensity for pupil conjugation at +2.5km.



(c) Simulated intensity for pupil conjugation at the pupil.

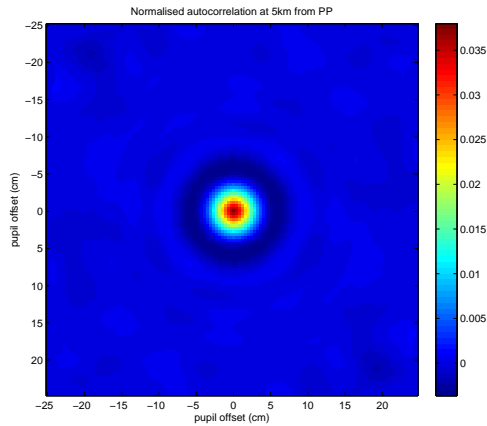


(d) Simulated intensity for pupil conjugation at -2.5km.

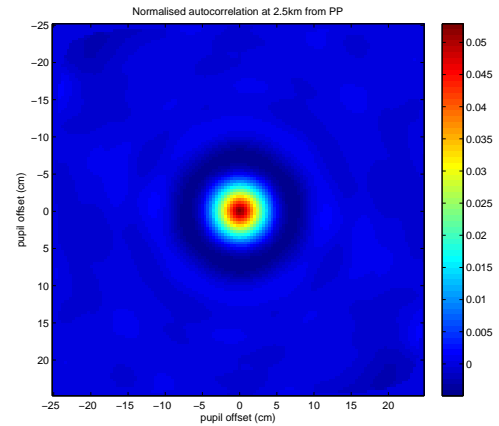


(e) Simulated intensity for pupil conjugation at -5km.

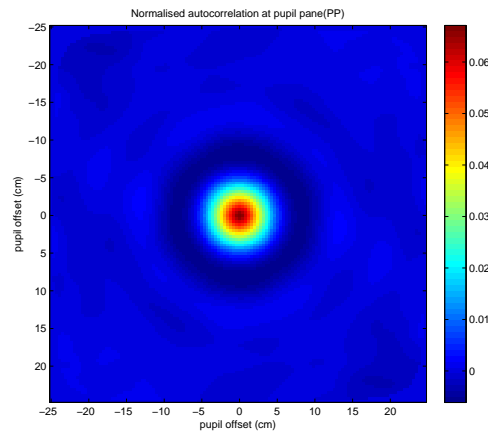
Fig. 6.5: Simulated scintillation patterns for 5 five different conjugation planes for a layer at 10 km with a  $r_0$  of 40 cm over 2000 frames.



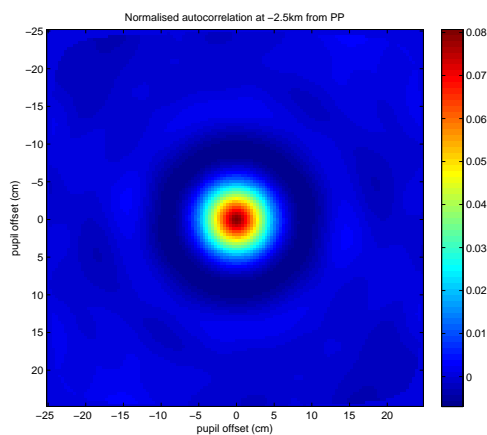
(a) Simulated 2 dimensional normalised autocorrelation for pupil conjugation at +5km.



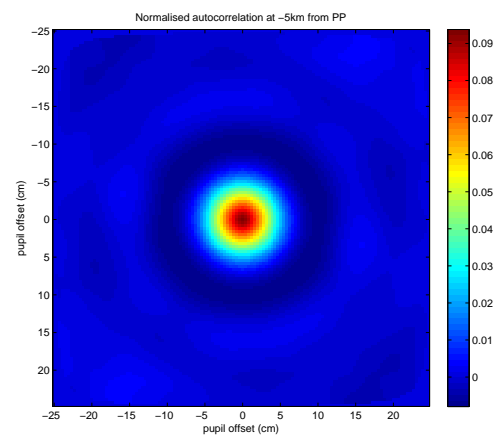
(b) Simulated 2 dimensional normalised autocorrelation for pupil conjugation at +2.5km.



(c) Simulated 2 dimensional normalised autocorrelation for pupil conjugation at pupil plane.



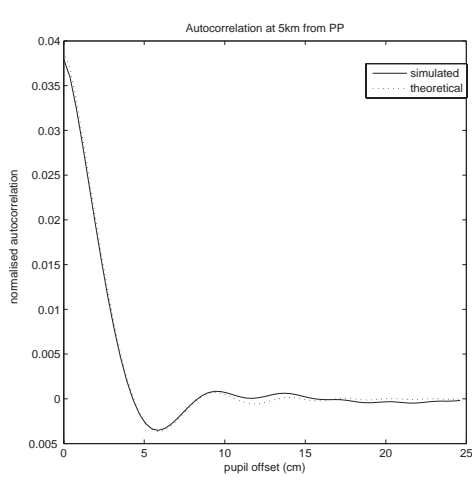
(d) Simulated 2 dimensional normalised autocorrelation for pupil conjugation at -2.5km.



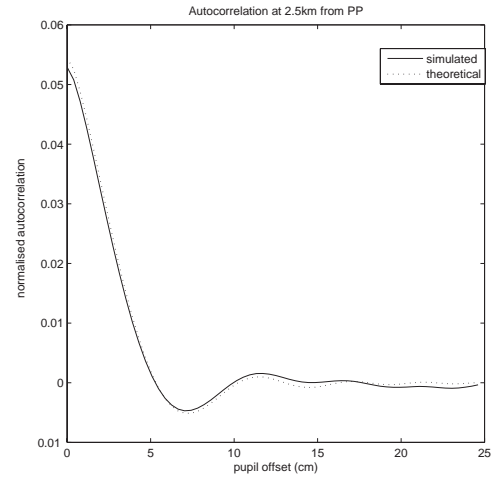
(e) Simulated 2 dimensional normalised autocorrelation for pupil conjugation at -5km.

Fig. 6.6: Simulated 2 dimensional normalised autocorrelation for 5 five different conjugation planes for a layer at 10 km with a  $r_0$  of 40 cm over 2000 frames.

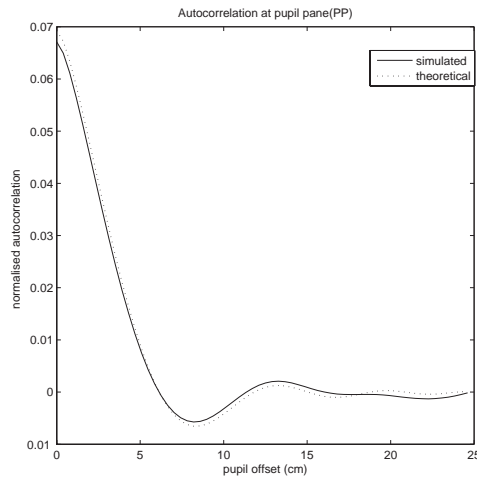




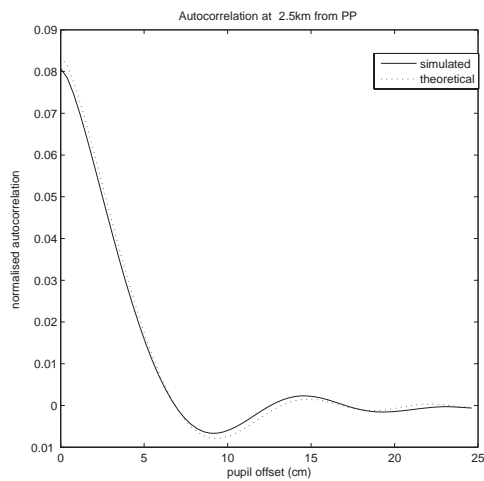
(a) Simulated average autocorrelation cuts for pupil conjugation at +5km.



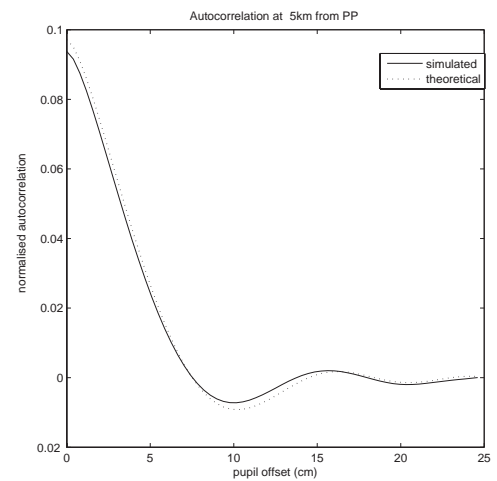
(b) Simulated average autocorrelation cuts for pupil conjugation at +2.5km.



(c) Simulated average autocorrelation cuts for pupil conjugation at the pupil plane.



(d) Simulated average autocorrelation cuts for pupil conjugation at -2.5km.



(e) Simulated average autocorrelation cuts for pupil conjugation at -5km.

Fig. 6.7: Simulated autocorrelation cuts for 5 five different conjugation planes for a layer at 10 km with a  $r_0$  of 40 cm over 2000 frames.

---

# Chapter 7

## Results

---

This chapter presents results obtained from the simulations and from data obtained during a campaign in October 2005 at La Palma. These results demonstrate the feasibility of the technique.

### 7.1 Results from simulation

For a  $\pm 2$  km defocus, diffraction effects are not so significant (see Figure 7.1). Retrieved profiles for different signal to noise ratio (SNR), with 5 observing planes located at +2,+1,0,-1,-2 km from the telescope pupil, with 1 kilometre height resolution have been simulated. Effects of diffraction appear to be significant when defocussing to a larger distance above the telescope as can be seen in Figure 7.2, where the distance is 5.8 km.

As indicated in section 5.1 the impact of the instrument's diffraction effects associated with the telescope pupil are not strongly in evidence for target heights below 2 km. As an initial validation of the inversion algorithm and the capability of the instrument to retrieve useful data giving the target height constraints simulations were performed to establish the system ability to locate predefined turbulent layers. In this study the approach was tested using the theoretical autocovariance responses produced for an atmosphere possessing two distinct layers, one at 1km and the other at 10km. These were chosen to have an integrated  $C_n^2(h)\delta h$  for each layer of  $8.34 \times 10^{-14} \text{m}^{\frac{1}{3}}$ . Given a wavelength of 550nm each layer has a corresponding  $r_0$  of 40 cm, with the resulting  $r_0$  for the wavefront after passing through both turbulent layers of 26.4 cm. To build up the data set defined in Eq.(5.10) the autocovariance response for the layers were modelled for 5 observing planes located at

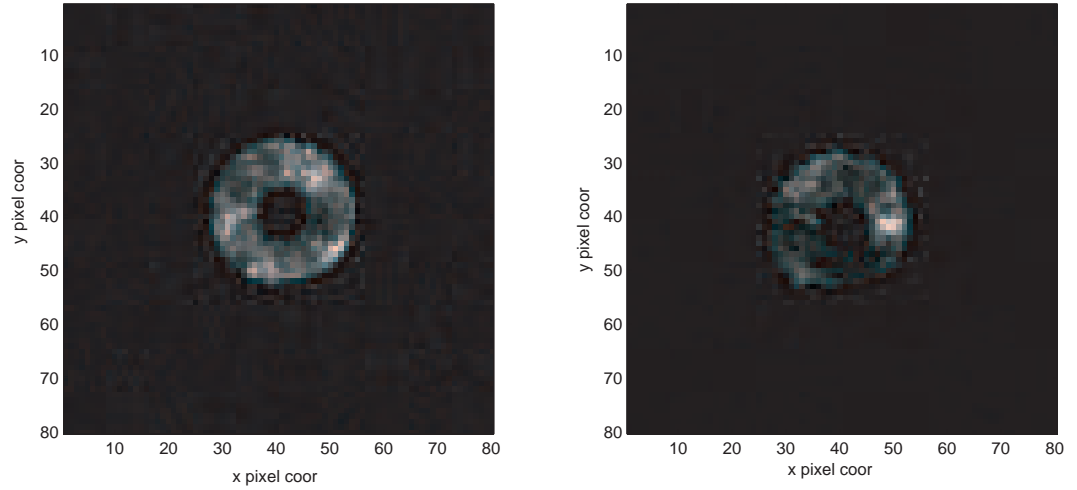


Fig. 7.1: SCIDAR data frames of Capella at pupil plane (left) and defocused to 2km (right).

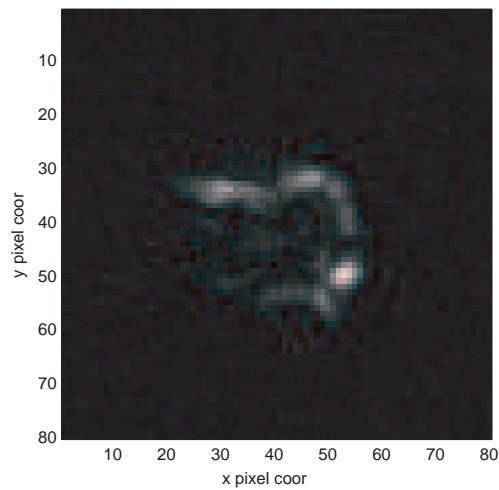


Fig. 7.2: SCIDAR data frame of Capella with measurement plane conjugated at 5.8km above the telescope aperture.

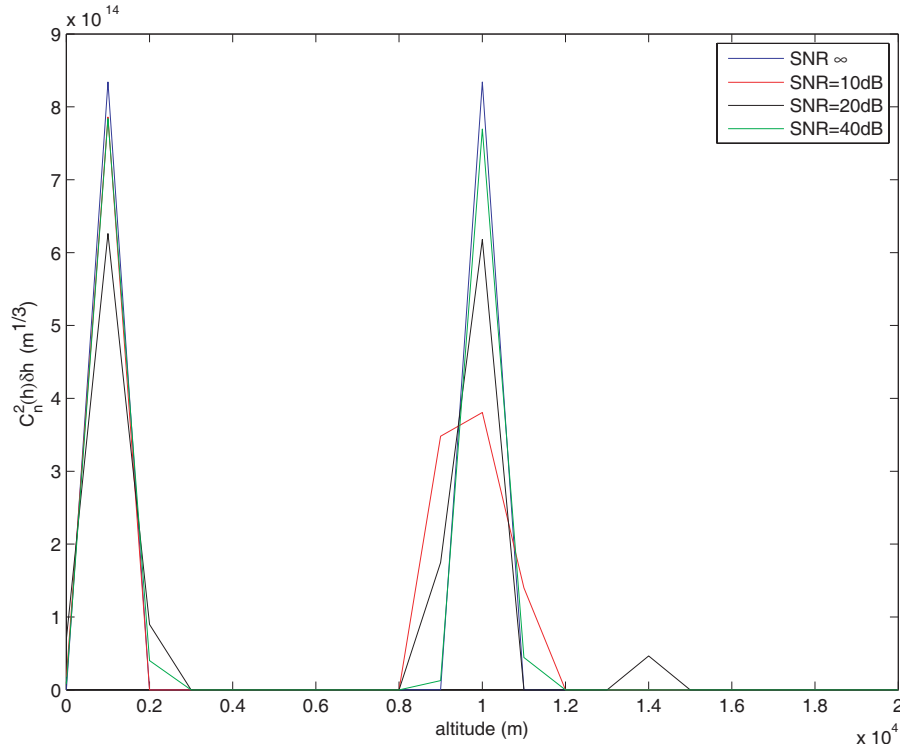


Fig. 7.3: Estimated  $C_n^2(h)$  profiles with an altitude resolution of 1 km for 4 different noise level. SNR=10dB (red), SNR=20dB (black), SNR=40dB (green) and noise free (blue). The ideal case is 2 layers at 1km and 10km simulated with  $C_n^2(h)\delta h = 8.34 \times 10^{-14} \text{m}^{\frac{1}{3}}$  for each.

+2, +1, 0, -1, -2 km from the telescope pupil. The primary interest in the study was to understand the sensitivity of the inversion algorithm to system noise. With this in mind the process of simulation and signal inversion was repeated for different background noise levels in the autocorrelation signal.

The retrieved profiles are shown in Fig. 7.3. The signal-to-noise ratios are expressed in terms of the average signal level in the “measured” autocorrelation to the *rms* white Gaussian noise: in terms of the peak of the autocorrelation, an SNR of 10dB is equivalent to an rms noise of approximately 5% of the peak value Fig. 7.5. Different values of noise are added Fig. 7.5. The retrieved profiles show excellent agreement with the initially assumed values, and the retrieved  $r_0$  values were all within 3%.

The results obtained vary in the value of the refractive index fluctuation of the

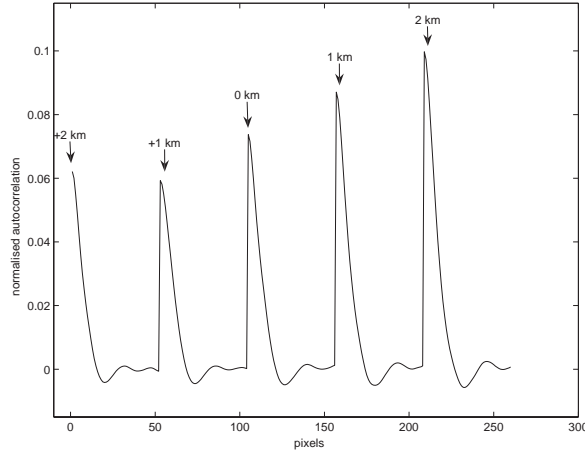


Fig. 7.4: Simulated autocorrelations data for 5 measurement planes at -2km,-1km,0,+1km,+2km, produced by two layers located at 20km and 1km.

layers. For small signal to noise ratios the inversion algorithm is unstable and gives additional strong layers apart from the two layers at 1 and 10 km. Other layers can be present in the retrieved profiles for a high SNR but with a much smaller weight compared to the value of the two main layers. More regularisation is needed for high SNR and the width of the peak in the  $C_n^2(h)$  estimate increases and the height falls, with the overall area under the profile remaining relatively changeless. The range of the regularisation parameter  $\gamma$  ranges between  $10^{-6}$  and  $10^{-3}$ .

## 7.2 Results from the campaign at La Palma

A measurement campaign lasting for a week in November 2005 was carried out at the Observatorio del Roque de los Muchachos, on La Palma island. The equipment was installed on the JKT (Jacobus Kapteyn Telescope). Three nights were actually usable. The alignment and the weather conditions made it difficult to observe on the other nights. Different stars with magnitudes from 0 to 3 were observed, using sequences of 2000 frames per defocus value. Seven defocus planes used were from 2.4km, 1.2km, and 0.6km below telescope pupil, with the corresponding planes above the pupil 0.6km, 1.2km and 2.4km, and the plane pupil. The camera exposure in all the scintillation data taken was 1ms, with binning of 2 ( $64 \times 64$  pixels) and 4 ( $32 \times 32$  pixels) for each star data set corresponding to spatial averaging of  $3.9 \times 3.9$

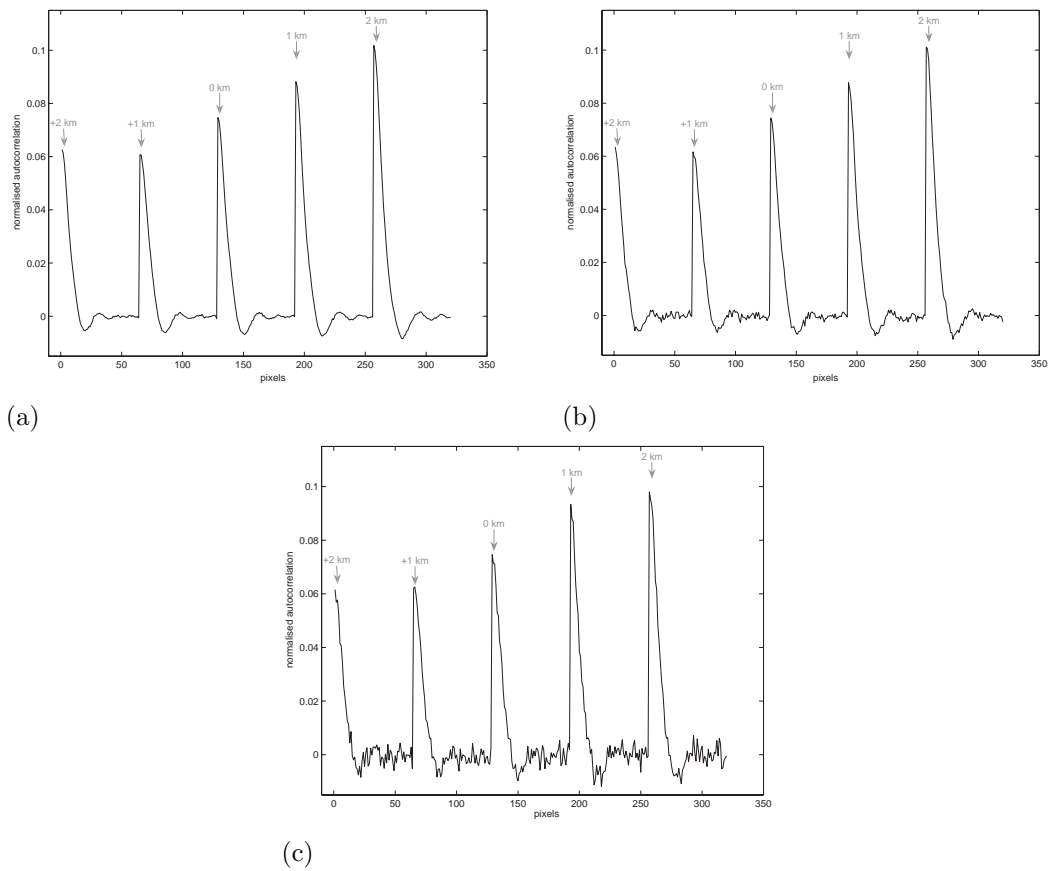


Fig. 7.5: Simulated autocorrelations single star SCIDAR data with different Gaussian noise values. (a) corresponds to a SNR of 60dB, (b) corresponds to a SNR of 40dB, (c) corresponds to a SNR of 20dB.

mm and  $7.8 \times 7.8$  mm respectively in the pupil. The target star was also taken to be as close as possible of the zenith.

### 7.2.1 Reduced autocovariances

The whole average autocorrelation is not usable due to noise and re-centring as shown in Fig. 7.6. The useful portion of the autocorrelation is on average 180 mm instead of the 250 mm for the full pupil. In addition perfect collimation was hard to achieve, which creates scintillation patterns with different size for different pupil conjugation within the same set.

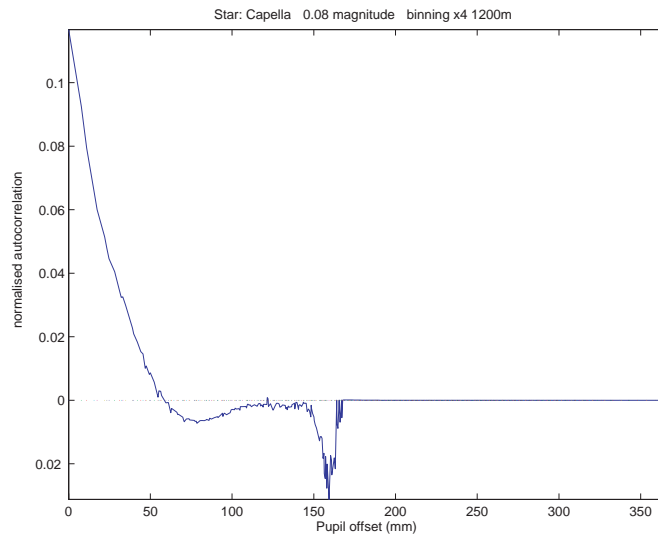


Fig. 7.6: Average autocorrelation for the bright star Capella ( $m_v \simeq 0.08$ ).

Autocorrelations for a magnitude 3.27 star with a binning $\times 4$  show a peak at the origin (Fig. 7.7) associated with the read noise. The average photon flux for this star and this binning is around 100 photons per pixel. The read noise becomes dominant at the origin of the autocorrelation.

### 7.2.2 $C_n^2(h)$ profile estimates

Retrieval of the refractive index fluctuation profile is made for an altitude resolution of 1km. Only the five central planes of measurement are kept in order to stay with the range where the effect of diffraction is minimised as discussed in section

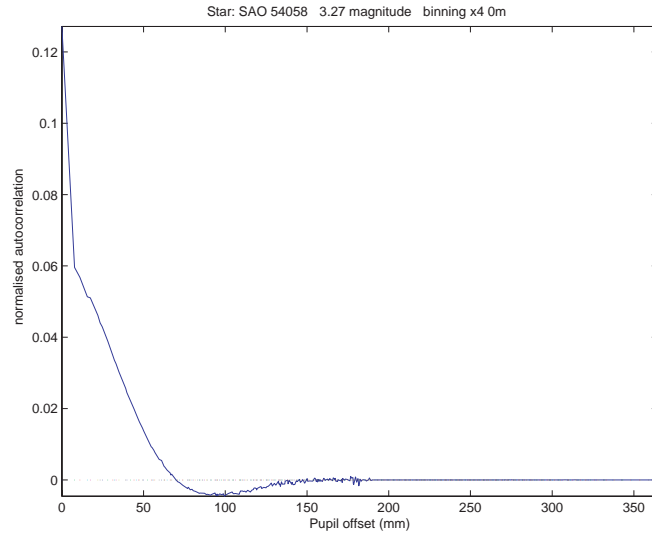


Fig. 7.7: Average autocorrelation for  $\delta$  Andromeda (magnitude 3.27). Note the peak at the origin.

5.1. The regularisation parameter  $\gamma$  can be found automatically using the L-curve method, giving a range of values determined to be around the standard deviation of the autocorrelation functions, for magnitude up to 2. Parameter values were experimentally tried until an acceptable solution to check the consistency of the method. In the case of a magnitude of about 3 the L-curve technique fails. This might be due to the implementation of the program for the level of noise. The value of the parameter has been found by trials. Examples of retrieved  $C_n^2(h)$  profiles are shown in Fig. 7.8a, Fig. 7.8b, Fig. 7.9 and Fig. 7.10.

### 7.2.3 Estimation of the error

To check the accuracy the estimated value of the seeing  $\beta$  (Eq.(3.18)) was calculated from the estimates  $\hat{C}_n^2(h)$  profiles, shown in Figs. 7.8a, 7.8b, 7.9 and 7.10, and checked against the values of the seeing given by the seeing monitor of the Isaac Newton Group of Telescopes (RoboDIMM) archives[1]. In addition, following Klückers et al. [49] we define the error on the retrieved autocovariance data as

$$\varepsilon_B = \sqrt{\frac{\langle (B - \hat{B})^2 \rangle}{\langle B^2 \rangle}}, \quad (7.1)$$



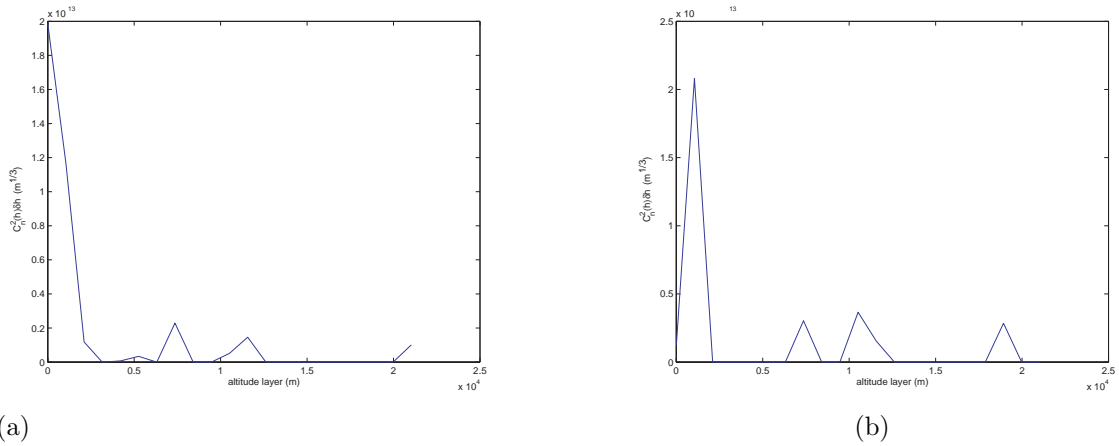


Fig. 7.8: Estimated  $C_n^2(h)$  profile using Capella (magnitude 0.08 star) for a binning $\times 2$ . (b) was taken ten minutes later. Four layers at 1km,  $\sim 8$  km,  $\sim 11$  km and  $\sim 20$  km are present in both profiles, as well as one around 20 km. In the first run (a) shows an extra layer at 0km. The contribution of the layer located at  $\sim 11$  km in (a) is half less important than in (b).

where  $\hat{B}$  is the autocovariance calculated from the profile estimates as  $\hat{B} = KC_n^2(h)$ . Fig. 7.11a, Fig. 7.11b, Fig. 7.12 and Fig. 7.13 show comparison between the data retrieved from the  $\hat{C}_n^2(h)$  estimates and real data and the error, and the values of the retrieved seeing with the one from RoboDIMM.

The value of the estimated seeing is relatively close to the one given by RoboDIMM.

The values of the error on the autocovariances estimate,  $\varepsilon_B$  are around 20% (c.f. Fig. 7.11, Fig. 7.12, Fig. 7.13). It is good considering full autocovariance functions are not used, and the presence of the peak due to read out noise at the origin for one star. Moreover the collimation of the instrument was not perfect giving different scintillation patterns with different scales. Even for a star of magnitude 3.27 ( $\delta$  Andromeda) the error is low (Fig. 7.13).

The 4 sets of turbulence profiles show similar general shape. The distribution of the layers appears discrete, composed of three or four dominant layers. The main contribution by far in the profiles is the closest layer above the telescope aperture. This layer corresponds to the boundary layer as expected. The other turbulent

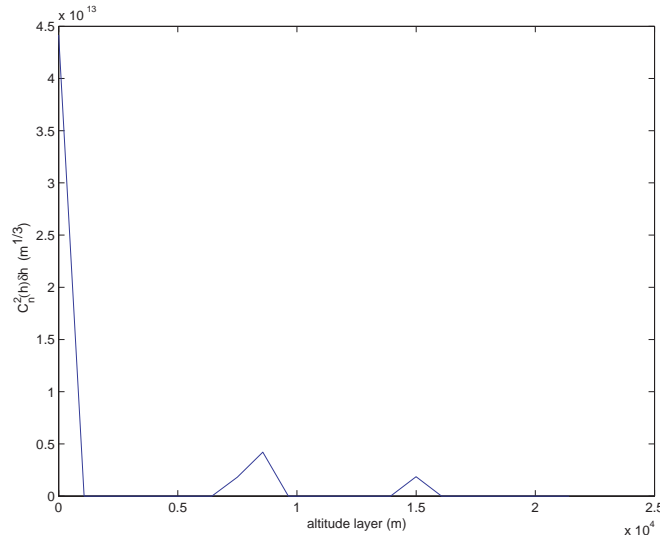


Fig. 7.9: Estimated  $C_n^2(h)$  profile using Capella (magnitude 0.08 star) for a binning $\times 4$ . Three main layers are present; a strong one at 0 km and two less important at 8 km and 15 km.

layers are located higher in the atmosphere, with two layers located around 10 km. Fig. 7.8a and Fig. 7.8b show two turbulence profiles obtained with few minutes delay. They both have a turbulent layer at 2 km. In the second set the layer at the ground do not appear any more and is only located at 1 km. These 3 other layers in Fig. 7.8b are still present but their refractive index is higher. These changes reflect the fluctuations of the turbulence strength in the atmosphere and in intensity that is expected to be bigger according to the experimental autocorrelation that have higher values too as seen in Fig. 7.11a and Fig. 7.11b. The set of experimental autocorrelations for Capella with a binning by 4, Fig. 7.12, shows a value at the origin for the autocorrelation corresponding to an altitude conjugation of + 1.2 km (first autocorrelation) that seems to a bit high compare to the other ones. Considering that the scintillation index for the lowest plane below the telescope represents the contribution due to all the layers, the scintillation index should be the bigger one, and the scintillation index in a plane above the telescope should be lower within the noise fluctuations. This particular autocorrelation revealed to have more bad frames and is noisier than the rest of the set of autocorrelations. The profile for  $\delta$  Andromeda presents high value wider layers (Fig. 7.10). The noise is more impor-

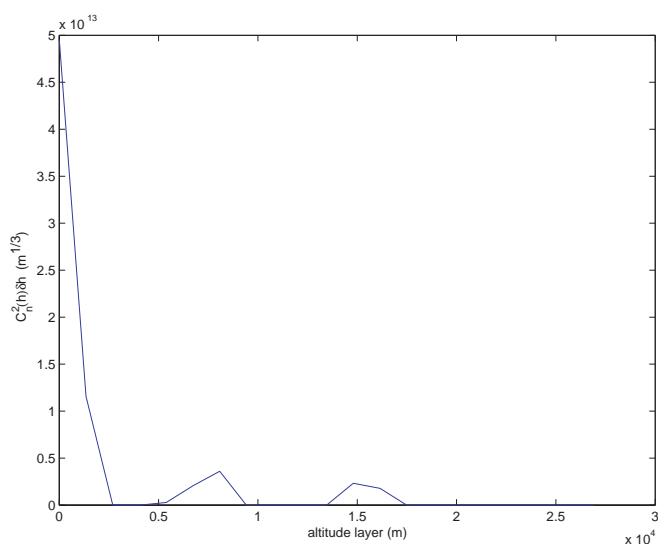


Fig. 7.10: Estimated  $C_n^2(h)$  profile using  $\delta$  Andromeda (magnitude 3.27 star) for a binning $\times 4$ . Mainly four layers are present; a very strong one at 0 km, one 1 km and two less important at 8 km and 15 km.

tant because the star is fainter, then more regularisation is needed to find a solution creating broader solutions with lower values of the turbulence strength. However, the presence of the peak at the origin of each autocorrelation (Fig. 7.13) tend more likely to increase the strength of the turbulence in the estimate.

The seeing retrieved from the profiles are always bigger than the seeing value at the site of measurement. That means that the intensity of the turbulence layers should be in reality smaller (Eq.(3.16) and Eq.(3.18)) and are overestimated, and then that the structure constant of the refractive index should be smaller in the profiles.

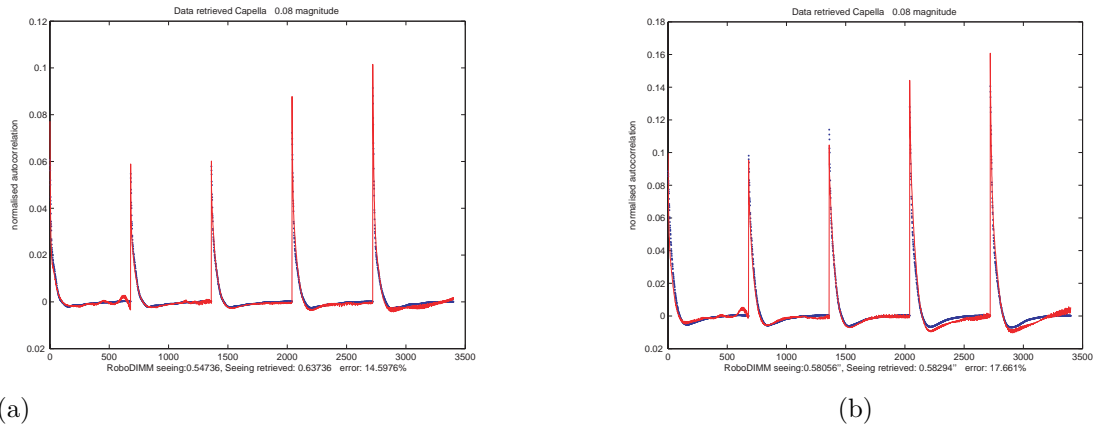


Fig. 7.11: Estimation of the error for Capella data binning by 2 for two consecutive runs. The experimental autocovariance is represented by a solid red line and the retrieved autocovariance in blue dots.

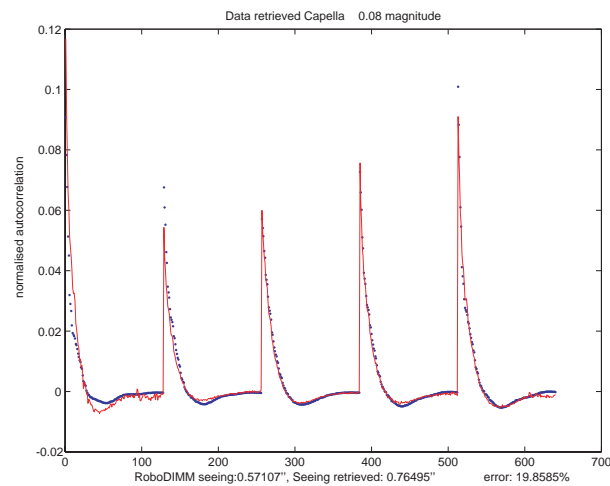


Fig. 7.12: Estimation of the error for Capella data with binning by 4. The experimental autocovariance is represented by a solid red line and the retrieved autocovariance in blue dots.

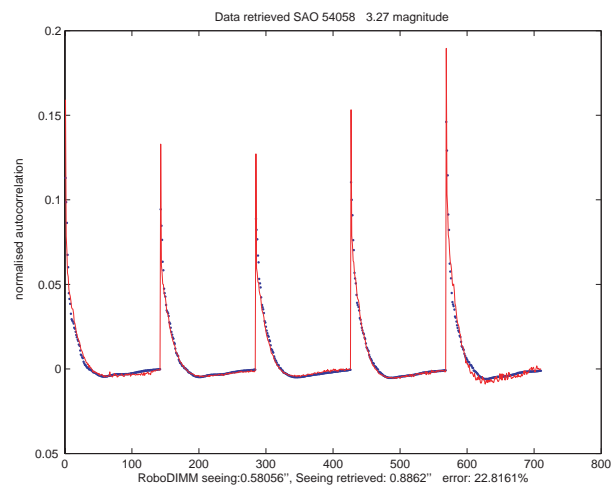


Fig. 7.13: Estimation of the error for  $\delta$  Andromeda data with binning by 4. The experimental autocovariance is represented by a solid red line and the retrieved autocovariance in blue dots.

---

# Chapter 8

## Conclusion and future work

---

### 8.1 Summary

A remote sensing technique that uses an analysis of the scintillation to obtain altitude turbulence strength profiles was presented. The single star SCIDAR instrument is a 25-cm telescope with an imaging system at its back designed to record a sequence of pupil images of a single star at five different defocussing height.

Simulations using Fresnel diffraction of wave propagation through atmospheric turbulence were made to simulate scintillation patterns of the instrument. Those simulations were used to test a least-square method using Tikhonov regularisation method to retrieve the turbulence profiles from SCIDAR data. The results obtained with this inversion method on simulations gave satisfactory results.

Structure constant refractive index fluctuation profiles were obtained from experimental data gathered from an observing site. The inversion technique provided encouraging results. We have shown that we can obtain profiles using scintillation produced by a single star for bright stars of magnitude greater than three.

Better star tracking would be useful and a better re-centring technique would allow to make full use of the autocorrelation function. Collimation should be improved to maintain a constant pupil width for different conjugate pupil heights. The algorithm can be improved especially to determine the optimum regularisation parameter  $\gamma$  for an automatic approach. For bright stars the value can be usually found automatically but it shows real weakness for dimmer stars.

A bigger defocussing distance would allow a higher conjugation height to help the inversion, that can be done with a, still portable, 40-cm telescope. With a 40-cm telescope the height of conjugation can be doubled improving the inversion. It would increase as well the signal to noise ratio.

## 8.2 Future work

The greatest single improvement that could be made to the method of multi-generalised single star SCIDAR is to record the data from the various defocus planes simultaneously, rather than sequentially as in this Thesis. This would reduce the variability inherent in the sequential acquisition method, and might allow a smaller number of defocus positions to be used. The disadvantage of doing this is that, since the optical intensity is now divided between several (e.g. 4 or 5) channels, the photon noise for each data set increases. This could be partially offset by using a camera with a higher quantum efficiency, such as a thinned CCD camera.

The value of the regularisation parameter is a key factor in determining the quality of the estimated  $C_n^2(h)$  profile and finding an improved and more robust method for estimating this parameter is desirable. This probably has to be investigated by carrying out more simulations.

In the present study, we considered, but in the end ignored, telescope diffraction effects in the defocus data planes. This had the effect of limiting the maximum defocus we could use. Diffraction effects could be incorporated analytically into the theory and an initial study of this was carried out with Prof H H Barrett during his stay in our group. The problem with this is that the system operator, composed by the telescope aperture and the overall optical system (telescope plus reimaging optics treated as a thin lens), becomes non-isoplanatic and the final expression becomes very complicated. However, if the single star SCIDAR method is to be implemented, this should be pursued.

Finally, a critical comparison needs to be made between multi-generalised single star

---

SCIDAR as described in this Thesis, and competing methods such as the MASS and, in particular, SLODAR. SLODAR uses Shack-Hartmann wavefront sensing, and astronomers are very familiar with this technique. Another advantage is that the inversion procedure for SLODAR appears to be much simpler than the techniques described here. There may also be other advantages, for example it may have some fundamental advantage, but that is not clear. A detailed comparison of multi-generalised single star SCIDAR and SLODAR should be carried out.



---

# Appendix A

## Hilbert Spaces

---

In this thesis, the norm is taken to be the  $\mathbb{L}_2$  norm. The vector space is a Hilbert space. It is the case, for the definition of Fourier transform and then the following functions are in an Hilbert space. Hilbert spaces is defined in this appendix and the  $\mathbb{L}_2$  norm.

### A.1 Vectors

Vectors can be defined simply as objects that can be added to each other and multiplied by numbers[10]. It is easily seen taking a 3D-vector  $\mathbf{f}$  with cartesian components  $(f_x, f_y, f_z)$  and a scalar  $\lambda$ . A set of  $N$ -dimensional vectors with each a set of  $N$  ordered numbers (or  $N$ -tuple) coordinates  $(f_1, \dots, f_N)$  is a *linear vector space*. Examples of linear vector space is  $\mathbb{R}^3$ , where each vector is a triplet of real numbers. The  $\mathbb{C}^3$  space is similar than  $\mathbb{R}^3$  but with complex numbers.

### A.2 Hilbert Space

An Hilbert space is a normed *Banach space* equipped with a scalar product (inner product). A Banach space is defined as a complete normed linear space. A Hilbert space is a generalization of an Euclidean space with infinite-dimension.

- The distance  $d(\mathbf{f}_1, \mathbf{f}_2)$  is defined from the norm  $\|\mathbf{f}_1 - \mathbf{f}_2\|$  as  $d(\mathbf{f}_1, \mathbf{f}_2) = \|\mathbf{f}_1 - \mathbf{f}_2\|$ .
- The space is complete meaning that the norm of every *Cauchy sequence* has a limit.

- The norm is itself defined from the scalar product,  $(\mathbf{f}_1, \mathbf{f}_2)$  as  $\|\mathbf{f}\| = \sqrt{(\mathbf{f}, \mathbf{f})}$ .

### A.2.1 Distance And Norm

In an  $N$ -dimensional vector space the metric or distance of two vectors  $\mathbf{f}_1$  and  $\mathbf{f}_2$ , denoted  $d(\mathbf{f}_1, \mathbf{f}_2)$  satisfies the following properties

- (a)  $d(\mathbf{f}_1, \mathbf{f}_2) = d(\mathbf{f}_2, \mathbf{f}_1)$
- (b)  $d(\mathbf{f}_1, \mathbf{f}_2) \geq 0$ ,  $d(\mathbf{f}_1, \mathbf{f}_2) = 0$  if and only if  $\mathbf{f}_1 = \mathbf{f}_2$
- (c)  $d(\mathbf{f}_1, \mathbf{f}_2) \leq d(\mathbf{f}_1, \mathbf{f}_3) + d(\mathbf{f}_3, \mathbf{f}_2)$  for any  $\mathbf{f}_3$  (triangle inequality)

In  $\mathbb{R}^3$ , the distance is commonly defined by

$$d(\mathbf{f}_1, \mathbf{f}_2) = [(f_{1x} - f_{2x})^2 + (f_{1y} - f_{2y})^2 + (f_{1z} - f_{2z})^2] \quad (\text{A.1})$$

The notion of distance is closely related to notion of *norm*. In an  $N$ -dimensional vector space the *norm* of a vector  $\mathbf{f}$ , denoted  $\|\mathbf{f}\|$  has the properties

- (a)  $\|\mathbf{f}\| \geq 0$
- (b)  $\|\lambda \mathbf{f}\| = |\lambda| \cdot \|\mathbf{f}\|$ , with  $\lambda$  any real or complex number
- (c)  $\|\mathbf{f}_1 + \mathbf{f}_2\| \leq \|\mathbf{f}_1\| + \|\mathbf{f}_2\|$  In  $\mathbb{R}^N$  or  $\mathbb{C}^N$  we can define a particular norm

$$\|\mathbf{f}\|_p = \left[ \sum_{n=1}^N |f_n|^p \right]^{\frac{1}{p}}, \quad (\text{A.2})$$

called the  $\mathbb{L}_p$  norm. For  $p = 2$  we recognise the well known  $\mathbb{L}_2$  norm.

$$\|\mathbf{f}\|_2 = \left[ \sum_{n=1}^N |f_n|^2 \right]^{\frac{1}{2}} \quad (\mathbb{L}_2 \text{ norm}) \quad (\text{A.3})$$

A distance in a vector space can be defined as

$$d(\mathbf{f}_1, \mathbf{f}_2) = \|\mathbf{f}_1 - \mathbf{f}_2\| \quad (\text{A.4})$$

A vector space with Norm- $\mathbb{L}_2$  is an  $N$ -dimensional space, referred as Euclidean space and is denoted as  $\mathbb{E}^N$ . We should note that a functional is a mapping which associates a number (real or complex) to each vector, or function.

### A.2.2 Completeness

The notion of completeness of an Euclidean space is strictly related to the notion of convergence. The concept of convergence is linked to the concept of distance.

A sequence of vectors  $\mathbf{f}_j$  is said to be convergent to an element  $\mathbf{a}$  of the space if the limit of  $\mathbf{f}_j \rightarrow \mathbf{a}$  when  $j \rightarrow \infty$ . A *Cauchy sequence* is a sequence  $\mathbf{f}_j$  such that  $\|\mathbf{f}_j - \mathbf{f}_k\| \rightarrow 0$  when  $j, k \rightarrow \infty$ . A vector space is said to be complete when any Cauchy sequence is convergent to an element of the space. For example, the  $N$ -dimensional Euclidean space,  $\mathbb{E}^N$  is complete for any finite  $N$ . A *complete Euclidean space is a Hilbert space*. Another example of a complete metric space is the  $\mathbb{L}_p$ -space of  $p$ -integrable functions which is a complete metric space if  $p \geq 1$ .

### A.2.3 Scalar Products

So far we introduced the notions to define a Banach space, but the concept of scalar product has not been introduced. In  $\mathbb{R}^3$  the scalar product is simply defined as

$$(\mathbf{f}_1, \mathbf{f}_2) = \|\mathbf{f}_1\| \cdot \|\mathbf{f}_2\| \cos(\theta), \quad (\text{A.5})$$

where  $\theta$  is the angle between  $\mathbf{f}_1$  and  $\mathbf{f}_2$ . The scalar product gives from a function, or vectors a number, it is therefore a functional. A general scalar product is a complex valued functional. The scalar product or inner product in a general Hilbert space  $\mathbb{U}$  denoted  $(\mathbf{f}_1, \mathbf{f}_2)$ , sometimes  $(\mathbf{f}_1, \mathbf{f}_2)_{\mathbb{U}}$  if necessary, has the following properties

- (a)  $(\mathbf{f}_1, \mathbf{f}_1) \geq 0$ ,  $(\mathbf{f}_1, \mathbf{f}_1) = 0$  if and only if  $\mathbf{f}_1 = 0$  (zero element of  $\mathbb{U}$ )
- (b)  $(\mathbf{f}_1, \mathbf{f}_2) = (\mathbf{f}_2, \mathbf{f}_1)^*$
- (c)  $(\alpha\mathbf{f}_1, \mathbf{f}_2) = \alpha(\mathbf{f}_1, \mathbf{f}_2)$  for any complex number  $\alpha$
- (d)  $(\mathbf{f}_1 + \mathbf{f}_2, \mathbf{f}_3) = (\mathbf{f}_1, \mathbf{f}_3) + (\mathbf{f}_2, \mathbf{f}_3)$

Conditions (c) and (d), imply that the scalar product  $(\mathbf{f}_1, \mathbf{f}_2)$  is a linear functional of the first argument. From (b) and (c), we can derive that

$$(\mathbf{f}_1, \alpha\mathbf{f}_2) = \alpha^*(\mathbf{f}_1, \mathbf{f}_2). \quad (\text{A.6})$$

The norm of a Hilbert space is generated from a scalar product.

$$\|\mathbf{f}\| = \sqrt{(\mathbf{f}, \mathbf{f})}. \quad (\text{A.7})$$

### A.2.4 $\mathbb{L}_2$ spaces

On  $N$ -dimensional Euclidean space  $\mathbb{E}^N$ , the scalar product is defined as

$$(\mathbf{f}_1, \mathbf{f}_2) = \sum_{n=1}^N f_{1n}^* f_{2n} \quad (\text{A.8})$$

The Hilbert space  $\mathbb{L}_2(\alpha, \beta)$ , or  $\mathbb{L}_2$ , the space of complex-valued functions  $f(x)$  have the scalar product defined as

$$(\mathbf{f}_1, \mathbf{f}_2) = \int_{\alpha}^{\beta} dx f_1^*(x) f_2(x) \quad (\text{A.9})$$

The norm is defined by

$$\|\mathbf{f}\| = \sqrt{(\mathbf{f}, \mathbf{f})} = \left[ \int_{\alpha}^{\beta} |f^*(x)|^2 \right]^{\frac{1}{2}}. \quad (\text{A.10})$$

A function  $f(x)$  belongs to  $\mathbb{L}_2(\alpha, \beta)$ , if the integral in Eq.(A.10) exists.  $\mathbb{L}_2(\alpha, \beta)$  is the square-integrable function space, over the range  $(\alpha, \beta)$ . We can extend  $\mathbb{L}_2$  to  $\mathbb{L}_2(\mathbb{L}^q)$ , in which born of integration are  $(-\infty, \infty)$ , and the vector  $\mathbf{r}$  is a  $q$ D vector in  $\mathbb{R}^q$ .

$$\|\mathbf{f}\| = \left[ \int_{-\infty}^{\infty} d^q r |f(\mathbf{r})|^2 \right]^{\frac{1}{2}}. \quad (\text{A.11})$$

$$(\mathbf{f}_1, \mathbf{f}_2) = \int_{-\infty}^{\infty} d^q r f_1^*(\mathbf{r}) f_2(\mathbf{r}). \quad (\text{A.12})$$

# Bibliography

- [1] RoboDIMM Data Access. <http://www.ing.iac.es/ds/robodimm/>.
- [2] M. J. Adcock. *Simulation of Three Dimensional Propagation of Light Through Turbulent Media Applied to Adaptive Optics*. PhD thesis, Imperial College of Science, Technology and Medecine, London, UK, 1997.
- [3] C. W. Allen and A. N. Cox. *Allen's Astrophysical Quantities*. Springer, New York, 1999.
- [4] L. C. Andrews, R. L. Phillips, C. Y. Hopen, and M. A. Al Habash. Theory of optical scintillation. *J. Opt. Soc. Am. A*, 16(6):1417–1429, 1999.
- [5] R. Avila, J. Vernin, and S. Cuevas. Turbulence profiles with generalized scidar at San Pedro Mártir observatory and isoplanatism studies. *PASP*, 110:1106–1116, 1998.
- [6] R. Avila, J. Vernin, and E. Masciadri. Whole atmospheric-turbulence profiling with generalized scidar. *Appl. Opt.*, 36:7898–7905, 1997.
- [7] R. Avila, J. Vernin, and L. J. Sanchez. Atmospheric turbulence and wind profiles monitoring with generalized scidar. *Astron. Astrophys.*, 369:364–372, 2001.
- [8] M. Azouit and J. Vernin. Optical turbulence profiling with balloons relevant to astronomy and atmospheric physics. *PASP*, 117:536–543, May 2005.
- [9] M. Azouit, J. Vernin, R. Barletti, G. Ceppatelli, A. Righini, and N. Speroni. Remote sensing of atmospheric turbulence by means of a fast optical method - a comparison with simultaneous in situ measurements. *Journal of Applied Meteorology*, 19:834–838, 1980.

- 
- [10] H. H. Barrett and K. Myers. *Foundations of Image Science*. Wiley-Interscience, 2003.
- [11] R. R. Beland. Propagation through atmospheric optical turbulence. In *The Infrared and Electro-Optical Systems Handbook, 1993*, volume 2 Atmospheric Propagation of Radiation, chapter 2, pages 157–232. Cambridge University Press, Bellingham, Wash., f. g. smith edition, 1993.
- [12] M. Bertero and P. Boccacci. *Introduction to Inverse Problems in Imaging*. Institute of Physics IOP Publishing, 1998.
- [13] R. Bracewell. *The Fourier Transform and Its Applications*. McGraw-Hill, Third edition, 2000.
- [14] J. P. Braga. Numerical comparison between Tikhonov regularization and singular value decomposition methods using the  $l$  curve criterion. *Journal of Mathematical Chemistry*, 29(2):151–161, 2001.
- [15] J. L. Caccia, M. Azouit, and J. Vernin. Wind and  $C_N^2$  profiling by single-star scintillation analysis. *Appl. Opt.*, 26:1288–1294, 1987.
- [16] J. L. Caccia, J. Vernin, and M. Azouit. Structure function  $C_N^2$  profiling by two-color stellar scintillation with atmospheric dispersion. *Appl. Opt.*, 27:2229–2235, 1988.
- [17] D. Coburn, D. Garnier, and C. Dainty. Development and modelling of a single star SCIDAR system for profiling atmospheric turbulence. In *Laser and Optical Systems for Astronomy and Space-Based Instrumentation II, Proc. FiO and Laser Science.*, 2005.
- [18] D. Coburn, D. Garnier, and J. C. Dainty. Development of a Single Star SCIDAR system for profiling atmospheric turbulence. *Atmosphere knowledge and Adaptive Optics for 8 to 100 m telescopes, ESO Mini Workshop, Garching, October 2003*.
- [19] D. Coburn, D. Garnier, and J. C. Dainty. A single star SCIDAR system for profiling atmospheric turbulence. In *Optics in Atmospheric Propagation and Adaptive Systems VIII. Proc. SPIE, Vol. 5981:105-114*, 2005.

- 
- [20] J. M. Conan. Strategy for a better understanding of key atmospheric parameters. *Atmosphere knowledge and Adaptive Optics for 8 to 100 m telescopes, ESO Mini Workshop, Garching*, October 2003.
- [21] J. M. Conan, L. M. Mugnier, T. Fusco, V. Michau, and G. Rousset. Deconvolution of adaptive optics images using object autocorrelation and positivity. In *Adaptive Optics and Applications, Proc. SPIE, Vol. 3126:56-*, 1997.
- [22] A. Consortini, F. Cochetti, J. H. Churnside, and R. J. Hill. Inner-scale effect on irradiance variance measured for weak-to-strong atmospheric scintillation. *J. Opt. Soc. Am. A*, 10(11):2354–2362, 1993.
- [23] A. Consortini and K. A. O’Donnell. Measuring the inner scale of atmospheric turbulence by correlation of lateral displacements of thin parallel laser beams. *Waves in random media*, 3(2):85, 1993.
- [24] D. X. Cruz, F. Angeles, R. Avila, S. Cuevas, A. Farah, S. I. González, A. Iriarte, L. A. Martínez, M. Martínez, B. Sánchez, and L. J. Sánchez. Development of a Generalized SCIDAR at UNAM. *Revista Mexicana de Astronomía y Astrofísica Conference Series*, 19:44–51, 2003.
- [25] J. C. Dainty, B. M. Levine, B. J. Brames, and K. A. Odonnell. Measurements of the wavelength dependence and other properties of stellar scintillation at Mauna Kea, Hawaii. *Appl. Opt.*, 21:1196–1200, 1982.
- [26] N. Devaney and J. Keen. The use of turbulence-profile measurements to predict the performance of adaptive optics systems. *New Astronomy Reviews*, 42:459–463, 1998.
- [27] D. Dravins, L. Lindegren, E. Mezey, and A. T. Young. Atmospheric Intensity Scintillation of Stars, I. Statistical Distributions and Temporal Properties. *PASP*, 109:173–207, 1997.
- [28] D. Dravins, L. Lindegren, E. Mezey, and A. T. Young. Atmospheric Intensity Scintillation of Stars. II. Dependence on Optical Wavelength. *PASP*, 109:725–737, 1997.

- 
- [29] D. Dravins, L. Lindgren, E. Mezey, and A. T. Young. Atmospheric Intensity Scintillation of Stars. III. Effects for Different Telescope Apertures. *PASP*, 110:610–633, 1998.
- [30] B. L. Ellerbroek and D. W. Tyler. Adaptive optics sky coverage calculations for the Gemini-North telescope. *PASP*, 1998.
- [31] A. Fuchs, M. Tallon, and J. Vernin. Folding-up of the vertical atmospheric turbulence profile using an optical technique of movable observing plane. In W. A. Flood and W. B. Miller, editors, *Atmospheric Propagation and Remote Sensing III, Proc. SPIE, Vol. 2222:682-692*, 1994.
- [32] A. Fuchs, M. Tallon, and J. Vernin. Focusing on a turbulent layer: Principle of the “generalized scidar”. *PASP*, 110:86–91, 1998.
- [33] J. J. Fuensalida, B. García-Lorenzo, J. M. Delgado, C. Hoegemann, M. Verde, M. Reyes, and J. Vernin. Cute-SCIDAR: An automatically controlled SCIDAR instrument for the Jacobus Kapteyn telescope (ing newsl.), issue no. 8, p. 15-18.
- [34] J. W. Goodman. *Intoduction to Fourier Optics*. McGraw-Hill, New York, 1968.
- [35] J. W. Goodman. *Statistical Optics*. John Wiley and Sons, 1985.
- [36] A. Habib, J. Vernin, and Z. Benkhaldoun. Application de la technique du SCIDAR généralisé aux étoiles simples. *Comptes Rendus Physique*, 6(3):385–392, 2005.
- [37] A. Habib, J. Vernin, Z. Benkhaldoun, and H. Lanteri. Single star scidar: atmospheric parameters profiling using the simulated annealing algorithm. *Mon. Not.R. Astron. Soc*, 368(3):1456–1462, 2006.
- [38] J. Hadamard. New Haven, U.S.A.
- [39] M. Hanke, J. G. Nagy, and C. Vogel. Quasi-Newton approach to nonnegative image restorations. *Linear Algebra and its Applications*, 316(1-3):223–236, 2000.
- [40] P. C. Hansen. Numerical tools for analysis and solution of fredholm integral equations of the first kind. *Inverse Problems*, 8(6):849–872, 1992.



- 
- [41] C. M. Harding, R. A. Johnston, and R. G. Lane. Fast simulation of a Kolmogorov phase screen. *Appl. Opt.*, 38(11):2161–2170, 1999.
- [42] M. Iqbal. Deconvolution and regularization for numerical solutions of incorrectly posed problems. *JCAM*, 151:463–476, 2003.
- [43] J. M. Jarem. Remote determination of the structure constant profile from amplitude scintillation data using Tikhonov’s regularized inverse method. *IEEE Antennas and Propagation*, 31(1):145–148, 1983.
- [44] R. A. Johnston. *Inverse Problem in Astronomical Imaging*. PhD thesis, University of Canterbury, Christchurch, New Zealand, 2000.
- [45] R. A. Johnston, T.J. Connolly, and R. G. Lane. An improved method for deconvolving a positive image. *Optics Communications*, 181:267–278, 2000.
- [46] R. A. Johnston, C. Dainty, N. J. Wooder, and R. G. Lane. Generalized scintillation detection and ranging results obtained by use of a modified inversion technique. *Appl. Opt.*, 41(32):6768–6772, 2002.
- [47] R. A. Johnston and R. G. Lane. Modeling scintillation from an aperiodic Kolmogorov phase screen. *Appl. Opt.*, 39(26):4761–4769, 2000.
- [48] V. Klückers. A report on the feasibility of a single-star SCIDAR. 1998.
- [49] V. A. Klückers, N. J. Wooder, T. W. Nicholls, M. J. Adcock, I. Munro, and J. C. Dainty. Profiling of atmospheric turbulence strength and velocity using a generalized SCIDAR technique. *Astron. Astrophys. Suppl. Ser.*, 130:141–155, 1998.
- [50] A. N. Kolmogorov. The local structure of turbulence in an incompressible fluid for very large Reynolds numbers. *Dokl. Akad. Nauk. SSSR*, 30:301–305, 1941.
- [51] J. Krause-Polstorff, E. A. Murphy, and D. L. Walters. Instrument comparison - corrected stellar scintillometer versus isoplanometer. *Appl. Opt.*, 32:4051–4057, 1993.

- 
- [52] M. Le Louarn. Impact of atmospheric parameters on AO system design. *Atmosphere knowledge and Adaptive Optics for 8 to 100 m telescopes, ESO Mini Workshop, Garching*, October 2003.
- [53] David G. Luenberger. *Linear and Nonlinear Programming*. Reading, Mass.: Addison-Wesley, Massachusetts, 2nd edition, 1984.
- [54] E. Masciadri and P. Jabouille. Improvements in the optical turbulence parameterization for 3D simulations in a region around a telescope. *Astron. Astrophys.*, 376:727–734, 2001.
- [55] E. Masciadri, J. Vernin, and P. Bougeault. 3D numerical simulations of optical turbulence at the Roque de Los Muchachos Observatory using the atmospheric model Meso-Nh. *Astron. Astrophys.*, 365:699–708, 2001.
- [56] A. M. Obukhov. The structure of the temperature field in a turbulent flow. *Izv. Akad. Nauk SSSR, Ser. Geogr. Geofiz.*, 13:58, 1949.
- [57] G. R. Ochs, R. S. Lawrence, T. Wang, and P. Zieske. Stellar-scintillation measurement of the vertical profile of refractive-index turbulence in the atmosphere. In *Imaging through the atmosphere; Proceedings of the Seminar, Reston, Va.*, volume 75, pages 48–54, 1976.
- [58] R. R. Parenti and R. J. Sasiela. Laser-guide-star systems for astronomical applications. *J. Opt. Soc. Am. A*, 11(1):288, 1994.
- [59] A. Peskoff. Theory of remote sensing of clear-air turbulence profiles. *J. Opt. Soc. Am.*, 1968.
- [60] W. H. Press, S. A. Teukolsky, W. T. Vetterling, and B. P. Flannery. *Numerical Recipes in C: The Art of Scientific Computing*. Cambridge University Press, 1992.
- [61] A. Rocca, F. Roddier, and J. Vernin. Detection of atmospheric turbulent layers by spatiotemporal and spatioangular correlation measurements of stellar-light scintillation. *J. Opt. Soc. Am.*, 64(7):1000–1004, 1974.

- 
- [62] F. Roddier. The effects of atmospheric turbulence in optical astronomy. In *Progress in Optics, Volume 19*, pages 281–376. Amsterdam, North-Holland Publishing Co, 1981.
- [63] M. Sarazin. Site atmospheric characterization. In M. Cullum, editor, *Adaptive Optics Topical Meeting, Garching, October 2-6, 439-+*, 1995.
- [64] M. Sarazin and F. Roddier. The ESO differential image motion monitor. *Astron. Astrophys.*, 227:294–300, 1990.
- [65] J. L. Starck, F. Murtagh, P. Querre, and F. Bonnarel. Entropy and astronomical data analysis: Perspectives from multiresolution analysis. *Astron. Astrophys.*, 368:730–746, 2001.
- [66] K. B. Stevens. *Remote Measurements of the Atmospheric Isoplanatic Angle and Determination of Refractive Turbulence Profiles by Direct Inversion of the Scintillation Amplitude Covariance Function With Tikhonov Regularization*. PhD thesis, Naval Postgraduate School, Monterey, California, USA, 1985.
- [67] V. I. Tatarskii. *Wave Propagation in a Turbulent Medium Translated From Russian by R. A. Silverman*. McGraw-Hill, 1961.
- [68] A. Tokovinin. Measurement of seeing and the atmospheric time constant by differential scintillations. *Appl. Opt.*, 41(6):957–964, 2002.
- [69] A. Tokovinin. MASS-DIMM: a turbulence monitor for adaptive optics. *Atmosphere knowledge and Adaptive Optics for 8 to 100 m telescopes, ESO Mini Workshop, Garching, October 2003*.
- [70] A. Tokovinin, V. Kornilov, N. Shatsky, and O. Voziakova. Restoration of turbulence profile from scintillation indices. *Mon. Not.R. Astron. Soc.*, 343(3):891–899, 2003.
- [71] A. Tokovinin, J. Vernin, A. Ziad, and M. R. Chun. Optical turbulence profiles at Mauna Kea measured by MASS and SCIDAR. *PASP*, 117(830):395–400, 2005.

- 
- [72] J. Vernin. Atmospheric parameters and adaptive optics design: Key parameters, measurement equipment and impact on AO design. *Atmosphere knowledge and Adaptive Optics for 8 to 100 m telescopes, ESO Mini Workshop, Garching*, October 2003.
- [73] J. Vernin and F. Roddier. Experimental determination of two-dimensional spatiotemporal power spectra of stellar light scintillation. evidence for a multilayer structure of the air turbulence in the upper troposphere. *J. Opt. Soc. Am. A*, 63(5):270–273, 1973.
- [74] J. Vernin and F. Roddier. Détection au sol de la turbulence stratosphérique par intercorrélacion spatioangulaire de la scintillation stellaire. *C.R.A.S*, 280:463–465, 1975.
- [75] C. Vogel. *Computational Methods for Inverse Problems*. SIAM, 2002.
- [76] V. V. Voitsekhovich, V. G. Orlov, and L. J. Sanchez. Influence of scintillations on the performance of adaptive astronomical systems with Hartmann-like wavefront sensors. *Astron. Astrophys.*, 368:1133–1136, 2001.
- [77] R. W. Wilson. SLODAR: Measuring optical turbulence altitude with a Shack-Hartmann wavefront sensor. *Mon. Not. R. Astron. Soc*, 337:103, 2002.
- [78] R. W. Wilson. Turbulence profiler and seeing monitor for laser guide star adaptive optics,. In *Adaptive Optical System Technologies II. Proceedings, Proc. SPIE, Vol. 4839:466-472*, 2003.
- [79] R. W. Wilson, J. Bate, J. C. Guerra, N. N. Hubin, M. Sarazin, and C. D. Saunter. Development of a portable SLODAR turbulence profiler. In *Advancements in Adaptive Optics. Proceedings of the SPIE, Volume 5490, pp. 758-765 (2004).*, 2004.
- [80] G. M. Wing. *A Primer on Integral Equations of the First Kind: The Problem of Deconvolution and Unfolding*. Society for Industrial and Applied Mathematics, 1991.
- [81] A. T. Young. Photometric error analysis. viii: The temporal power spectrum of scintillation. *Appl. Opt.*, 8(5):869–885, 1969.